MODERN

APPLIED

SCIENCE

CCSE

Canadian Center of Science and Education

Editorial Board

Contents

Enhancing the Properties of Mahang *(Macaranga* spp.)

Wood through Acrylic Treatment in Combination with Crosslinker

Aikfei Ang, Zaidon Ashaari (Corresponding author), Edi Suhaimi Bakar & Mohd Hamami Sahri

Faculty of Forestry, Universiti Putra Malaysia

43400, Serdang, Selangor, Malaysia

Tel: 60-3-8946-7174   E-mail: zaidon@putra.upm.edu.my

Mohd Khairun Anwar Uyup & Hamdan Husin

Forest Research Institute Malaysia (FRIM)

52109, Kepong, Malaysia

Tel: 60-3-6279-7285   E-mail: mkanuar@frim.gov.my

Abstract

Macaranga spp. (mahang) was treated with methyl methacrylate (MMA) in combination with a crosslinker trimethylolpropane trimethacrylate (TMPTMA). Polymerisation was carried out by catalyst heat treatment. A fairly consistent acrylic retention was found in the wood when treated with or without crosslinker. Polymerisation of MMA is at maximum with 1% crosslinker and beyond this concentration the polymerisation decreased. The dimensional stability in terms of anti-swelling efficiency (ASE) was determined and found to be improved on treatment. Water absorption was also found to be decreased considerably for treated wood. Mechanical strength of the treated wood in terms of modulus of rupture (MOR), compressive stress and hardness were improved, but the stiffness (modulus of elasticity) did not change. In terms of specific strength (strength to density ratio), the treated material is less stiffer and less strength in lateral direction compared to untreated wood.   However, the specific compressive strength perpendicular to the grain and hardness of the treated material were superior compared with the untreated.

Keywords: Mahang, Methyl methacrylate, Crosslinker, Anti-swelling efficiency

1. Introduction

Mahang (*Macaranga* spp.) is a light density hardwood from a pioneer tree species which emerge large quantity in logged-over forest in Southeast Asia (Helmer *et al*., 2000). It has a   potential as resources to augment the depleting supply of logs from natural and plantation forests. Due to its poor properties in nature, it is still underutilized, but this wood can have value added by being made into wood suitable for different applications like flooring, panelling and furniture through proper treatment such as chemical modification.

Wood properties can be modified through treatment either with or without changing the chemical nature of the wood (Norimoto and Gril, 1993). Considerable work has been done on the modification of wood by impregnation with suitable polymers depending upon the end uses (Hill, 2006). Treatment with vinyl type monomer followed by curing (radiation or calatlyst) significantly improved the moisture resistance, hardness of wood (Meyer, 1984). Vinyl monomers have also proven effective in imparting dimensional of oil palm wood (Ibrahim, 1989). This treatment does not change the chemical nature of the wood and is known as wood-polymer composite (WPC) (Hill, 2006). WPC shows improvement in both physical and mechanical properties over untreated wood (Rowell and Konkol, 1987). Impregnation of rubberwood with styrene in combination with a crosslinker glycidyl methacrylate improved the dimensional stability, strength and stiffness of the wood (Devi *et al.,* 2003). The impregnation of wood with acrylic or vinyl type monomer showed less dimensional stability in the presence of moisture. This was due to the confinement of the monomer in the cell lumen instead of the cell wall (Rowell and Youngs, 1981). Attempt has also been made to impregnate acrylic polymer into softwood and hardwood but the dimensional stability imparted was low (Ashaari *et al.,* 1990a). A greater dimensional stability was achieved when treated with aqueous dimethylodihydroxythleneurea (DMDHEU), a glyoxal urea adduct, but this treatment significantly reduced the strength and stiffness of wood (Ashaari *et al*., 1990b).

Methyl methacrylate (MMA) is one of the least expensive and most readily monomers and is used alone or in combination with other monomers to crosslink the polymer system. Ng *et al.* (1999) stated that dimensional stability of MMA-treated wood can be further enhanced through incorporation of crosslinking agent to the treating solution. Crosslinking agents generally accelerate polymerization reaction rate and improve the properties of WPC (Kenaga, 1970). Geraldes *et al.* (2004) did a series of studies on acrylates crosslinking agents capable to impart a more effective croos-linking on Poly(MMA) matrix. They found out that trimethylene propane trimethylacrylate (TMPTMA) and diethylene glycol diacrylate (DEGDMA) presented higher reactivity or compatibility with the polymer. Modification of mahang with MMA is expected to enhance its properties and may expand the usage of this material especially in the manufacturing of laminated products such as flooring, panelling and furniture components.

The purpose of this study was to modify the low density wood of *Macaranga* spp. (mahang) with acrylate in combination with crosslinker (TMPTMA), and examine the effect of the treatment on dimensional stability and strength properties of the modified wood.

2. Materials and Method

2.1 Materials

Mahang *(Macaranga* spp.) wood was obtained from Forest Research Institute, Malaysia. The treating solution was methyl methacrylate (MMA) and trimethylolpropane trimethacrylate (TMPTMA) as crosslinking agent while benzoyl peroxide (BPO) was used as a free radical catalyst to accelerate the polymerization process. All chemicals were of analytical grade and were used as received. The solution was prepared by adding 2% BPO and 0%, 1%, 3% and 5% crosslinkers separately to MMA solution. The wood were flat sawn into samples (the width is tangential surface) of nominally 10-mm thick, 50-mm wide and 150-mm long. End-matched samples were assigned to one of five groups: 0%, 1%, 3% and 5% crosslinking agents or control . The control group was untreated.

2.2 Impregnation process

All samples were dried in an forced circulation air oven at 103 ± 2^0C to constant weight before treatment and the dimensions (V_o) and weights (W_o) were measured. The samples were then impregnated with the MMA solutions separately using a Bethel cycle in a cylinder. The treating cycle consisted of a 15-min initial vacuum of 85 kPa. The cylinder was then filled with treating solutions under vacuum. When the cylinder was completely filled with the solution, a pressure of 340 kPa was applied and held for 30 min at ambient temperature. The cylinder was then vented to atmospheric pressure and the solution was withdrawn. The impregnated samples were immediately weighed and wrapped with several layers of aluminium foil to prevent evaporation of MMA. Prior to weighing (W_f), excess solution was removed by blotting. The samples were then heat in an oven maintained at 65ºC±1ºC for 2 h. Excess polymer on the surface of the treated wood was scrapped off using scrapper. This was followed by drying in an oven at 103 ± 2^0C to constant weight. Oven dry weight (W_{to}) and volume were measured (V_{to}) before the were conditioned to equilibrium condition at 65±5% relative humidity maintained at 25±2°C.

2.3 Determination of polymer content

The treated samples were evaluated for percentage of monomer in the sample (% M), percentage of polymer content in the sample (% P), and percent conversion of monomer into polymer (% C). They were calculated using the following Equations (Duran and Meyer, 1972):

% M = 100 (W_m / W_o)   [1]

% P = 100 (W_p / W_o)   [2]

% C = 100 (W_p / W_m)   [3]

% Change in dimension (ΔD)   = 100 [($V_o - V_{to}$) / V_o]   [4]

where,

W_m (weight of monomer, g) = ($W_f - W_{od}$) / W_{od} [5]

W_p weight of polymer, g = ($W_{to} - W_{od}$) / W_{od} [6]

W_o = oven dried weight of untreated wood sample, g

2.4 Evaluation of dimensional stability

Dimensional stabilization was quantified by comparing the volumetric swelling coefficients and water absorption of treated and control specimens. The swelling process were done through 30-min vacuum followed by soaking in distilled water for 24 h (Ashaari *et al.,* 1990a*)* and exposing in water vapour at 95% relative humidity (Rowell and Youngs, 1981).   In this case, the exposure time is taken to be completed when the untreated samples reached constant weight. This took approximately 35 days. For this test, oven-dried wafers measuring 20 mm x 20 mm in cross sections and 10 mm were used. The weight and volume of samples before and after swelling process were measured. The volumertic

swelling coefficient (S), reduction in water absorption (R) and antiswelling efficiency (ASE) were calculated using the following equations.

$$S (\%) = 100 (V_w - V_d) / V_d \qquad\qquad [7]$$

$$R (\%) = 100 (M_c - M_t) / M_c \qquad\qquad [8]$$

$$ASE (\%) = 100 (S_c - S_t) / S_c \qquad\qquad [9]$$

Where,

V_w = volume after humidity conditioning or soaking in water, mm^3

V_d = volume of oven dry, mm^3

M_c = moisture content untreated,%

M_t = moisture content treated, %

S_c = untreated volumetric swelling coefficient, mm^3

S_t = treated volumetric swelling coefficient, mm^3

2.5 Evaluation of mechanical properties

2.5.1 Static bending test

Static bending test was performed according to procedure specified in British Standard BS 373: 1957 (BSI 1957) with a modification of the specimen size (10-mm thick, 20-mm wide and 250-mm long). The specimens were tested under a static load with the crosshead speed of 5.0 mm/min. The test was carried out on 50 kN Instron universal testing machine. Load deflection curves were recorded. Mechanical properties calculated from the load deflection curves included modulus of rapture (MOR) and modulus of elasticity (MOE).

2.5.2 Compression perpendicular to grain test

The tests were carried out according to British Standard BS 373:1957 (BSI 1957) with small specimens size (10-mm thick, 20-mm wide and 20-mm long). The crosshead speed of this test was 0.5 mm/min. The properties computed were compressive stress at proportional limit (CSPL) and compressive stress at compression of 2.50mm (CSmax).

2.5.3 Hardness test (Janka indentation test)

The size of test blocks was 10 mm x 40 mm x 60 mm. The test was carried out by probing 11.3-mm diameter sphere onto the wide surface of the specimens. Load at which the ball had penetrated to one half its diameter was recorded (BSI 1957)

2.6 Experimental design

Statistical analyses were performed on physical and mechanical property values to detect any changes in the treated material compared to untreated group. A complete randomized design with 4 levels of treatment and untreated was conducted where the treatment means were separated by using Tukey at $p < 0.05$.

3. Results and Discussion

3.1 Polymerization of MMA in mahang wood

The trends of monomer and polymer loadings in mahang wood with various concentrations of crosslinking agent are shown in Figure 2. A consistent loading of MMA monomer (254-265%) in the wood when treated with or without crosslinking agent. The higher monomer uptake by the wood is very much attributed to the porosity and permeability of the material. It is known that mahang is a very low density and permeable wood. In terms of polymerisation, MMA with 1% TMPTMA crosslinker gave the highest polymer loading (230%) with 87% monomer converted to polymer, while wood treated without crosslinking agent had the lowest loading (186%) with only 74% conversion when curing at 65^0C. The results suggest that the crosslinking agent had successfully generate higher crosslinked matrix of Poly(MMA). Earlier research found that 1% TMPTMA can generate 96.6% crosslinked matrix of PMMA at 87.8^0C (Geraldes *et al.,* 2004). However, with the increasing concentration of TMPTMA in the treating solution, the polymer loading decreases. This is shown by the polymer loading values in 3% and 5% TMPTMA which were 216% and 197% respectively (Table 1). The additional amount of the crosslinking agent will depress the increasing molecular weight of linear Poly(MMA) (Meyer, 1984).

The location of polymers in the samples was investigated using a scanning electron microscope. As shown in Figures 1 and 2, polymer is seen occupying the cell lumen and vessels of the wood. In the case of acrylic treatment with 1% crosslinker (Figure 2), higher percentage of cell lumens and vessels were filled with polymers than in sample treated without crosslinking agent (Figure 1), indicating that the TMPTMA had successfully generated higher crosslinked matrix of polymer.

3.2 Properties of Mahang-MMA composite

Table 1 summarises the analysis of variance (ANOVA) on properties of untreated and MMA-treated mahang. The descriptive statistics of the properties is given in Table 2. Group means with the same letter are not significantly different. Percent increment of property values exhibited in the table is compared to untreated values. The ANOVA shows that except for modulus of elasticity (MOE), all the properties tested significantly differ among the treatment groups.

3.2.1 Effect on physical properties

The density of mahang wood increased significantly by approximately 200% from 288 kgm^{-3} (untreated) to about 829 – 910 kgm^{-3}. This variation in density was affected by the polymer loading. Samples with the highest polymer loading (with 1% crosslinker) had the highest density (910 kgm^{-3}) and those with the lowest polymer loading had the lowest density (829 kgm^{-3}). When immersed in water for 24 h, the anti-swelling efficiency (ASE) of the wood ranged from of 48-51% with no significant difference was noticed among the treatments. It has been reported oil palm wood treated with MMA without crosslinking agents had an ASE of 46% (Ibrahim, 1989). When exposed to water vapour (95%) up to 35 days, the modified wood without crosslinker had lower ASE value (21.9%) compared to those with crosslinker (36.3 – 41.6%). There is no difference in ASE of the modified wood with different concentration of crosslinker. After that, the dimensional stability is expected to behave similar to untreated wood (Hill, 2006). This poly(MMA) is simply bulked the cell lumens and vessels of the wood. There is no significant changes in dimension of the wood after treatment suggesting that no monomer penetrated the cell wall (Table 2). The cell wall is freely to swell and polymers are just act as barrier to reduce the moisture uptake (Calleton *et al*., 1970; Noah and Foudjet, 1988 and Ibach and Ellis, 2005). In this study, MMA treatment with or without crosslinker showed very effective in reducing water or moisture uptake. In 24 h soaking in water, the R values were in the range of 92-94%, while in longer time exposure to water vapour, the values were 50-64%.

3.2.2 Effect on mechanical properties

A significant increment was found for MOR, compressive stress and hardness values of modified mahang. No difference in MOE was found between the modified wood and the untreated wood, although 11 - 23% improvement for MMA-treated wood. The result suggests that regardless of the presence of TMPTMA in the treatment, the polymer content alone affects the mechanical properties except for MOE. The insignificant change in MOE suggests that the polymer itself was not elastic enough which could enhance the elasticity of the wood. Schneider *et al.* (2003) also reported the same for basswood when treated with MMA. For MOR, the increment was between 23 to 55% from the original value of 57.27 Nmm^{-2}. Among the MMA-treated material, those with the highest polymer content, i.e., treatment with the addition of 1% TMPTMA had the highest MOR value (88.87 Nmm^{-2}). The same was also noted for compressive stress. CSPL and CSmax values for the treated material were markedly increased, i.e., by between 576 -1384% and by 632 – 1188%, respectively. The MMA treatment also significantly increased the hardness of mahang. The increasing rates vary between 219% and 386% and the highest value was recorded for treated wood without TMPTMA (6.07 kN). Majority of the treated samples failed before the sphere fully penetrates the surface of the test blocks. This shows that *in situ* polymerisation of MMA tends to produce more brittle material.

Specific strength is the ratio of mechanical values over density. It is known that mechanical properties of wood are directly proportional to density (Haygreen and Bowyer, 1982). The analysis was done to investigate whether the weight gain due to the treatment would compensate the increment in mechanical properties. Results in Table 3 show that the treated board had much lower specific MOE values (8.60-8.95 Nm^3/kgmm^2) and MOR (0.084-0.098 Nm^3/kgmm^2) compared to 22.7 Nm^3/kgmm^2 and 0.199 Nm^3/kgmm^2, respectively in untreated material. This indicates that at an equal density level, the treated wood is 60% less stiffer and can only sustain 49% of its original lateral load. However, the specific stress perpendicular to the grain 3-4 folds than that of untreated. For hardness, the specific value was about similar or slightly higher compared to the untreated material.

4. Conclusions

The study shows that MMA loading in mahang wood was fairly consistent when treated with or without crosslinking agent (TMPTMA) using a bethel process. The highest degree of polymerisation was attained with the addition of 1% crosslinker and beyond this concentration the polymerisation decreased. The density of the modified wood increased markedly and it is very much associated with the polymer contents. The dimensional stability of the modified wood with or without crosslinker when soaked in water for 24 h was similar. However, in water vapour, treatment with crosslinker imparted higher dimensional stability. The stability of the material was not affected by the contents of the crosslinking agent. Polymer loading significantly affects the strength and hardness of the wood but did not change the stiffness. As regards to specific strength, the results show that at equal density level, the treated material is less stiffer and sustained lesser lateral load than that of untreated wood. Nevertheless, the specific compressive strength perpendicular to the grain and hardness were greater in treated mahang compared to untreated.

References

Ashaari, Z., Barnes, H.M., Vasisth, R.C., Nicholas, D.D. and Lyon, D.E. (1990a). Effect of aqueous polymer treatments on properties. Part I: Treatability and dimensional stability. *International Research Group on Wood Preservation*, Doc. No. IRG/WP/3610.

Ashaari, Z., Barnes, H.M., Vasisth, R.C., Nicholas, D.D. and Lyon, D.E. (1990b). Effect of aqueous polymer treatments on properties. Part II: Mechanical properties. *International Research Group on Wood Preservation* Doc. No. IRG/WP/3611

BSI (Bristish Standard Institute) (1957). *British Standard 373:1957: Methods of testing small clear specimens of timber.* British Standard Institution, London.

Calleton, R.L., Choong, E.T. and Mcilhenny, R.C. (1970). Treatments of southern Pine with vinyl chloride and methyl methacrylate for radiation-produced wood-plastic combinations. *Wood Science and Technology* 4:216–225.

Devi, R.R., Ali, I. and Maji, T.K. (2003). Chemical modification of rubberwood with styrene in combination with a crosslinker: effect on dimensional stability and strength property. *Bioresource Technology* 88:185-188.

Duran, J.A. and Meyer, J.A. (1972). Exothermic heat released during catalytic polymerization of Basswood-methyl methacrylate composites. *Wood Science and Technology* Vol. 6:59-66.

Geraldes, A.N., Parra, D.F., Cardoso, E.C.L., Ribeiro, M.S., Santos, W.V.C., Galin, P.C. and Lugao, A.B. 2004. The effect of acrylates cross-linking agents on PMMA matrix.   Pp. 345-349 in IV Brazilian Congress of Thermal Analysis and Calorimetry II and Pan-American Congress of Thermal Analysis and Calorimetry, Pocos de Caldas, MG. Vol. 1.

Haygreen, J.G. and Bowyer, J.L. (1982). Mechanical properties of wood. Pp. 219-250 in *Forest products and wood science: An introduction.* The Iowa State University Press.

Helmer, T., Trockenbrodt, M. and Fruhwald, A. (2000). Wood density and elastomechanical properties of *Macaranga gigantifolia* and *M. hypoleuca* from Sabah, Malaysia. *Journal of Tropical Forests Products Malaysia* 6(1):62-67

Hill, C.A.S., (2006). Modyfying the properties of wood. Pp. 19-44 in *Wood modification: Chemical, thermal and other processes.* John Wiley & Sons, Ltd.

Ibach, R.E. and Ellis, W.D. (2005). Lumen modifications. Pp. 421-446 in Rowell, R.M. (Ed.) *Handbook of Wood Chemistry and Wood Composites.* CRC press.

Ibrahim, W. A. (1989). Densification and stabilization of oil palm stem by treatment with two polymers. *Journal of Tropical Forest Science* 2(1):1–7.

Kenaga, D.L. (1970). Heat cure of high boiling styrene-type monomers in wood. *Wood Fiber Sci.* 2(1):40–51.

Meyer, J.A. (1984). Wood-polymer materials. Pp. 257–289 in Rowell, R.M. (Ed.) *The Chemistry of Solid Wood.* American Chemical Society, Washington, D.C.

Ng, L.T., Garnet, J.L. and Mohajerani, S. (1999). Role of additives in wood-polymer composites. Relationship to analogous radiation grafting and curing processes. *Radiation Physics and Chemistry* 55:633–637.

Noah, J.N. and Foudjet, A. (1988). Wood-polymer composites from some tropical hardwoods. *Wood Sci. Technol.* 22:115–119

Norimoto, M. and Gril, J. (1993). Structure and properties of chemically treated woods. Pp. 135–154 in Shiraishi, N., Kajita, H. and Norimoto, M. (Eds.) *Recent Research on Wood and Wood-based Materials.* Elsevier, Barking, UK.

Rowell, R.M. and Konkol, P. (1987). Treatments that enhance physical properties of wood. *Gen. Tech. Rep. FPL-GTR-55.* Madison, U.S. Department of Agriculture, Forest Service, Forest Product Laboratory.

Rowell, R. M. and Youngs, R. L. (1981). Dimensional stabilization of wood in use. *U. S. For. Serv., For. Prod. Res. Note FPL -0243.* Forest Product Laboratory, Wisconsin.

Schneider, M.H., Vasic, S., Lande, S. and Phillips, J.G. (2003). Static bending and toughness of wood polymer composites (yellow birch and basswood). *Wood Sci. Technol.* 37:165–176.

Table 1. Summary of ANOVA on properties of MMA-treated mahang

Source of variation	%P	ASE	CSPL	CSmax	Hardness	MOE	MOR
Treatments	-	-	**	**	**	ns	**
Concentrations of TMPTMA	**	**	**	**	ns	ns	**

** = significantly different at p<0.05, ns = not significantly different

Table 2. Physical properties of MMA-treated mahang

TMPMTA concentrations (%)	0%	1%	3%	5%
Polymer (%)	187.5b	229.6a	216.4ab	197.2ab
	N=5	*N=5*	*N=5*	*N=5*
ΔD (%)	-3.9	-1.85	-3.33	-2.41
Density (kgm^{-3})	829b±80.0	910a±70.0	903a±79.3	844ab ±16.2
Increment, %	188	216	214	193
	N=5	*N=5*	*N=5*	*N=5*
Reduction in absorption (R_1, %)	94.36a±0.51 *N=10*	93.95a±1.930 *N=10*	94.29a±1.03 *N=10*	92.0a±3.19 *N=10*
ASE_1, %	48.49a±8.92 *N=10*	50.82a±9.61 *N=10*	49.64a±8.66 *N=10*	48.24a±11.38 *N=10*
Reduction in absorption (R_2, %)	60.05a±10.52 *N=12*	59.21a±11.51 *N=12*	63.35a±6.48 *N=12*	49.38b±5.44 *N=12*
ASE_2, %	21.94b±2. 63 *N=12*	41.53a±4.7 *N=12*	36.28a±3.55 *N=12*	41.63a±6.71 *N=12*

[1]Means followed by the same letter are not significantly different (p < 0.05), ± are standard deviations

ASE_1 and R_1 = determined by soaking after vacuumed for 24 h, ASE_2 and R_2 = determined by humidity conditioning, *N*= Number of samples

Table 3. Mechanical properties of MMA-treated mahang compared with untreated wood

TMPMTA concentrations (%)	Control	0%	1%	3%	5%
Polymer (%)		187.5b	229.6a	216.4ab	197.2ab
MOR (Nmm^{-2})	57.27c±4.5	79.34ab±15.04	88.87a±1.1	79.60ab±8.16	70.64b±6.3
Increment, %		39	55	39	23
MOE (Nmm^{-2})	6540a±740	7424a±909	7886a±640	8040a±567	7259a±569
Increment, %		14	21	23	11
CSPL (Nmm^{-2})	2.80d±0.53	23.98c±4.35	41.57a±2.35	32.60b±3.92	18.93c±0.78
Increment,%		632	1188	1025	710
CSmax (Nmm^{-2})	5.65c±1.0	41.36b±6.17	72.75a±6.7	63.58a±11.55	45.79b±6.86
Increment,%		386	219	279	350
Hardness (kN)	1.25b±0.21	6.07a±1.97	3.99a±1.49	4.74a±1.03	5.63a±0.93
Increment,%		386	219	279	350

[1]Means followed by the same letter are not significantly different ($p < 0.05$), ± are standard deviations

Table 4. Specific strength of MMA-treated mahang compared with untreated

| TMPMTA concentrations (%)	MOE (Nmm^{-2}/kgm^{-3})	MOR (Nmm^{-2}/kgm^{-3})	CSPL (Nmm^{-2}/kgm^{-3})	CSmax (Nmm^{-2}/kgm^{-3})	Hardness N/kgm^{-3}
Control	22.7	0.199	0.010	0.020	4.34
0.0	8.95	0.096	0.029	0.050	7.32
1.0	8.67	0.098	0.046	0.080	4.38
3.0	8.90	0.088	0.036	0.070	5.25
5.0	8.60	0.084	0.022	0.054	6.67
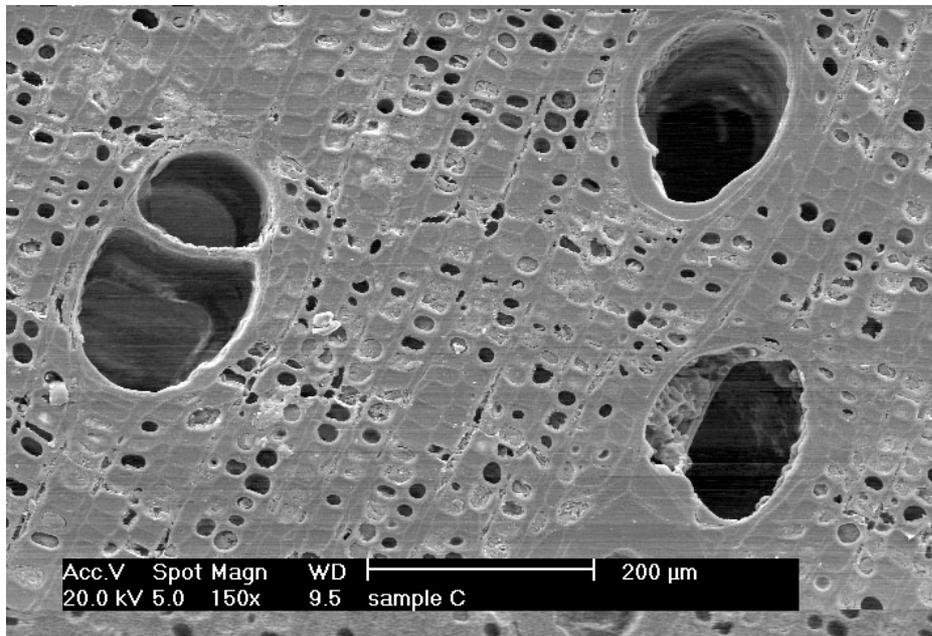
Figure 1. Cross section of MMA-treated mahang wood without crosslinking agent showing cell lumen and vessels with partially and fully filled with polymer
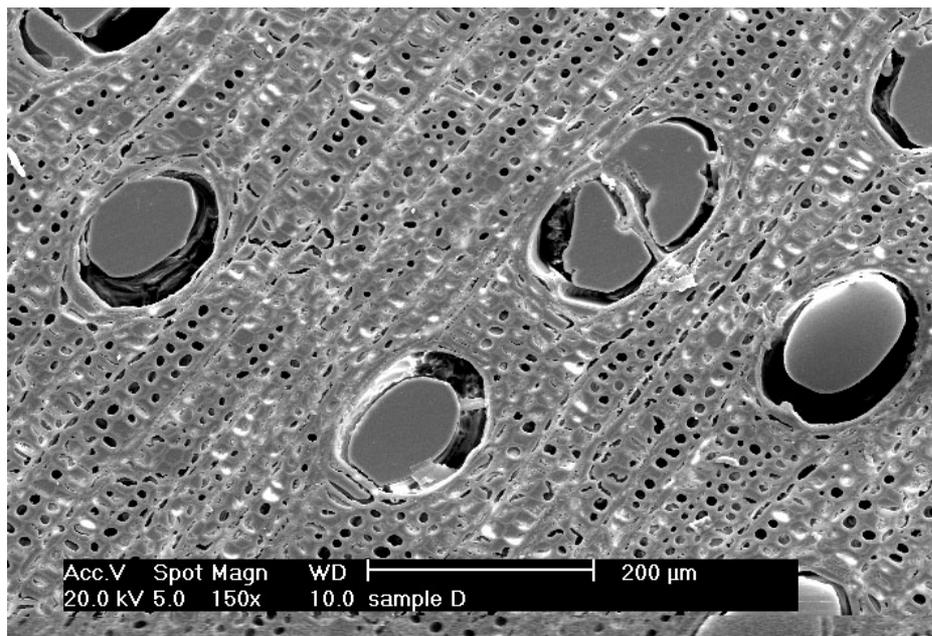

Figure 2. Cross section of MMA-treated mahang wood with 1% TMPTMA showing higher percentage of lumens and vessels filled with polymer
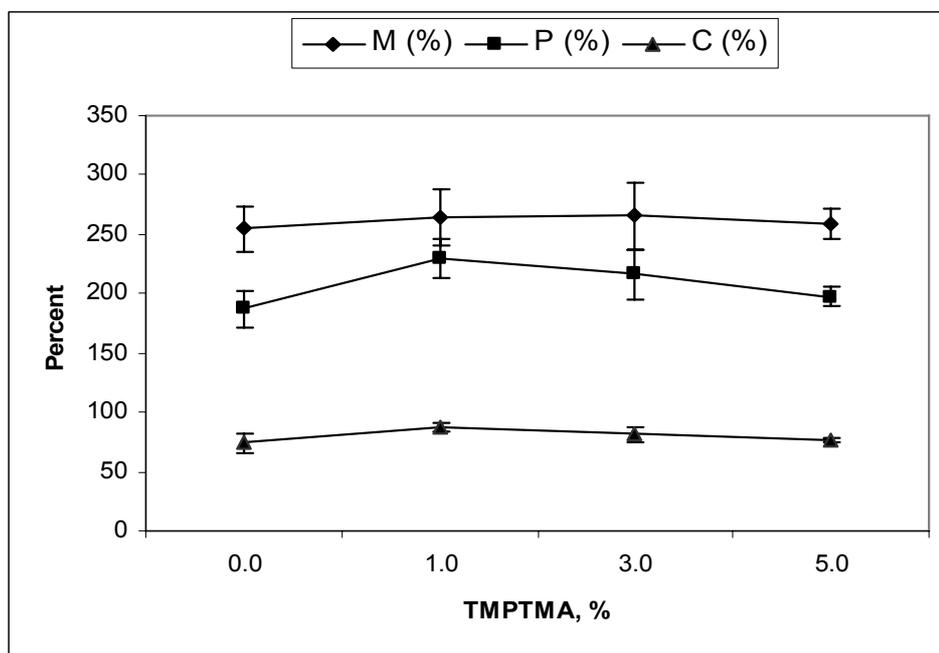
Figure 3. Effect of TMPTMA concentrations on polymerization of MMA in mahang

Remarks on New Properties of Preinvex Functions

Zaiyun Peng

Institute of Mathematics, College of Science

Chongqing JiaoTong University

Xue Fu Da Dao Street, Nan Ping, Chongqing 400074, China

E-mail: pengzaiyun@126.com.

Yawei Liu

Institute of Mathematics, College of Science, Chongqing JiaoTong University

Chongqing 400074, China

X. J. Long

College of Mathematics and Statistics, ChongqingTechnology and Business University

Chongqing 400067, China

Abstract

A new type of generalized convex functions, termed preinvex functions, is further discussed in this paper. A new result that if a preinvex function satisfies intermediate-point semistrict preinvexity then it is also a semistrictly preinvex function is obtained. Furthermore, another simplified proof for a criterion of preinvex functions under weaker conditions and an impotant application of preinvex functions are given.

Keywords: Preinvex functions, Semistrictly preinvex functions, Lower semicontinuity, Applications

1. Introduction

Convexity and generalized convexity play a central role in mathematical economics and optimization theories. Therefore, the research on convexity or generalized convexity becomes one of the most important aspects in mathematical programming. A significant generalization of convex functions termed preinvex functions was introduced by (Weir and Mond,1988). Yang and Li obtained some properties of preinvex function in (Yang and Li, 2001).Yang also discussed the relationships among convexity, semistrict convexity and strict convexity in (Yang,1994). In this paper, preinvex functions is further discussed in this paper. A new result that if a preinvex function satisfies intermediate-point semistrict preinvexity then it is also a semistrictly preinvex function is obtained. Furthermore, another simplified proof for a criterion of preinvex functions under weaker conditions and an impotant application of preinvex functions are given.

Now we recall some definitions .

Definition 1.1 (Weir,1998,p.29) A set $K \subseteq R^n$ is said to be invex if there exist a vector function $\eta : R^n \times R^n \to R^n$, such that

$$\forall x, y \in K, \forall \lambda \in [0,1] \Rightarrow y + \lambda \eta(x, y) \in K .$$

Definition 1.2 (Yang,2001) Let $K \subseteq R^n$ be an invex set with respect to $\eta : R^n \times R^n \to R^n$. Let $f : K \to R$. We say that f is preinvex on K, if $\forall x, y \in K, \lambda \in [0,1]$,

$$f(y + \lambda\eta(x, y)) \leq \lambda f(x) + (1 - \lambda)f(y).$$

Definition 1.3 (Yang,2001) Let $K \subseteq R^n$ be an invex set with respect to $\eta : R^n \times R^n \to R^n$. Let $f : K \to R$. We say that f is semistrictly preinvex on K, if $\forall \lambda \in (0,1)$ $\forall x, y \in K, f(x) \neq f(y)$,

$$f(y + \lambda\eta(x, y)) < \lambda f(x) + (1 - \lambda)f(y).$$

Condition C. Let $\eta : R^n \times R^n \to R^n$. We say that the vector-valued function η satisfies Condition C if for any $x, y \in K$ any $\lambda \in (0,1)$,

$$\eta(y, y + \lambda\eta(x, y)) = -\lambda\eta(x, y),$$

$$\eta(x, y + \lambda\eta(x, y)) = (1 - \lambda)\eta(x, y).$$

Example1. Let $\eta(x, y) = \begin{cases} x - y, (x \geq 0, y \geq 0) \\ x - y, (x < 0, y < 0) \\ -2 - y, (x > 0, y \leq 0) \\ 2 - y, (x \leq 0, y > 0) \end{cases}$

By Example 2.2 in (Yang, 2003), we know that η satisfies the Condition C. Another example that η satisfies the Condition C may refer Example 2.4 in (Yang, 1995, p.901).

2. Main Results

In (Yang,2001, p.256), the authors have discussed the preinvex functions and semistrictly preinvex functions.In this section, we will discuss the properties of preinvex functions. Firstly, we give the following basic lemma.

Lemma 2.1 Let f be a lower semicontinous and satisfy $f(y + \eta(x, y)) \leq f(x)$ ($\forall x, y \in K$), $\eta : R^n \times R^n \to R^n$ satisfies Condition C. If for every pair $x, y \in K$, there exist $\lambda \in (0,1)$ such that inequality

$$f(y + \lambda\eta(x, y)) \leq \lambda f(x) + (1 - \lambda)f(y) \tag{2.1}$$

then the set $A(x, y) = \{\alpha \in [0,1] \mid f(y + \alpha\eta(x, y)) \leq \alpha f(x) + (1 - \alpha)f(y)\}, \forall x, y \in K$ is dense in the interval $[0,1]$.

Proof . Given $x, y \in K, x \neq y$,suppose that $A(x, y)$ is not dense in [0,1]. Then , there exist $\overline{\alpha} \in (0,1)$ and $\varepsilon > 0$ such that

$$A(x, y) \cap (\overline{\alpha} - \varepsilon, \overline{\alpha} + \varepsilon) = \phi$$

For $f(y + \eta(x, y)) \leq f(x)$ ($\forall x, y \in K$), then $0 \in A(x, y)$,and $1 \in A(x, y)$.

Define

$$u = \sup\{\alpha \in A(x, y) : \alpha < \overline{\alpha}\}$$

$$v = \inf\{\alpha \in A(x, y) : \alpha > \overline{\alpha}\}$$

Let $u_1 \leq u_2 \leq ... \leq u_k \leq ...$, such that $u_k \to u$ as $k \to +\infty$, and $u_k \in A(x, y)$ for each k ,then

$$f(y + u_k\eta(x, y)) \leq u_k f(x) + (1 - u_k)f(y)$$

$$\liminf_{k \to \infty} f(y + u_k\eta(x, y)) \leq \liminf_{k \to \infty}[u_k f(x) + (1 - u_k)f(y)] \tag{2.2}$$

Since f is a lower semicontinous, we have

$$f(y + u\eta(x, y)) \leq \liminf_{k \to \infty} f(y + u_k\eta(x, y)) \tag{2.3}$$

Form (2.2) and (2.3), we obtain $f(y + u\eta(x, y)) \leq u f(x) + (1 - u)f(y)$ .Hence $u \in A(x, y)$.

Similarly, we get $v \in A(x, y)$.

Then, by the definitions of u and v, we obtain $0 \le u < \overline{\alpha} < v \le 1$, and

$$\alpha u + (1-\alpha)v \notin A(x,y), \forall \alpha \in (0,1) \tag{2.4}$$

Now denote $x_u = y + u\eta(x,y), y_v = y + v\eta(x,y)$

Then under inequality (2.1), there exist a $\lambda \in (0,1)$ such that

$$f(y_v + \lambda\eta(x_u, y_v)) \le \lambda f(x_u) + (1-\lambda)f(y_v) \tag{2.5}$$

From Condition C, we have

$$y_v + \lambda\eta(x_u, y_v) = y + v\eta(x,y) + \lambda\eta(y + u\eta(x,y), y + v\eta(x,y))$$

$$= y + v\eta(x,y) + \lambda\eta(y + u\eta(x,y), y + u\eta(x,y) - (u-v)\eta(x,y))$$

$$= y + [\lambda u + (1-\lambda)v]\eta(x,y)$$

Hence, by (2.5) and $u, v \in A(x,y)$, we obtain

$$f(y + [\lambda u + (1-\lambda)v]\eta(x,y)) = f(y_v + \lambda\eta(x_u, y_v))$$

$$\le \lambda f(x_u) + (1-\lambda)f(y_v) \le [\lambda u + (1-\lambda)v]f(x) + [1 - (\lambda u + (1-\lambda)v)]f(y)$$

Which implies $\lambda u + (1-\lambda)v \in A(x,y)$, and contradicts (2.4). Thus this proves Lemma2.1.

Theorem 2.2 Let f be a lower semicontinous and satisfy $f(y + \eta(x,y)) \le f(x)$ ($\forall x, y \in K$), $\eta : R^n \times R^n \to R^n$ satisfies Condition C. If for every pair $x, y \in K$, there exist $\lambda \in (0,1)$ such that inequality (2.1) holds, then f is a preinvex function on K.

Proof. By Lemma2.1, $\forall x, y \in K$, $A(x,y)$ is dense in the interval $[0,1]$.

Then, $\forall \overline{\alpha} \in (0,1)$, $\exists\{\alpha_n\} \subseteq (0,1) \cap A(x,y)$, such that $\alpha_n \to \overline{\alpha}$ as $n \to \infty$.

Since $f(y + \alpha_n\eta(x,y)) \le \alpha_n f(x) + (1-\alpha_n)f(y)$, then

$$\liminf_{k \to \infty} f(y + \alpha_k\eta(x,y)) \le \liminf_{k \to \infty}[\alpha_k f(x) + (1-\alpha_k)f(y)]$$

Since f is a lower semicontinous, we have

$$f(y + \overline{\alpha}\eta(x,y)) \le \liminf_{k \to \infty} f(y + \alpha_k\eta(x,y))$$

Thus $$f(y + \overline{\alpha}\eta(x,y)) \le \overline{\alpha}f(x) + (1-\overline{\alpha})f(y) \tag{2.6}$$

From Condition $f(y + \eta(x,y)) \le f(x)$ ($\forall x, y \in K$), when $\lambda = 0,1$ we also have

$$f(y + \lambda\eta(x,y)) \le \lambda f(x) + (1-\lambda)f(y) \tag{2.7}$$

So f is a preinvex function on K. This completes the proof.

Remark 2.1 A criterion of preinvex functions is given by theorem 2.2. Comparing with (Yang,2001), we give another simplified proof for the result.

Theorem 2.3 Let $K \subseteq R^n$ be an invex set with respect to $\eta : R^n \times R^n \to R^n$ which satisfies Condition C, and $f : K \to R$ be a preinvex function for the same η. If there exists an $\alpha \in (0,1)$, such that for all $x, y \in K, f(x) \ne f(y)$ implies

$$f(y + \alpha\eta(x,y)) < \alpha f(x) + (1-\alpha)f(y), \tag{2.8}$$

Then f is semistrictly preinvex on K with respect to η.

Proof. On the contrary, we assume that there exist $x, y \in K, \lambda \in (0,1)$ such that $f(x) \ne f(y)$ and

$$f(y + \lambda\eta(x, y)) \geq \lambda f(x) + (1 - \lambda)f(y). \tag{2.9}$$

Without loss of generality, we assume the $f(x) < f(y)$, let $z = y + \lambda\eta(x, y)$.

Then, inequality (2.9) implies

$$f(z) \geq \lambda f(x) + (1 - \lambda)f(y) > f(x). \tag{2.10}$$

Since f is preinvex function, we have

$$f(z) \leq \lambda f(x) + (1 - \lambda)f(y).$$

Which together with (2.10), leads to

$$f(x) < f(z) = \lambda f(x) + (1 - \lambda)f(y). \tag{2.11}$$

Let

$$z_1 = z + \alpha\eta(x, z)$$

$$z_2 = z + \alpha\eta(z_1, z)$$

$$\ldots$$

$$z_k = z + \alpha\eta(z_{k-1}, z), \forall k \in N$$

According to (2.11) and (2.8) ,we have

$$f(z_1) = f(z + \alpha\eta(x, z)) < f(z). \tag{2.12a}$$

$$f(z_2) = f(z + \alpha\eta(z_1, z)) < f(z). \tag{2.12b}$$

$$\ldots$$

$$f(z_k) = f(z + \alpha\eta(z_{k-1}, z)) < f(z). \tag{2.12c}$$

From Condition C, we have

$$z_k = z + \alpha^k \eta(x, z) = y + [\lambda + \alpha^k(1 - \lambda)]\eta(x, y)$$

Let $k_1 \in N$ be such that

$$\alpha^{k_1}/(1 - \alpha) < \lambda/(1 - \lambda)$$

Let $\beta_1 = \lambda + \alpha^{k_1}(1 - \lambda)$, $\beta_2 = \lambda - \dfrac{\alpha^{k_1+1}}{1 - \alpha}(1 - \lambda)$, $\overline{x} = y + \beta_1\eta(x, y)$, $\overline{y} = y + \beta_2\eta(x, y)$.

Then

$$0 \leq \beta_2 \leq \lambda \leq \beta_1 \leq 1, \lambda = \alpha\beta_1 + (1 - \alpha)\beta_2$$

Thus from Condition C,we have

$$z + \alpha^{k_1}\eta(x, z) = y + \lambda\eta(x, y) + \alpha^{k_1}\eta(x, y + \lambda\eta(x, y))$$

$$= y + [\lambda + \alpha^{k_1}(1 - \lambda)]\eta(x, y)$$

$$= y + \beta_1\eta(x, y) = \overline{x}. \tag{2.13}$$

From (2.12)(2.13), we obtain

$$f(\overline{x}) = f(z + \alpha^{k_1}\eta(x, z)) = f(z_{k_1}) < f(z). \tag{2.14}$$

There are two cases to be considered.

(i.) $f(\overline{x}) \geq f(\overline{y})$ .It follows from Condition C that

$$\overline{y} + \alpha\eta(\overline{x}, \overline{y}) = y + \beta_2\eta(x, y) + \alpha\eta(y + \beta_1\eta(x, y), y + \beta_2\eta(x, y))$$

$$= y + \beta_2\eta(x, y) + \alpha(\beta_1 - \beta_2)\eta(x, y)$$

$$= y + [\alpha\beta_1 + (1-\alpha)\beta_2]\eta(x,y) = y + \lambda\eta(x,y) = z$$

Since f is preinvex ,this implies

$$f(z) \le \alpha f(\bar{x}) + (1-\alpha)f(\bar{y}) \le f(\bar{x}).\text{which contradicts inequality (2.14)}.$$

(ii.) $f(\bar{x}) < f(\bar{y})$. Since $\bar{y} + \alpha\eta(\bar{x}, \bar{y}) = y + \lambda\eta(x,y) = z$

By (2.8), we get

$$f(z) < \alpha f(\bar{x}) + (1-\alpha)f(\bar{y}). \tag{2.15}$$

Again , $\bar{x} = y + \beta_1\eta(x,y), \bar{y} = y + \beta_2\eta(x,y)$ and f is preinvex , we have

$$f(\bar{x}) \le \beta_1 f(x) + (1-\beta_1)f(y) . \tag{2.16}$$

$$f(\bar{y}) \le \beta_2 f(x) + (1-\beta_2)f(y). \tag{2.17}$$

According to (2.15)-(2.17), we obtain

$$f(z) < \lambda f(x) + (1-\lambda)f(y),$$

Which contradicts (2.11). This completes the proof.

Let the problem of minimum $f(x)$ subject to $x \in K$ be denoted by (P). Now, we can discuss an application of preinvex functions to the problem (P).

Theorem 2.4 Let $K \subseteq R^n$ be a nonempty invex set with respect to $\eta : R^n \times R^n \to R^n$ and $f : K \to R$ be a preinvex function with respect to η. If $\bar{x}$ is a local minimum to the problem (P), then $\bar{x}$ is a global one.

Proof. If $\bar{x}$ is a local minimum to the problem (P), then there exists a neighborhood $U \in R^n$ with $\bar{x} \in U$ and

$$f(\bar{x}) \le f(x), \forall x \in K \cap U \tag{2.18}$$

Assume that $\bar{x}$ is not a global one of (P) ,then there exists $\hat{x} \in K$ with

$$f(\hat{x}) < f(\bar{x}) \tag{2.19}$$

Since $K \subseteq R^n$ be a nonempty invex set with respect to $\eta : R^n \times R^n \to R^n$ and $f : K \to R$ be a preinvex function, then $\forall \lambda \in (0,1)$

$$f(\bar{x} + \lambda\eta(\hat{x}, \bar{x})) \le \lambda f(\hat{x}) + (1-\lambda)f(\bar{x}) < f(\bar{x}) \tag{2.20}$$

i.e.,for any $\forall \lambda \in (0,1)$, we have

$$f(\bar{x} + \lambda\eta(\hat{x}, \bar{x})) < f(\bar{x})$$

$\lim_{\lambda \to 0}(\bar{x} + \lambda\eta(\hat{x}, \bar{x})) = \bar{x}$, so there exists a δ ($0 < \delta < 1$)and for all $\lambda \in (0, \delta)$ with $\bar{x} + \lambda\eta(\hat{x}, \bar{x}) \in K \cap U$. Whic is a contradiction to (2.18).This completes the proof.

Remark 2.2 From Theorem 2.4, we can conclude that preinvex functions constitutes an important class of generalized convex functions in mathematical programming.

References

Long X. J. ,Peng Z. Y. and Zeng B. (2009). Remark on cone semistrictly preinvex functions, *Optim Lett.*, 3,337-345.

Mohan, S, R and Neogy, S, K. (1995). On Invex sets and Preinvex Functions. *J Math Anal Appl,*189, 901-908.

Peng J W and Yang, X, M. (2005). Two Properties of Strictly Preinvex Functions. OR Transactions, 9, 37:42.

Peng, Z. Y. and Chen, Guo. (2007). Remarks on Prequasi-invex Functions. *Journal of China Three Gorges University* (Natural Science edition), 6, 70-72.

Peng, Z. Y. and Luo, H. L. (2006). Technical Note on Characterrizations of Strongly Preinvex Functions. *Journal of Chongqing Normal University(Natural Science edition)*, 23, 36--39.(in Chinese).

Weir, T and Mond, B. (1988). Preinvex Functions in Multiple Objective Optimization. *J Math Anal Appl.*,136, 29-38.

Yang, X, M and Li, D. (2001). On Properties of Preinvex Functions. *J Math Anal Appl*, 256, 29-241.

Yang, X, M and Li, D. (2001). Semistrictly Preinvex Functions. *J Math Anal Appl,* 258, 287-308.

Yang, X, M,Yang, X, Q and Teo, K, L. (2003). Generalized invexity and invariant monotonicicy. *J Optim Theory Appl.*, 117,607-625.

Yang, X, M. (1994). Semistrictly convex Functions. Opsearch, 31, 15-27.

A New Repetitive Control Strategy in a Liquid Level System

M.Vijayakarthick

Department of Instrumentation Engineering, Annamalai University

Annamalai Nagar-608002, TamilNadu, India

E-mail: vijayakarthick@yahoo.co.in

S.Sathishbabu

Department of Instrumentation Engineering, Annamalai University

Annamalai Nagar-608002, TamilNadu, India

E-mail: sathish3575@gmail.com

P.K.Bhaba (Corresponding author)

Department of Chemical Engineering, Annamalai University

Annamalai Nagar-608002, TamilNadu, India

E-mail: drpkbhaba@gmail.com

Abstract

In this research work, a new attempt is made to implement a Repetitive Control Strategy (RCS) in a Liquid Level System (LLS). First, the liquid level system is approximated into a First Order Plus Time Delay (FOPTD) model by step testing method. RCS is incorporated in the conventional level control loop of proportional (P) mode. Ziegler-Nichols Tuning Rule (ZNTR) based proportional controller parameter is considered in the loop. A periodic signal of sine wave in inflow to the level system is generated and real time runs of the LLS are carried out for the periodic input tracking with RCS based P mode control loop. The performance analysis of periodic input tracking is done. A similar run is carried out with the system having conventional P-mode structure in the control loop. A comparison in the performance analysis clearly indicates that the incorporation of RCS in the control loop in LLS provides a better tracking performance than the conventional P mode. The robustness of RCS incorporation in control loop is also justified with another tuning rule.

Keywords: Liquid Level System RCS-P, Conventional P, ZNTR, ATR

1. Introduction

The basic requirements in control systems is that they have the ability to regulate the controlled variable to the reference commands without steady state error against disturbances. Control of Level process have been widely studied in recent decades due to the importance in many industrial applications. In most level process control applications, P and PI controllers perform reasonably well under constant disturbances .However, consistent regulation performance is not achieved when the process is subject to periodic disturbances. One of the main contributions of the work presented in this paper is precisely implementation of the Repetitive Control Strategy in a level process. Repetitive control is a subclass of learning control systems that achieves low error in systems with periodic exogenous inputs with known period. This is achieved by introducing a highly frequency selective gain through a positive feedback loop containing a time delay element. The delay time is equal to the known period of the exogenous input.

The main applications of the RCS deal with tracking of periodic trajectories in the set point or rejecting periodic disturbances [J. H. Lee, et al,2001] with a known period. In the development of the RCS, the internal model principle (IMP) has played a major role. According to IMP [B A.Francis and W. M. Wonham, 1975] the controlled output tracks a class of reference commands without a steady state error only if the generator for references is included in the stable closed-loop system

The salient features of the RCS are as follows [Rong-Fong et al, 2000]: (i) In order to reduce tracking error in every period of the control system, tracking error in the previous period have to be considered. Therefore, the control method is obviously different from that used in the typical servomechanisms. (ii) Integrator and time delay of the system are combined for achieving the above description.

The concept of RCS has been largely used in different control areas such as CD and disk arm actuators, robotics [Yamada, M et al, 1999] electronic rectifiers [Zhou. K et al, 2000] and pulse-width modulated (PWM) inverters [Zhou.K., & Wang.D, 2001].etc. In particular the RCS have not found any significant application in chemical process because most of the chemical process handling large delays and non linear in nature. In this paper a first attempt is made to implement the RCS in liquid level chemical process. Here the level process behaves linear system with minimum delay

The paper is organized as follows: Section 2 summarizes the process description of Liquid Level Control System. In Section 3, Materials and Methods are described and the structure of Repetitive Control Scheme is also explained. Real time results are analyzed in Section 4 to illustrate the better performance of the proposed RCS in closed loop. Finally, concluding remarks are given in Section 5.

2. Process description

2.1 Experimental setup

The experimental setup of Liquid Level System is shown in figure1 and specifications are given in Table1. The setup consists of process tank, collection tank, variable speed motor pump and RF capacitance level sensor. The RF capacitance level sensor is fixed in the process tank to measure the level. The variable speed motor pump is attached to the collection tank and speed of the pump can be controlled by thyristor power control (TPC) unit.

2.2 Description

By means of a variable speed motor pump, water in the collection tank is pumped to the process tank. The level in the tank is measured by RF capacitance level sensor and it converts the physical quantity of level to current signal .This current signal is converted to a voltage signal using I to V converter. A newly designed VMAT01 interface board consisting of a multifunction ,high speed analog to digital converter (ADC)   and digital to analog converter (DAC) is interfaced with the PC-AT Pentium 4.The VMAT01 is capable of running the real time control algorithms in simulink tool of MATLAB platform directly. Moreover it is just like DSPACE. The voltage signal is processed and the real time control algorithm is carried out by VMAT01.

3. Materials and Methods

3.1 Model parameters and Controller settings identification

Initially the level in the tank is maintained at steady state of 40% (12 cm) of the total height. A step size of 5% in DAC output is given to the system.The variation in level in percentage is recorded against time until a new steady state is attained. From the experimental data the FOPTD model parameters such as process gain (K_p), time delay (D) and time constant (τ_p,) of the level process are determined. The identified transfer function model for the Liquid Level System is given as **G(s) = (4.31 / (22.8s+1)) exp $^{(-1.32s)}$.**Based on these model parameters the P mode controller settings are calculated by considering ZN open loop tuning rules [Ziegler and N. B. Nichols, 1942] (Kc = 4).

3.2 Repetitive Control Strategy (RCS)

Repetitive control is a simple learning control method which was designed especially for tracking a periodic reference signal and rejecting a periodic load signal. The design of repetitive control strategy (RCS) is based on the Internal Model Principle (IMP).The internal model principle **(IMP)** proposed by Wonham and Francis plays an important role in the design of the servo system. The IMP states that if any exogenous signal can be regarded as the output of an autonomous system, the inclusion of the model of the signal in a stable closed-loop system can assure perfect tracking or complete rejection of the signal.   Hara et al. has developed RCS in the year 1985.

The RCS includes the factor $\dfrac{e^{-Ls}}{1-e^{-Ls}}$ which has poles at $jk\dfrac{2\pi}{L_a}$, k = 0,±1,…..,±∞ (corresponding to the harmonic and sub harmonics of the basic period L), the controller can track any periodic signal and reject any disturbance of period L. Based on this concept, RCS is constructed with a model of $\dfrac{e^{-Ls}}{1-e^{-Ls}}$. Figure 2 shows the incorporation of RCS in the level control loop.

3.3 Periodic Signal Generator

A periodic signal generator is shown in figure 3.In periodic signal generator, any periodic signal with known period L can be generated by the time delay system. If one single period of any periodic wave is given as an input, the output will generate continuous periodic wave with one period delay. The delay should be the time of one period.

4. Results and discussions

A sinusoidal wave with known period (L=62) is generated as discussed in section 3.3. Figure 4 shows the RCS structure in a conventional P mode control loop. Real time runs of the LLS are carried out for sinusoidal periodic tracking in RCS based P mode control and the tracking responses are recorded in figure 5. To compare the RCS based P mode the runs are carried out with conventional P mode control loop and the tracking responses are recorded in figure 6.In both cases the nominal operating point of 40% of liquid level in the tank is maintained. From the figures it is observed that RCS in control loop is capable of tracking dynamic periodic reference trajectories better than the conventional P mode control loop. If the system is linear, the RCS technique can be adopted in chemical process. To analyze the robustness of the proposed structure, an experimental run of the level control system with P mode parameter using Abbas Tuning Rules (ATR) [Abbas, 1997] is carried out. Tracking responses are recorded in figures 7 and 8. The figures 9 and 10 shows the magnified tracking responses of RCS based P mode with ZNTR and ATR. From the result, the RCS based P mode with ZNTR took minimum runs (42 runs) to converge than ATR (47 runs).

5. Conclusion

In this paper a Real time implementation of RCS in a liquid level System has been made. Using step testing method the level system has been approximated to first order with delay. The Repetitive controller is developed and implemented. A comparison of the RCS-P controller with Conventional P mode is made. From the results RCS-P gives satisfactory performance over the Conventional P mode controller. Robustness of the proposed control loop is also analyzed.

References

A.Abbas. (1997). A new set of controller tuning relations, *ISA transactions*, 36(3), 183-187.

B. A. Francis and W. M. Wonham. (1975). Internal Model Principle for Linear Multivariable Regulators, *Journal of Applied Mathematics and Optimization*, 170-194.

J. H. Lee, S. Natarajan, and K. S. Lee. (2001). A Model-Based Predictive Control Approach to Repetitive Control of Continuous Processes with Periodic Operations, *Journal of Process Control*, 11, 195-207.

J.B.Ziegler and N. B. Nichols. (1942).Optimum settings for automatic controllers, *ASME Transactions,* 64, 759-768.

Rong-Fong Fung,Jeng-Sheng Huang,Chung-Gung Chien,Yun-Chen Wang. (2000). Design and application of a continuous repetitive controller for rotating mechanisms. *International Journal of Mechanical Sciences*, 42 , 1805-1819.

S. Hara, Y. Yamamoto, T. Omata, and M. Nakano. (1988). Repetitive Control-System -A New Type Servo System for Periodic Exogenous Signals, *IEEE Transactions on Automatic Control*, 33, 659-668.

Yamada.M., Riadh. Z., & Funahashi.Y. (1999). Design of discretetime repetitive control system for pole placement and application, *IEEE/ASME Transactions On Mechatronics*, 4(2), 110–118.

Zhou. K., Wang. D., & Xu. G. (2000). Repetitive controlled three-phase reversible PWM rectifier, *In Proceedings of the 2000 American control conference*, 1, 125–129.

Zhou.K., & Wang.D. (2001). Digital repetitive learning controller for three-phase CVCF PWM inverter*, IEEE Transactions on Industrial Electronics*, 48(4), 820–830.

Table 1. Specification of Liquid Level System

Variable speed motor pump		Process tank		Collection tank	
Type	Tullu - 80	Material	Acrylic	Material	Mild steel
Speed	6500 rpm	Capacity	3.5 litres	Capacity	10 litres
Discharge	800 ltr/hr	Height	30 cm		
		Diameter	15 cm		

Figure 1. Experimental setup of Liquid Level System
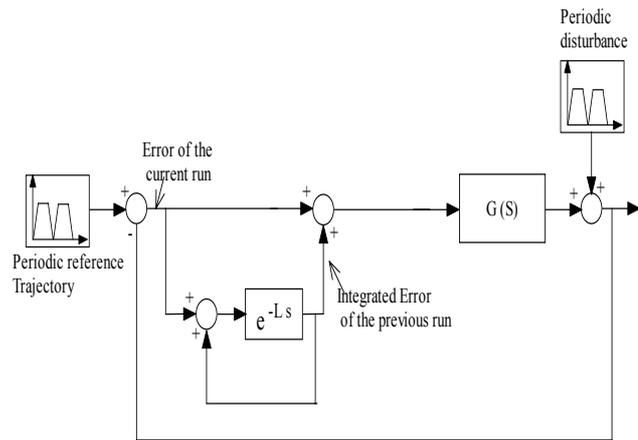
Figure 2. Repetitive Control System
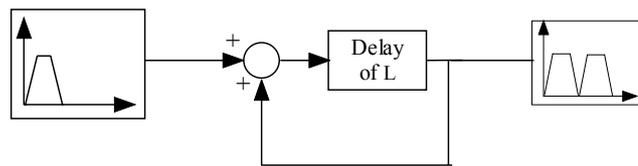
Figure 3. Periodic signal generator
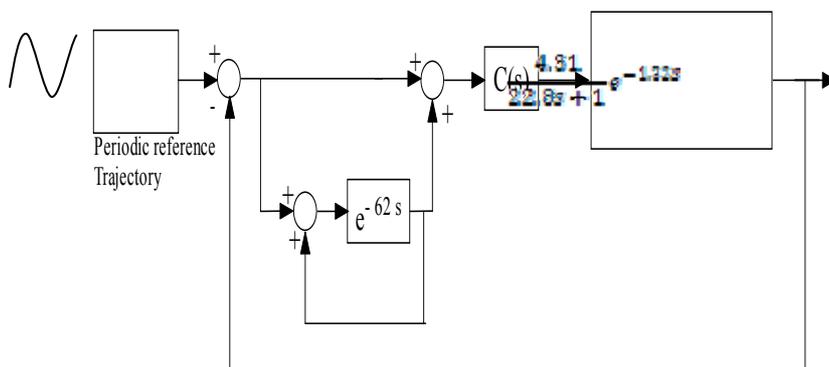
Figure 4. RCS with P mode structure in LLS
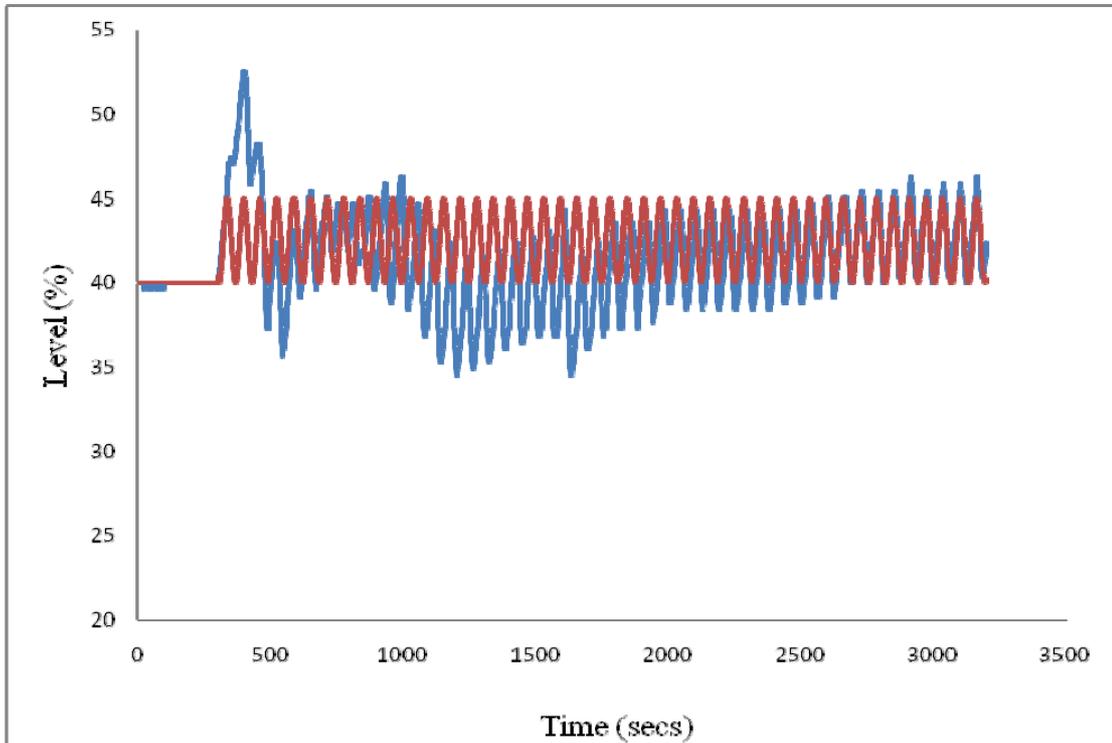
Figure 5. Tracking of periodic reference trajectories with Z-N based RCS-P mode
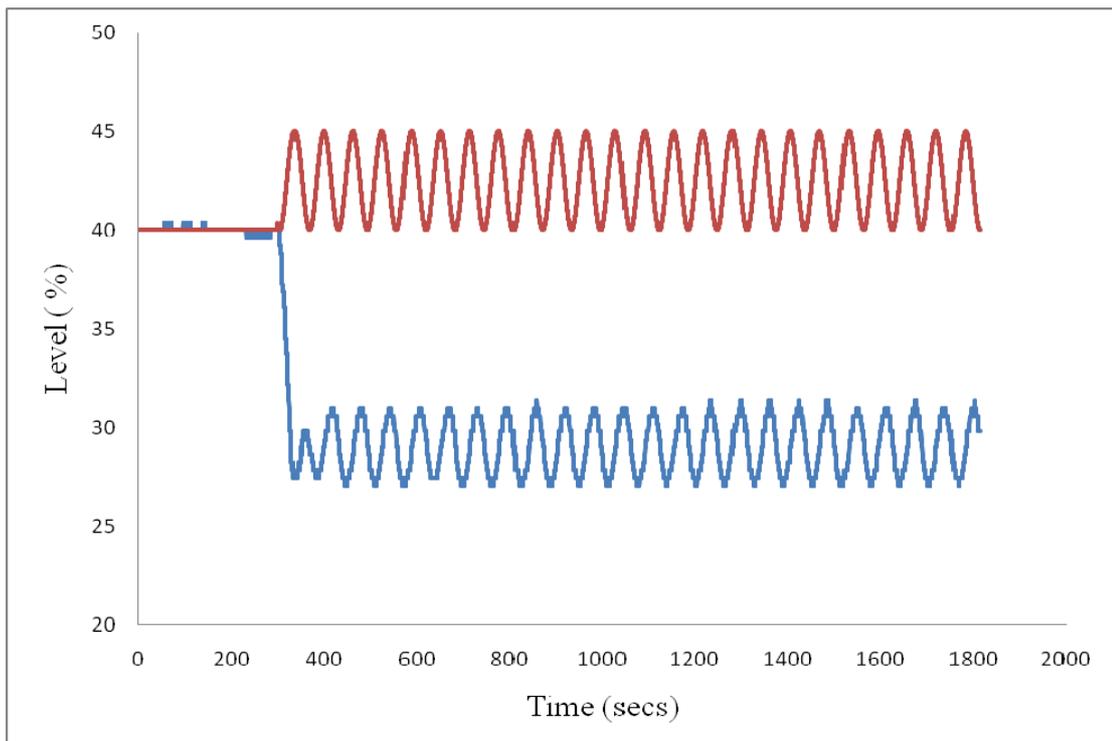
Figure 6. Tracking of periodic reference trajectories with Z-N based P mode
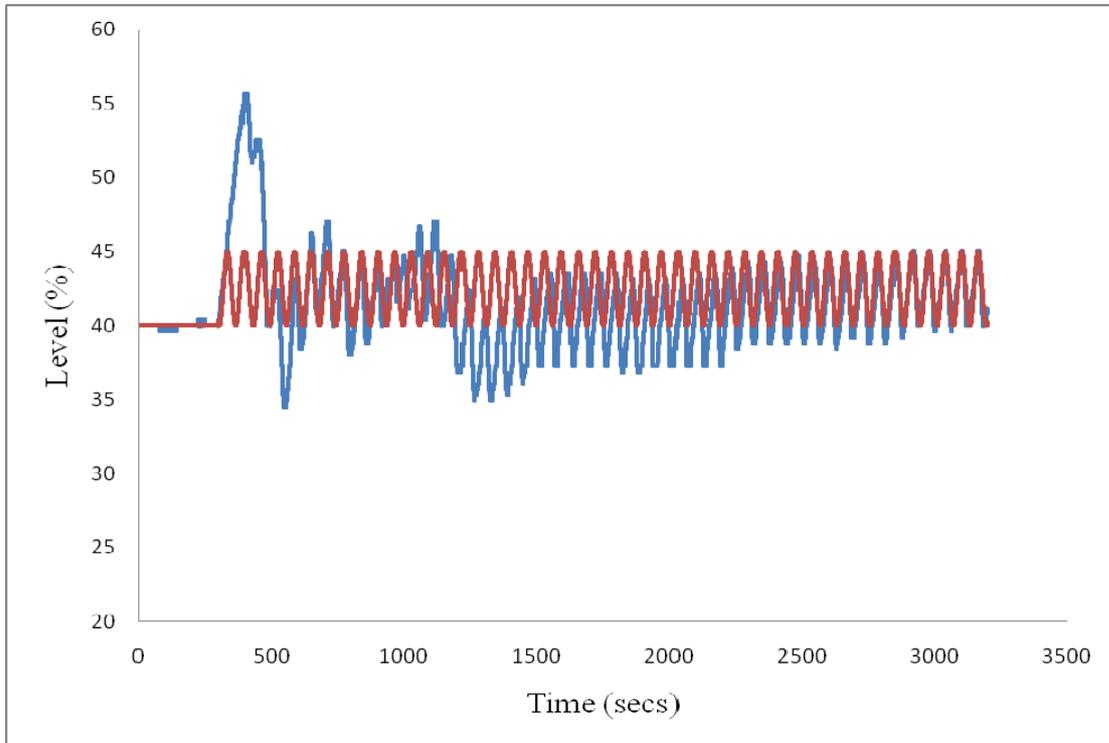
Figure 7. Tracking of periodic reference trajectories with Abbas based RCS-P mode
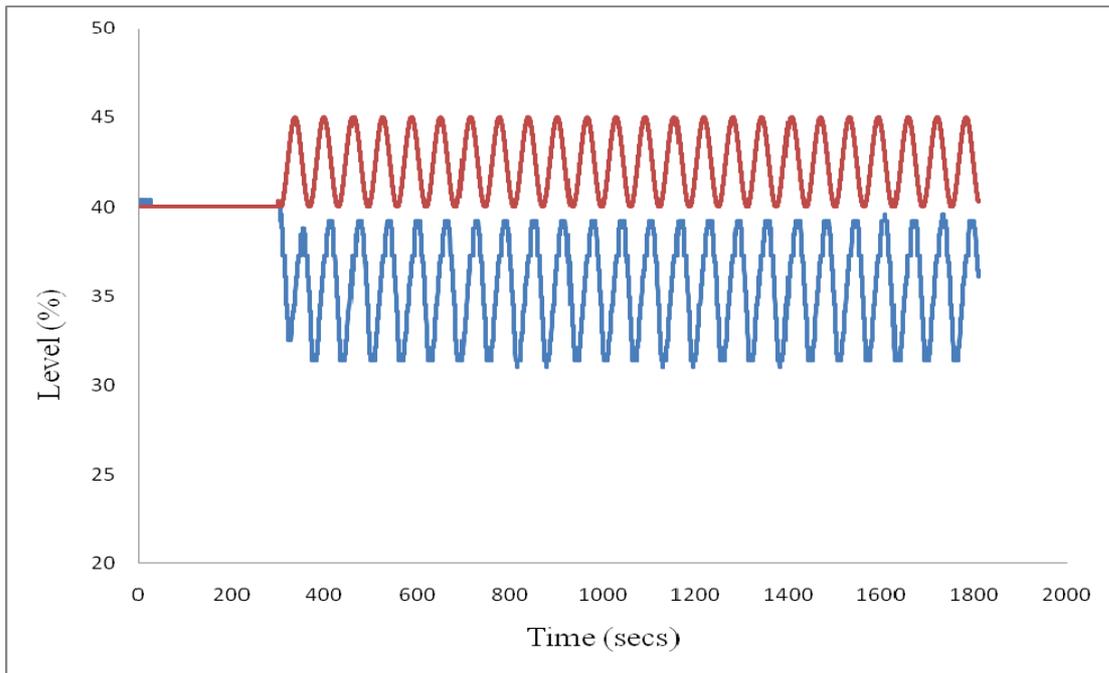
Figure 8. Tracking of periodic reference trajectories with Abbas based P mode
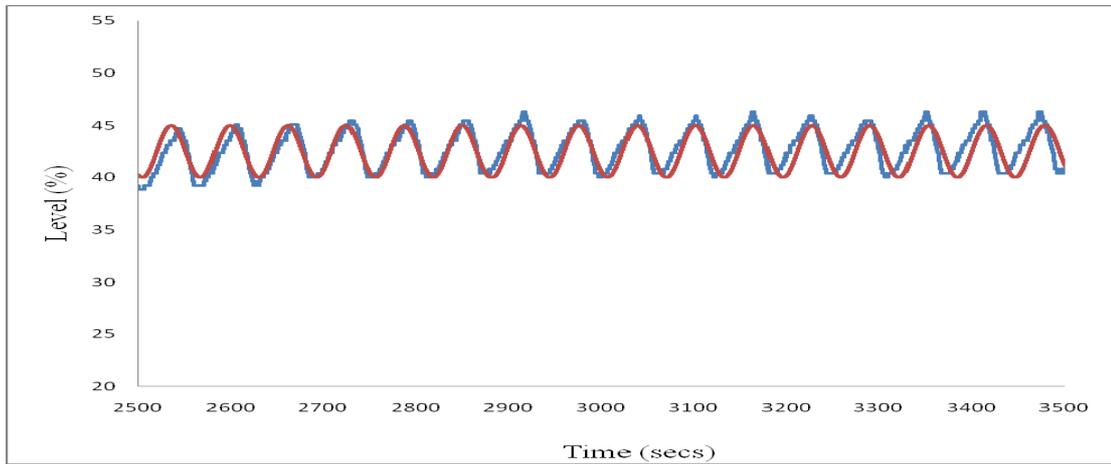
Figure 9. Magnified Tracking response of periodic reference trajectories with Z-N based RCS-Pmode
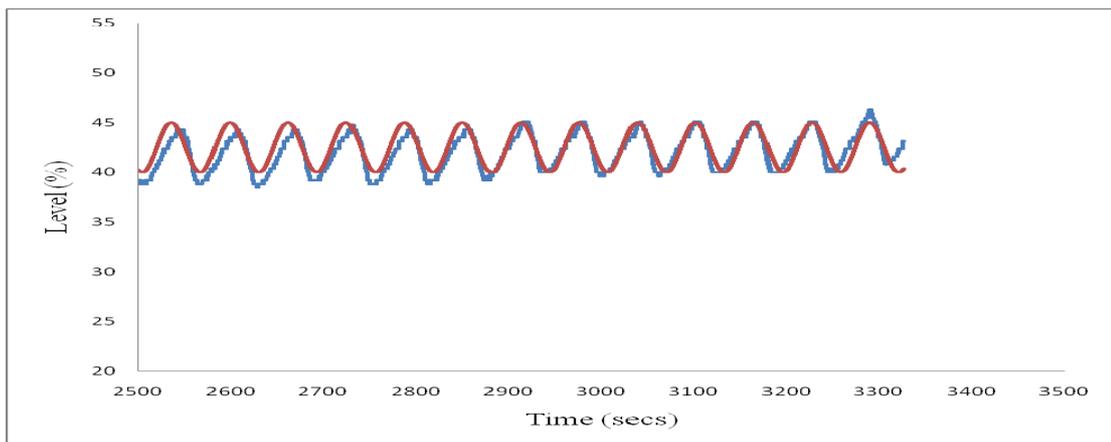
Figure 10. Magnified Tracking response of periodic reference trajectories with Abbas based RCS-P mode

Study on the Growth of the Fatigue Crack under Flexural Moment

Wen Zhong, Jiajie Hu, Jun Guo, Zibin Li & Quyue Liu

State Key Laboratory of Traction Power, Sout hwest Jiaotong University, Chengdu 610031, China

E-mail:zw1019@126.com

Abstract

Vehicles will suffer various loads in the moving process, and under the functions of various factors such as the ovality of the wheel, and the impacts to the rails when the vehicle passes the curve rail, the rail slot and the turnoff, the wheels will inevitably add normal loads to the rails, and the flexural moment will influence the generating and growth of the fatigue crack. To study the influences of flexural moment on the fatigue performances of rails with various materials, the experiments about the growth performances of the fatigue cracks of two kinds of materials including U71Mn and PD3 under the flexural moment are made on the NENE-2 fretting test machine, and according to the experiment results, the measures to reduce the fatigue of rails are proposed. The research analysis and experiment results indicate that the fatigue crack generates from the focal point of stress at first, and the main shearing stress is very important, and when the static load functions, the direction of crack growth will change by a large angle, but when the dynamic load functions, the direction of crack growth will be stable, and under same loading speed, the fatigue crack of PD3 rail more easily generates and grows than U71Mn rail. To prevent and reduce the fatigue of rails, the selection of rail should accord with the type of the route and the actual working environment of the rail, and in the heavy freight route, the PD3 rail with high mechanical strength should be selected, and in the high-speed route, the U71Mn rail should be selected.

Keywords: Rail steel, Fatigue crack, Flexural moment, Growth, Research

With the increase of railway transportation and the enhancement of train speed, the destroys induced by the wheel track rolling contact fatigues become more and more seriously, especially in the high-speed routes and the heavy freight routes (Jin, 2001, P.92-108 & Lu, 2007, P.41-54). For the mechanism of rolling contact fatigue, the prediction of crack life, the parameters with influencing functions and the methods of prevention, scholars have made large numbers of researches (Anders, 2005, P.1288-1300 & Liu, 2000, P.30-34).

The twisting force between the wheels and rails can always produce plastic distortion of rails when the train moves (Liu, 1998, P.337-340). At the same time, the ovality will occur in wheels because of various reasons (such as machining and fretting), and the normal load will occur in movements and impact the rails. In addition, when the transverse motion and the yaw motion happens in the wheel pairs, especially when the vehicle passes the curves with small radius, the rail slot and the turnoff, the impact vibration will occur between wheel tracks. But because of the installing form of the rails, the normal load will make the rails to bend and distort adown, i.e. the under-area of the rail will be elongated by the pulling function, and the top-area of the rail will be reduced by the pulling function, and the energy dissipation will be different with the pure twisting force (Jonas, 2001, P.575-586). And if the fatigue crack is generated on the surface or the hypo-surface of the rails (A. Bernasconi, 2005, P.973-980), the rails will suffer the functions of reducing or pulling. Under the function of repetitive loading, the plastic distortion will be accumulated and form micro-cracks on the surface or the hypo-surface of the materials (Liu, 2002, P.1596-1599), i.e. the flexural moment will influence the generation and growth of the fatigue cracks.

On the NENE-2 fretting test machine, the growth characters of fatigue cracks of two kinds of rails including U71Mn and PD3 are studied under the flexural moment by improving the experiment clump, and the influences of the flexural moment on the generation and growth of rail fatigue crack are analyzed as follows.

1. Experiment

1.1 Experiment equipment

The experiment is made on the NENE-2 fretting test machine, and the experiment equipment is seen in Figure 1. The whole experiment equipment is divided into the under-part and the top-part. The clump chuck and the loading chuck compose in the top-part which generates the normal load, and the simulated girder and the installing seat compose in the under-part of the equipment. To be like with the practical installing form of the rails, the bolt connection is adopted between the simulated girder and the installing seat, and two ends forms the fixed-end restriction. The installing seat is installed on the piston seat of the NENE-2 fretting test machine by the bolt, and it can realize the loading of normal load by the pumps of the pistons in the experiment.

In the experiment, the load extent is 20-350N (U71Mn), or 20-350N, or 20-200N (PD3), and the loading speed is 12mm/min.

To simulate the practical working condition, the maximum contact pressure in the experiment keeps equal with the maximum contact pressure of rails in the practical working condition (Liu, 2003, P.132-135). The size of the simulated girder (length= 220mm, breath= 8mm, height= 10mm) is confirmed by the working platform of the test machine. The crack of 0.18mm×7.5mm is prefabricated in the just middle of the simulated girder by the line cutting method.

Approximate the contact between the loading chuck and the simulated girder as the contact of two columns, and according to Hertz's contact theory,

$$R = (\frac{1}{R_1} + \frac{1}{R_2})^{-1} \tag{1}$$

Because the radius of the girder R_2 is close to ∞, so the radius of the loading chuck is

$$R = \frac{PE^*}{\pi P_0^2} \tag{2}$$

Where,

$$E^* = (\frac{1-\upsilon_1^2}{E_1} + \frac{1-\upsilon_2^2}{E_2})^{-1}.$$

Take P=55N/mm, P_0=1.2Gpa and E= 2.14×10^{5}Mpa to compute, and consider the influences of the machining precision, take the radius of the loading chuck is R=1.3mm.

1.2 Experiment materials

Take the hot rolled rails of U71Mn and PD3 from the middle of the sample rails, and their chemical components and mechanical performances are seen in Table 1 and Table 2 (Zhao, 2007).

To compare the growths of cracks, the static loading experiment is implemented. When the static load functions, the clump chuck is fixed on the bracket, and the installing seat is put on the top-pole of the hydraulic pressure jack. By moving the top-pole of the jack continually until the sample ruptures, the static load can be implemented. After the experiment, take the prefab crack part in the middle of the simulated girder, and metallographically burnish and polish it, and observe the growth conformation of the crack by the optical microscope.

2. Results and discussion

In Figure 3 and Figure 4, the crack in the static loading will turn to the large-angle of 90° when it growth to certain extent, and then grow randomly to other side. But in Figure 5 and Figure 6, the growth direction of fatigue crack is stable and changes little.

That is because when the static load functions, the energy can only rapidly release by the growth of the crack. And once the crack growth encounters the disfigurement in the interior of the material, it will change the direction at once to the direction that the edge stress of disfigurements centralizes. But because the crack will always grow to the direction that the energy consumes little, so when the direction grows to a little distance, it will return to the initial growth direction. But in the growth process of fatigue growth, the plastic distortion near the crack will consume part of energies, and make the release of energy to be slow, so the crack will grow always along the direction that the energy consumes least, and the direction will change little.

In Figure 3, Figure 4, Figure 5 and Figure 6, the generating points of the fatigue crack are located in the side of the top end of the crack round arc, not the middle of the round arc. From the analysis of the stress distribution, because the contact width is narrow, the pressure of the loading chuck can be simplified as the even distribution. According to Hertz's contact theory, ignore the influences of prefab cracks, the value of the main shearing stress is $\tau_1 = \frac{p}{\pi}\sin\alpha$, and its distribution is seen in Figure 7.

In the ideal situation of Figure 7, from the main shearing stress distribution, the point of intersection of the isoline of the main shearing stress and the round arc of the top of the prefab crack is on the round arc of the side of the middle line (the macula in the Figure), and the crack is generates at this position. The maximum point of the main shearing stress is close to the generating point of the crack, which indicates that the main shearing stress significantly influence the generating position of the crack.

By the software of ANSYS, the finite element method (FEM) is used to further analyze the stress of the simulated girder. First, establish the solid model of the simulated girder of 220×10×8, and generate the prefab crack of 7.5×0.18 by the Boolean subtraction calculating. Because the contact pressure is only related with the geometric forms of the load and contact interface, so the loading chuck can be simplified as a half column when the radius of the loading end doesn't change. Considering that the forms and the contact of the simulated girder and the loading chuck are simple, the gridding division adopts the intelligent mode of ANSYS. The two ends of simulated girder and the faces of X, Y and Z between the simulated girders are not displaced, and the load is implemented on the top of the loading end, and the load is 300N when considering the practical experiment. The friction coefficients of the round arc face of the loading chuck and the surface of the simulated girder are 0.3, and the stress distribution of the prefab crack top under the 300N normal load is seen in Figure 8 by the solving and processing of the integrator in the software. And from the Figure, the generating position and the stress centralized position of the cracks good feature of superposition.

In most situations, the crack lengths of two kinds of rails will grow with the increase of the cycle times. At the initial stage, the crack grows little, and with the time goes, the growth speed of crack increases rapidly and goes into the fatigue rupture stage, and under the loading function, the example component will be broken (Wang, 2007, P.1026-1029). By the optical microscope, the load extent of the hot rolled rail of U71Mn is 20-350N, and the under the working situation of the loading speed of 12mm/min, the obvious cracks will occur after 12000 times cycle (seen in Figure 5). After 21000 times cycle, the length of crack doesn't increase obviously with the former. The hot rolled rail steel of PD3 produces static loading crack when the loading extent is 20-350N. When the loading extent is 20-200N and the loading speed is 12mm/min, the obvious fatigue crack will occur after 4000 times, which indicates that under same loading speed and flexural function, the U71Mn has better anti-fatigue crack growth performance than PD3.

3. Conclusions

(1) The fatigue cracks generates from the focus point of the stress, and the focus point is the important factor to generate cracks, and the main shearing stress occupies important function, so the crack generates in the static loading is significantly different with the growth conformation of the fatigue crack.

(2) When the loading speeds are same, under the flexural moment produced by normal load, the fatigue crack of PD3 more easily generates and grows than U71Mn.

(3) Above analysis shows that two kinds of rail steel including PD3 and U71Mn presents different performances. With increase of railway transportation and speed, the working condition of rails will change largely. To prevent and reduce the fatigues of rails, the rail steel should be selected according to the practical working environment of rails. For example, in the heavy freight rout, the fretting is the main destroying form of rails, so the PD3 rail with high mechanical intension should be selected. But in the high-speed route, when the fatigue is the main factor, the rail of U71Mn should be selected. And for the area that the fatigue easily occurs, especially in the curve sect of rail, the rail polishing technology should be adopted to prevent the cracks in the generating stage of crack.

References

A. Bernasconi, P. Davoli, M. Filippini & S. Foletti. (2005). An integrated approach to rolling contact sub-surface fatigue assessment of railway wheels. *Wear*. No.258. P.973-980.

Anders Ekberg & Elena Kabo. (2005). Fatigue of railway wheels and rails under rolling contact and thermal loading-an overview. *Wear*. No.258. P.1288-1300.

D W Barke & W K Chiu. (2005). A review of the effects of out-of-round wheels on track and vehicle components. *Journal of Rail and Rapid Transit*. No.219. P.151-175.

Jin, Xuesong & Shen, Zhiyun. (2001). New Developments of the Rolling Contact Fatigue of Wheel Track. *Journal of the China Railway Society*. No.23(2). P.92-108.

Jonas W. Ringsberg. (2001). Life prediction of rolling contact fatigue crack initiation. *International Journal of Fatigue*. No.23. P.575-586.

Liu, Jianfeng & Wei, Qingchao. (2000). Prediction of Fatigue Service Life for Rails of High-speed Rialway. *Journal of Railway Engineering Society*. No.2. P.30-34.

Liu, Qiyue, Wang, Xiaqiu & Zhou, Zhongrong. (1998). An Investigation on Rail Corrugation. *Tribology*. No.18(4). P.337-340.

Liu, Qiyue, Zhang, Bo & Zhou, Zhongrong. (2003). Experimental Study on Rolling Wheel Corrugation. *Tribology.* No.23(2). P.132-135.

Liu, Qiyue, Zhang, Bo & Zhou, Zhongrong. (2002). The Research of Wear Characteristics on Steel Rail. *China Mechanical Engineering.* No.13(18). P.1596-1599.

Lu, Zuwen. (2007). Overall Comments on Track Technology of High-speed Railway. *Journal of Railway Engineering Society.* No.1. P.41-54.

Wang, Wenjian & Liu, Qiyue. (2007). Study on Fatigue Crack Growth Rate of PD3 and U71Mn Rail Steel. *Journal of Mechanical Strength.* No.29(6). P.1026-1029.

Zhao, Xueqin. (2007). *Study on the Forming Mechanism of Rail Contact Fatigue Cracks.* Chengdu: Master's degree thesis of Southwest Jiaotong University.

Table 1. Chemical components and contents of two kinds of rail steel

Rail steel	C%	Si%	Mn%	P%	S%
U71Mn hot rolled	0.736	0.282	1.4	0.02	0.033
PD3 hot rolled	0.793	0.712	0.771	0.022	0.014

Table 2. Mechanical performances of two kinds of rail steel under normal temperature

Rail steel	d5(%)	σ0.2(Mpa)	σb(Mpa)
U71Mn hot rolled	10	644.5	1077.5
PD3 hot rolled	10	552	964
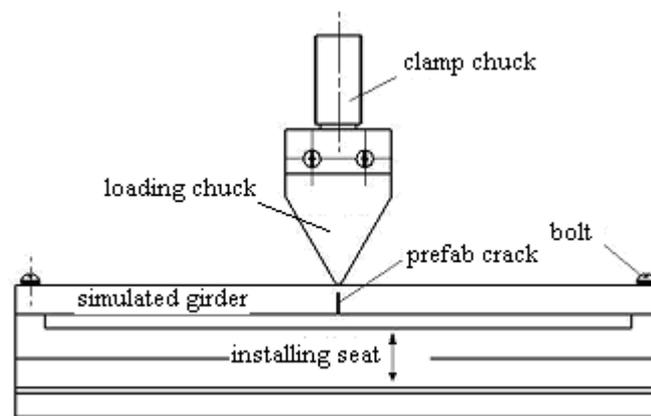
Figure 1. Sketch Map of Experiment Structure (Unit: mm)
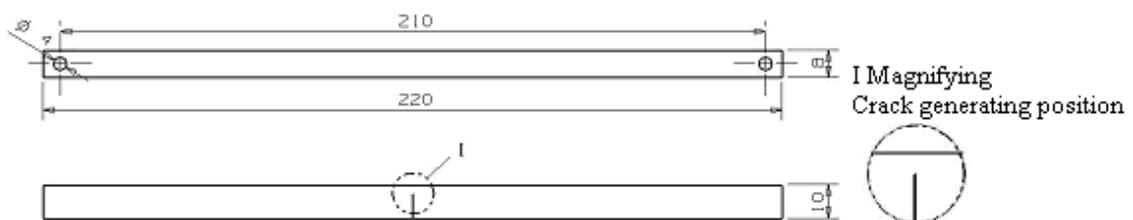
Figure 2. Sketch Map of Simulated Girder Size and Crack Generating Position (Unit: mm)

Figure 3. U71Mn Static Load Crack   Figure 4. PD3 Static Load Crack

Figure 5. U71Mn Crack after 12000 Times Fatigue   Figure 6. PD3 Crack after 4000 Times Fatigue
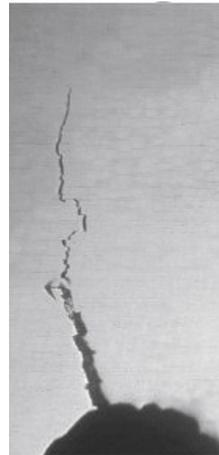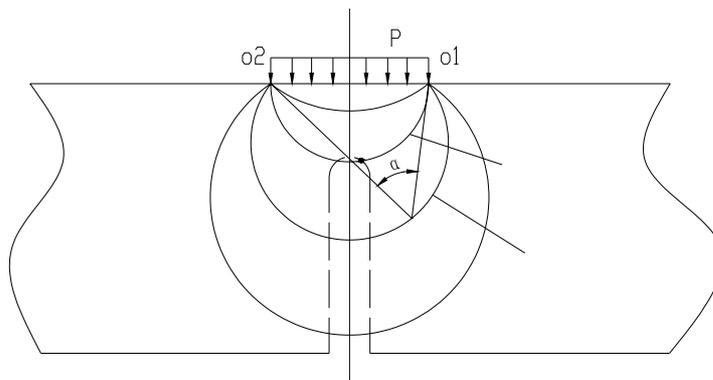
Figure 7. Simple Analysis of Main Shearing Stress of Simulated Girder
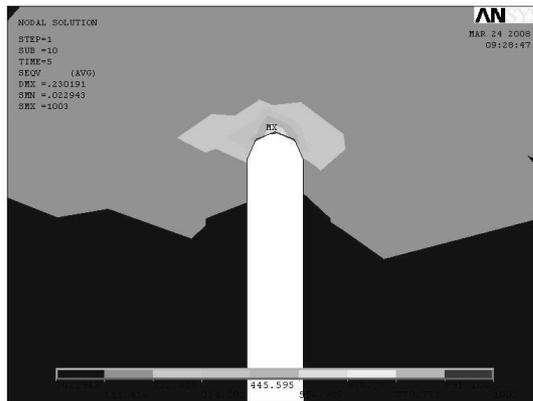
Figure 8. Equivalent Stress Distribution of Crack Top
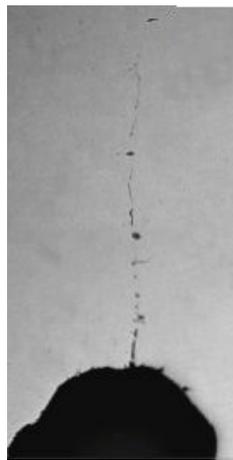
Figure 9. U71Mn Rail Steel Crack after 21000 Times Fatigue

Nonoscillation of First-order Neutral Difference Equation

Jianqiang Jia (Corresponding author)

Department of Science, Yanshan University

438 West of He Bei Avenue, Qinhuangdao 066004, China

E-mail: wyy_1246@sina.com.cn

Xiaozhu Zhong, Xiaohui Gong, Rui Ouyang & Hongqiang Han

Department of Science, Yanshan University

438 West of He Bei Avenue, Qinhuangdao 066004, China

Abstract

The oscillation of the first order neutral difference equation $\Delta[x(n) - px(n-\tau)] + qx(n-\sigma) = 0$ is studied in this paper, where $p > 0$ or $p < 0$, q is a positive constant, σ is a non-negative integer, τ is a positive integer. The sufficient conditions for nonoscillation of the equation is obtained by suitable inequality and characteristic equation.

Keywords: Difference equation, Neutral, Nonoscillation

1. Introduction

Qualitative behavior of solutions of difference equations has received considerable interest recently. In [1] the oscillation of the first order neutral difference equation

$$\Delta[x(n) - px(n-\tau)] + qx(n-\sigma) = 0 , \tag{1}$$

was considered and some oscillation criterias were given, q is a positive constant, σ is a non-negative integer, τ is a positive integer. In this paper nonoscillation of the solutions of the equation (1) are studied, where $p > 0$ or $p < 0$ and Δ is the forward difference, i.e., $\Delta x_n = x_{n+1} - x_n$.

A solution of equation (1) is called oscillatory, if it is neither finally positive nor negative. Otherwise it is called nonoscillatory.

2. main result

Lemma 1[2]   A necessary and sufficient condition for all solutions of equation (1) to oscillate is that the characteristic equation

$$F(\lambda) = (\lambda - 1)\lambda^{\sigma - \tau}(\lambda^{\tau} - p) + q = 0 \tag{2}$$

has no positive real root.

Theorem 1 Assume that $p < 0$. q is a positive constant, σ is a non-negative integer and τ is a positive integer, all solutions of equation (1) are nonoscillatory.

Proof: Since $F(\lambda) = (\lambda - 1)\lambda^{\sigma - \tau}(\lambda^{\tau} - p) + q = 0$ and $q < 0$, the equation (2) possibly has roots on interval $(1, \infty)$. Obviously $F(1) = q < 0$. From $p < 0$ we can get

$$F(\lambda) = (\lambda - 1)\lambda^{\sigma - \tau}(\lambda^{\tau} - p) + q = (\lambda - 1)\left(\lambda^{\sigma} - \frac{p}{\lambda^{\tau - \sigma}}\right) + q > (\lambda - 1)\lambda^{\sigma} + q$$

Assume that $G(\lambda) = (\lambda - 1)\lambda^{\sigma} + q$, the values of $G(\lambda)$ increase on interval $(1, \infty)$. Obviously when $\lambda \to \infty$, $G(\lambda) \to \infty$. So there is a positive constant N, such that $G(N) > 0$. From $F(\lambda) > G(\lambda)$ we can get $F(N) > 0$. So $F(N)F(1) < 0$, and $F(\lambda)$ is continuous on interval $[1, N]$, we can get there is at least a point ζ on interval $(1, N)$ such that $F(\zeta) = 0$. Therefore the equation (2) has roots on $(1, \infty)$, so all solutions of equation (1)

are nonoscillatory.

Theorem 2 Assume that $p > 0.q$ is a positive constant, σ is a non-negative integer and τ is a positive integer, all solutions of equation (1) are nonoscillatory.

Proof: When $1 > p > 0$, Obviously the equation (2) has positive roots only on $\lambda \in (1, \infty) \cup \left(0, p^{\frac{1}{\tau}}\right)$. $F(1) = q < 0$.

When $\sigma - \tau \geq 0$, the values of $F(\lambda)$ increase on interval $(1, \infty)$. Obviously when $\lambda \to \infty$, we can get $F(\lambda) \to \infty$. So there is a positive constant M_1, such that $F(M_1) > 0$. So $F(M_1)F(1) < 0$, and $F(\lambda)$ is continuous on interval $[1, M_1]$, we can get there is at least a point ξ_1 on $(1, M_1)$ such that $F(\xi_1) = 0$. Therefore the equation (2) has a root at least on interval $(1, \infty)$. So the equation (2) has a root at least on interval $(1, \infty) \cup \left(0, p^{\frac{1}{\tau}}\right)$ and all solutions of equation (1) are nonoscillatory.

When $\sigma - \tau < 0$, we can get

$$F(\lambda) = (\lambda - 1)\lambda^{\sigma - \tau}\left(\lambda^\tau - p\right) + q = (\lambda - 1)\left(\lambda^\sigma - \frac{p}{\lambda^{\tau - \sigma}}\right) + q$$

Obviously when $\lambda \to \infty$, we have $\frac{p}{\lambda^{\tau - \sigma}} \to 0$ and $F(\lambda) \to \infty$. So there is a positive constant M_2 such that $F(M_2) > 0$. So $F(M_2)F(1) < 0$, and $F(\lambda)$ is continuous on interval $[1, M_2]$, we can get there is at least a point ξ_2 on interval $(1, M_2)$ such that $F(\xi_2) = 0$. Therefore the equation (2) has a root at least on interval $(1, \infty)$. So the equation (2) has a root at least on interval $(1, \infty) \cup \left(0, p^{\frac{1}{\tau}}\right)$ and all solutions of equation (1) are nonoscillatory.

When $p = 1$, obviously the equation (2) has positive roots only on interval $(1, \infty) \cup (0,1)$. The process of the proof is similar with above-mentioned. We can get the equation (2) has a root at least on interval $(1, \infty) \cup (0,1)$. So all solutions of equation (1) are nonoscillatory.

When $p > 1$, obviously the equation (2) has positive roots only on interval $\left(p^{\frac{1}{\tau}}, \infty\right) \cup (0,1)$. The process of the proof is similar with above-mentioned. We can get the equation (2) has a root at least on interval $\left(p^{\frac{1}{\tau}}, \infty\right) \cup (0,1)$. So all solutions of equation (1) are nonoscillatory.

3. Examples

Example 1. Consider difference equation $\Delta(x_n + 2x_{n-3}) - 4x_{n-2} = 0$ where $p = -2$, $\tau = 3$, $\sigma = 2$, $q = -4$.

So the conditions in theorem 1 are satisfied and the characteristic equation is

$$F(\lambda) = (\lambda - 1)\lambda^{-1}\left(\lambda^3 + 2\right) - 4 = 0 \tag{3}$$

From the figure 1 we can see the equation (2) has a real root. Therefore all solutions of equation (1) are nonoscillatory.

Example 2. Consider difference equation $\Delta\left(x_n - \frac{1}{2}x_{n-1}\right) - 2x_{n-3} = 0$ where $p = \frac{1}{2}$, $\tau = 1$, $\sigma = 3$, $q = -2$.

So the conditions in theorem 2 are satisfied and the characteristic equation is

$$F(\lambda) = (\lambda - 1)\lambda^2\left(\lambda - \frac{1}{2}\right) - 2 = 0 \tag{4}$$

From the figure 2 we can see the equation (2) has a real root. Therefore all solutions of equation (1) are nonoscillatory.

Example 3. Consider difference equation $\Delta\left(x_n - \frac{1}{2}x_{n-3}\right) - 2x_{n-1} = 0$, where $p = \frac{1}{2}, \tau = 3$,

$\sigma = 1, q = -2$.

So the conditions in theorem 2 are satisfied and the characteristic equation is

$$F(\lambda) = (\lambda - 1)\lambda^{-2}\left(\lambda^3 - \frac{1}{2}\right) - 2 = 0 \tag{5}$$

From the figure 3 we can see the equation (2) has no real root. Therefore all solutions of equation (1) are oscillatory.

References

D A Georgiou, E A Grove and G Ladas. (1989). Oscillations of neutral difference equations, Applicable Analysis, 33(1989), 243-253.

He, Xinguang, Luo, Zhiguo, & Li, hua. (2003). Oscillation of neutrul difference equations with positive and nagative coefficients. *Journal of Mathematical Study.* 36[4]:388-393.

I Gyori, G Ladas and L Pakula. (1991). Condition for oscillation of difference equations with applications to equations with piecewise constant arguments, IAM J.Math.Anal., 22(1991), 769-773.

Li, Qiaoluan, Liu, Zhaoshuang, & Bai, Jingshan. (2004). Oscillation of First-order Neutral Difference Equation. *Journal of Hebei Normal University*. 28(6): 569-570.

Li, Yumei, Wang, Youbin, & Fan, Yehua. (2007). Qscillation of First-order Neutral Difference Equation. *Math in practice and theory*. 27(31), 188-191.

PARHIN, & TRIPATHY A K. (2003). Oscillation of a class of nonlinear neutral difference equation of higher order. *J.Math.Anal Appl*. 28(4):756-774.

SABER N E. (1995). .*An Introduction to Difference Equation*. New York: Spring-verlag.

Zhou, Yinggao, & Tang, Xianhua. (2002). Oscillation of First-order Nonlinear Delay Difference Equations. *Acta mathematical Applicatae sinica.*15(3):132-135.
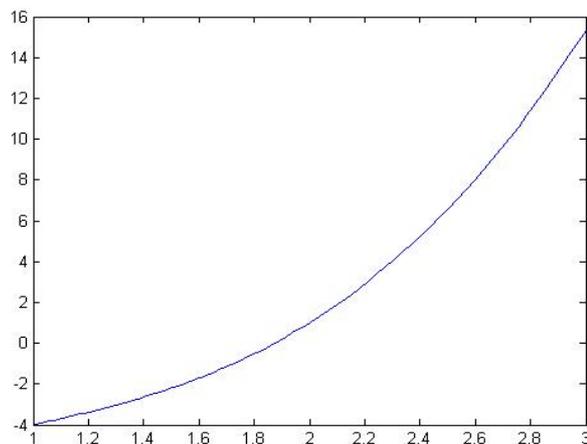
Figure 1. The figure of (3) on interval （−4,16）
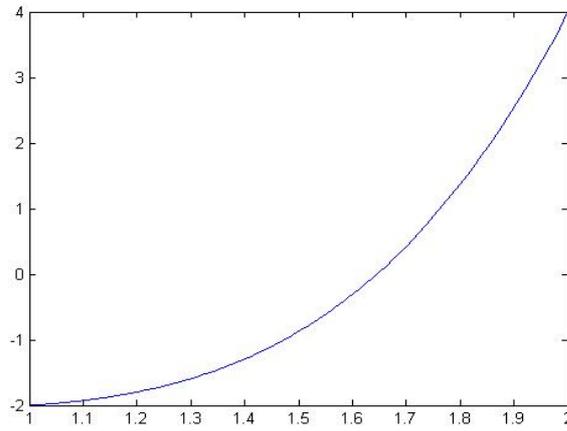
Figure 2. The figure of (4) on interval $(-2,4)$
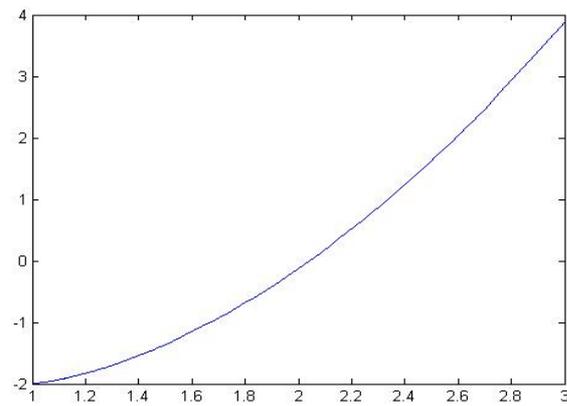
Figure 3. The figure of (5) on interval $(-2,4)$

Model-Based Feedback Control of High-speed Supercavitating Vehicles

Ziyao Cao

College of Marine Engineering

Northwestern Polytechnical University

Xi'an 710072, China

E-mail: caoziyao@nwpu.edu.cn

Abstract

Supercavitation is a means of drag reduction in water, wherein a body is enveloped in a gas layer in order to reduce skin friction. Depending on the type of supercavitating vehicle under consideration, the overall drag coefficient can be an order of magnitude less than that of a fully-wetted vehicle. However, even in its simplest conceptualization, supercavitating vehicle dynamics features slope-discontinuous force curves and time-delay effects, control presents special challenges. This paper has presented strategies for the control of the highly-coupled nonlinear system comprising a supercavitating vehicle. A three DOFs hydrodynamical model based on Newton's Laws was implemented for simulating the behavior of such a system. The linearization of the mathematical model is derived in detail. A Linear Quadratic Regulator (LQR) control design for the vehicle was formulated. Results of dynamical simulation for a specific vehicle were presented both for uncontrolled flight and with LQR-based feedforward-feedback control. The system behavior is dominated by the distinct change in the nature of the forces as the afterbody moves between a planing and non-planing condition, but that under the assumptions made for the three DOFs model the controller can eliminate the most undesirable behavior in either case.

Keywords: Supercavitation, Modeling, Linearization, LQR

1. Introduction

Supercavitation is a hydrodynamic process by which an undersea body is almost entirely enveloped in a layer of gas. Because the density and viscosity of the gas is dramatically lower than that of seawater, skin friction drag can be reduced by an order of magnitude. However, because the center of pressure is typically located well forward with respect to the center of gravity, control and maneuvering present special challenges not normally associated with fully-wetted vehicle dynamics 0. These arise from the absence of certain physical effects such as lift on the body and from the presence of other effects such as the nonlinear interaction of the control surfaces and the body with the cavity boundary. Even if the body is stable inside the cavity, the vehicle may not be stable when in contact with the cavity. Nonlinear interaction of the control surfaces and the body with the cavity wall is very important when calculating the fin and planing forces acting on the vehicle. The cavity wall exerts a large restoring force over a short period of time. The nature of this instability forces the vehicle back into the cavity, often resulting in limit cycle behavior (Dzielski et al. 2003). Cavity-vehicle interaction also exhibits strong memory effects and cavity shape is a function of the history of the vehicle motion.

This paper investigates the control challenges associated with supercavitating vehicles using a low order, longitudinal axis vehicle model. In the first part of the paper, a detailed derivation of the equations of motion for the vehicle has been carried out using Newton's Laws. Various forces experienced by different regions of the vehicle have been explained. This model draws heavily on the benchmark HSSV model proposed by Dzielski and Kurdila (2003). That two DOFs model is extended to be three DOFs and include delay dependent vehicle-cavity interaction and a more refined planing model. The second part of the paper describes linearization of the equations of motion using small disturbance theory. It is observed that the linearization, even for a simple trim, straight-level flight, can be very complicated. Thus, numerical methods are used for this purpose. The third part of the paper formulates a Linear Quadratic Regulator (LQR) control design for the vehicle. A controller is synthesized to track pitch angle, angular rate, vertical position and vertical speed for the HSSV vehicle model using the proposed approach. Simulations of the closed-loop vehicle are performed and analyzed in the fourth section of the paper. Challenges facing the model creator and control designer are highlighted with respect to actuator and sensor requirements, modeling issues, robustness and performance. The paper concludes with a summary of the results and directions for future study.

2. Modeling of Supercavitating Vehicles

Several mathematical descriptions of high speed supercavitating vehicles (HSSVs) are available in the literature (Dzielski et al. 2003) (Kirschner et al. 2003) (Kirschner et al. 2002). A one DOF longitudinal axis model was proposed to study the switching behavior of the supercavitating vehicle in (Kirschner et al. 2003). The model contains only longitudinal translational motion and its interaction with the cavity. The shape of the cavity boundary is described as a function of the time delayed position of the vehicle nose. A two DOFs longitudinal axis model for control design purposes was proposed in (Dzielski et al. 2003). The simplified model is linear within the cavity and nonlinear when the vehicle is in contact with the cavity (planing). The planing condition is defined as a function of vertical velocity and no time history dependency of the cavity is included. A high fidelity, nonlinear six DOFs mathematical model was proposed in (Kirschner et al. 2002). Lookup tables are used to calculate the forces generated by control surfaces as a function of immersion depth. The centerline of the cavity bubble is a function of the time history of the path of the vehicle nose affected by buoyancy.This paper extends the two DOFs longitudinal axis model developed in (Dzielski et al. 2003) to be three DOFs model and include the time dependent behavior of the cavity and redefines the planing condition to be a function of the vehicle vertical position, attack angle and time history of the cavity.

2.1 Geometry Setup of the Vehicle

The geometry of the vehicle being modeled is shown schematically in Figure 1. The geometry of the vehicle is intended to approximate the geometry of the actual vehicle. The body consists of a conical and a cylindrical section, where the cylindrical section is twice as long as the front conical section. The body length is denoted by *L* and its radius is *R*. The body has uniform density ρ_b (the body density is specified relative to the density of the surrounding fluid, $\rho_b = m\rho$, where ρ is the density of sea water), from which the mass and inertia are calculated.

The reference point is at the center of gravity of the vehicle, hence the vehicle mass, *M*, the moment of inertial relative to the CG fixed reference frame, I_{yy}, can be expressed using the above definitions as:

$$M = \frac{7}{9}\left(m\rho\pi\right)R^2 L \tag{1}$$

$$I_{yy} = \frac{11}{60}R^4 L\pi\rho m + \frac{1891}{45360}R^2 L^3 \rho\pi m \tag{2}$$

2.2 Reference Frame Definition

The reference frame used in modeling is shown clearly in Figure 1. The vehicle is assumed to be moving in an earth-fixed reference frame $O_e x_e z_e$, centered at any conveniently chosen point and described by the basis vector (e_x, e_z). The $O_e z_e$ axis points in the downward direction, i.e., the direction of the gravity; the $O_e x_e$ axis is placed in the vertical plane and perpendicular to $O_e z_e$. A body-fixed frame $O x_b z_b$ is defined to describe rotation of body and described by the basis vector (b_x, b_z). The frame $O x_b z_b$ is centered at O, the center of gravity of the vehicle, and moves with the vehicle. The $O_b x_b$ axis is along the vehicle's symmetry line and points to the nose of vehicle; the $O_b z_b$ axis is perpendicular to $O_b x_b$ and points downward.

The transformation matrix from **B** to **E** can be written as in

$$\begin{bmatrix} e_x \\ e_z \end{bmatrix} = \begin{bmatrix} \cos\theta & \sin\theta \\ -\sin\theta & \cos\theta \end{bmatrix}\begin{bmatrix} b_x \\ b_z \end{bmatrix} \tag{3}$$

Where, θ is pitch angle of the vehicle.

2.3 Kinematical Equations

To apply Newton's Laws, acceleration of the **CG** is required. The translational acceleration can be calculated by time differentiation of *V* in Newtonian (inertial) frame. A differentiation formula can be used to find the time derivative, in some frame, for a vector defined in some other related frame.

$$\frac{d}{dt}(\mathbf{v})\big|_I = \frac{d}{dt}(\mathbf{v})\big|_B + {}^I\omega^B \times \mathbf{v} \tag{4}$$

Where, subscript *I* denotes Newtonian (inertial) frame, and **B** is the body-fixed frame. ${}^I\omega^B$ is angular velocity of the body (or body-fixed frame) in the *I* frame, *v* is the velocity in *I* frame, of the point where acceleration is desired. Using the formula the acceleration of **CG** of vehicle in **E** frame can be obtained (*w* vertical speed, *u* horizontal speed, *q* pitch rate):

$$\begin{cases} Ax_e = \dot{u} + qw \\ Az_e = \dot{w} - qu \end{cases} \tag{5}$$

Similarly, the rotational acceleration will be required in the frame **E**. For the model is 3DOFs in vertical plane, this rotational acceleration is simply $\dot{q}$.

Now that the accelerations of various parts of the torpedo are known, Newton's Laws can be used to derive the dynamic equations of motion. Newton's Laws state that the rate of change of momentum is equal to the sum of external force applied on the body, which can also be extended to rotation. Then, the dynamic equations of motion can be obtained from Newton's Laws by an assumption that the mass of the vehicle is constant, this assumption is valid for a short period of time. The equations are:

$$\begin{cases} m(\dot{u}+qw) = \sum F_x \\ m(\dot{w}-qu) = \sum F_z \\ I_{yy}\dot{q} = \sum M \end{cases} \tag{6}$$

2.4 Forces on the Vehicle

It is assumed that when the vehicle body is fully contained in the cavity, the only hydrodynamic forces acting are due to the cavitator, immersed fins and planing.

2.4.1 Forces on Cavitator and Fins

Assuming that the cavitator drag coefficient is modeled as $C_x = C_{x0}(1+\sigma)$, where σ is the capitation number and $C_{x0} = 0.82$ (Logvinovich, 1972), the resulting force on the cavitator is approximately:

$$F_{cav} = \frac{1}{2}\pi\rho R_n^2 C_x V^2 \alpha_c = C_l V^2 \alpha_c \tag{7}$$

In the above equation, $C_l = \pi\rho R_n^2 C_x / 2$, R_n is the cavitator radius, ρ sea water density, V vehicle velocity, α_c denotes the angle-of-attack due to cavitator deflection δ_c and vertical body velocity.

The total force acting on an equivalent control surface fixed at the tail of the vehicle is modeled in relation to the cavitator force:

$$F_{fin} = -nC_l V^2 \alpha_f \tag{8}$$

Where, the parameter *n* represents the effectiveness of the control surfaces in provided lift as a function of angle-of-attack relative to the cavitator effectiveness.

In both force equations, the angle-of-attack terms are assumed to be small so that small angle approximations apply to trigonometric functions. Assuming the fins are located at the transom of the vehicle and have a moment arm L_f and the cavitator has a moment arm L_c relative to the reference point for the equation of motion, the total angle-of-attack equations are:

$$\alpha_c = \frac{w - qL_c}{V} + \delta_c \tag{9}$$

$$\alpha_f = \frac{w + qL_f}{V} + \delta_f \tag{10}$$

Where,
$$L_c = \frac{17}{28}L \quad \text{and} \quad L_f = \frac{11}{28}L.$$

Then, the forces and moments due to cavitator and fins can be calculated as:

$$\begin{cases} F_x^{cav} = F_{cav}\cos\delta_c \\ F_z^{cav} = F_{cav}\sin\delta_c \\ M_{cav} = F_x^{cav} L_c \end{cases} \tag{11}$$

$$\begin{cases} F_x^{fin} = F_{fin}\cos\delta_f \\ F_z^{fin} = F_{fin}\sin\delta_c \\ M_{fin} = F_x^{fin} L_f \end{cases} \tag{12}$$

2.4.2 Planing Force and Moment

In the original two DOFs model proposed in (Dzielski et al. 2003), the interaction of the vehicle and cavity was not a function of the cavitator position. Hence it was not delay dependent. In the extended model, the planing condition is a function of the cavity boundary and a delayed function of the cavitator position. The force and moment generated by planing are approximated by Paryshev's method (Paryshev, 2002).

$$F_p\left(h',\alpha_{im}\right)=-C_p\left(1-\left(\frac{R'}{h'(t)+R'}\right)^2\right)\left(\frac{1+h'(t)}{1+2h'(t)}\right)\alpha_{im}(t) \tag{13}$$

$$M_p = F_p \times L_f \tag{14}$$

The unknown variables are the following: C_p is a coefficient has value $\pi\rho R^2 V^2$; $h'(t)$ is the normalized immersion depth, the amount with which the body penetrates the water; $\alpha_{im}(t)$ the immersion angle, angle between the body's surface and the cavity; $R'=\left(R_c-R\right)/R$ normalized median distance between the transom and the cavity. The $h'(t)$ and $\alpha_{im}(t)$ are functions of time, because they are delay dependent, the time delay between the fluid impinging on the cavity and the aft end of the vehicle is $\tau = L/V$. The time dependence of the states and controls is suppressed in the paper unless it is needed for clarity.

The planing depth is a discontinuous functions, can be represented as:

$$h' = \begin{cases} \left[z(t)+\theta L+R-z(t-\tau)-R_c\right]/R \\ \quad if \qquad z(t-\tau)+R_c < z(t)+\theta L+R \\ 0 \qquad inside\ cavity \\ \left[z(t)-\theta L+R-z(t-\tau)-R_c\right]/R \\ \quad if \qquad z(t-\tau)-R_c < z(t)+\theta L+R \end{cases} \tag{15}$$

The position of the vehicle transom is described by the position of the vehicle nose plus a term caused by the vehicle angle radius at the transom. The cavity's boundary is located at R_c distance from the cavity centerline position $z(t-\tau)$, the immersion is the difference between the two. The immersion angle is also determined by the planing location:

$$\alpha_{im} = \begin{cases} \theta - \dfrac{w(t-\tau)}{V}-\dfrac{\dot{R}_c}{V} & (bottom\ \text{contact}) \\ 0 & (no\ \text{contact}) \\ \theta - \dfrac{w(t-\tau)}{V}+\dfrac{\dot{R}_c}{V} & (top\ \text{contact}) \end{cases} \tag{16}$$

Where $\dot{R}_c$ denotes the contribution from the fact that the cavity radius is usually contracting in the region of the planing location and this can have a significant effect on the apparent angle-of-attack.

To simplify the following equations and assuming that the body planes at the approximate location of the fins *L*, two numerical constants are defined by:

$$k_1 = \frac{L}{R_n}\left(\frac{1.92}{\sigma}-3\right)^{-1}-1 \tag{17}$$

$$k_2 = \left(1-\left(1-\frac{4.5\sigma}{1+\sigma}\right)k_1^{(40/17)}\right)^{1/2} \tag{18}$$

The expression for the radius of the cavity at a distance L from the cavitator is

$$R_c = R_n\left(0.82\frac{(1+\sigma)}{\sigma}\right)^{1/2}k_2 \tag{19}$$

And the expression for the contraction rate of the cavity $\dot{R}_c$ is

$$\dot{R}_c = -\frac{20}{17}\left(0.82\frac{1+\sigma}{\sigma}\right)^{1/2}V\left(1-\frac{4.5\sigma}{1+\sigma}\right)k_1^{(23/17)}\bigg/\left(k_2\left(\frac{1.92}{\sigma}-3\right)\right) \tag{20}$$

The equations for the cavity shape that are presented here are valid only if the following constraint on the length is

satisfied:

$$L > R_n \left(\frac{1.92}{\sigma} - 3 \right) \tag{21}$$

The above equations describe the dynamic behavior of an HSSV; these equations must be complemented with a s kinematics equation for depth in frame E

$$\dot{z} = -u \sin \theta + w \cos \theta \tag{22}$$

Then, substituting equations about forces and moments (11)~(14) into equation(6), the equation of motion for the supercavitating vehicles restricted to the vertical plane become:

$$\begin{cases} \dot{z} = -u \sin \theta + w \cos \theta \\ \dot{u} = \left(F_x^{cav} + F_x^{fin} \right) / M - qw - g \sin \theta \\ \dot{w} = \left(F_z^{cav} + F_z^{fin} \right) / M + qu + g \cos \theta \\ \dot{q} = \left(F_z^{cav} L_c + F_z^{fin} L_f + F_p L_f \right) / I_{yy} \\ \dot{\theta} = q \end{cases} \tag{23}$$

3. Control Design of Hssvs

3.1 Linearization

The equations of motion, as in the case of a supercavitating vehicle, are represented by a set of first-order differential equations.

$$\dot{\mathbf{x}} = \mathbf{f} (\mathbf{x}, \mathbf{u}) \tag{24}$$

Using $\mathbf{f} : \square^n \to \square^n$ as a nonlinear function of a time-varying vector $\mathbf{x} \in \square^n$ and $\mathbf{u} \in \square^n$. For control design, the system dynamics are observed at some trim conditions by giving perturbations to states of the system at that trim. The dynamics associated with these perturbations are obtained by linearization. An advantage by linearization is that most of the control methodology is based on linear equations of motion. A controller is designed initially for the linear system and then tested for the actual nonlinear system.

We determine the linearization for the planar vehicle about a steady state. We chose five states, let $\mathbf{x} = (z, u, w, q, \theta)^T$ and let $\mathbf{u} = (\delta_c, \delta_f)^T$. Assuming the operating point is $\mathbf{x}_0 = (z_0, u_0, w_0, q_0, \theta_0)^T$ and $\mathbf{u}_0 = (\delta_{c0}, \delta_{f0})^T$, Define

$$\Delta \mathbf{x} = \mathbf{x} - \mathbf{x}_0$$

$$\Delta \mathbf{u} = \mathbf{u} - \mathbf{u}_0$$

Then the linearized system is

$$\Delta \dot{\mathbf{x}} = A \Delta \mathbf{x} + B \Delta \mathbf{u} \tag{25}$$

Where A and B are defined as shown in (26) and (27). Here:

$$\alpha_u^c = \alpha_u^f = -\frac{w_0}{V_0^2} \quad \alpha_w^c = \alpha_w^f = \frac{u_0}{V_0^2}$$

$$\alpha_q^c = \frac{-L_c}{V_0} \quad \alpha_q^f = \frac{L_f}{V_0}$$

$$F_u^{cav} = C_l \left(2u_0 \alpha_u^c - w_0 \right)$$

$$F_w^{cav} = C_l \left(2w_0 \alpha_w^c + u_0 \right)$$

$$F_u^{fin} = -nC_l \left(2u_0 \alpha_u^f - w_0 \right)$$

$$F_w^{fin} = -nC_l \left(2w_0 \alpha_w^f + u_0 \right)$$

$$F_q^{cav} = -\frac{C_l L_c}{V_0} \quad F_q^{fin} = -\frac{nC_l L_f}{V_0}$$

Where we have abbreviated $\partial\alpha_c/\partial u$ as α_u^c, etc., and

$$a_{15} = -u_0 \cos\theta_0 - w_0 \sin\theta_0$$

$$a_{22} = \left(F_u^{cav}\cos\delta_{c0} + F_u^{fin}\cos\delta_{f0}\right)\big/M$$

$$a_{23} = \left(F_w^{cav}\cos\delta_{c0} + F_w^{fin}\cos\delta_{f0}\right)\big/M - q_0$$

$$a_{24} = \left(F_q^{cav}\cos\delta_{c0} + F_q^{fin}\cos\delta_{f0}\right)\big/M - w_0$$

$$a_{32} = \left(F_u^{cav}\sin\delta_{c0} + F_u^{fin}\sin\delta_{f0}\right)\big/M + q_0$$

$$a_{33} = \left(F_w^{cav}\sin\delta_{c0} + F_w^{fin}\sin\delta_{f0}\right)\big/M$$

$$a_{34} = \left(F_q^{cav}\sin\delta_{c0} + F_q^{fin}\sin\delta_{f0}\right)\big/M + u_0$$

$$a_{42} = \left(F_u^{cav}L_c\cos\delta_{c0} + F_u^{fin}L_f\cos\delta_{f0}\right)\big/I_{yy}$$

$$a_{43} = \left(F_w^{cav}L_c\cos\delta_{c0} + F_w^{fin}L_f\cos\delta_{f0}\right)\big/I_{yy}$$

$$a_{44} = \left(F_q^{cav}L_c\cos\delta_{c0} + F_q^{fin}L_f\cos\delta_{f0}\right)\big/I_{yy}$$

$$A = \begin{bmatrix} 0 & -\sin\theta_0 & \cos\theta_0 & 0 & a_{15} \\ 0 & a_{22} & a_{23} & a_{24} & -g\cos\theta_0 \\ 0 & a_{32} & a_{33} & a_{34} & -g\sin\theta_0 \\ 0 & a_{42} & a_{43} & a_{44} & 0 \\ 0 & 0 & 0 & 1 & 0 \end{bmatrix} \qquad (26)$$

$$B = \begin{bmatrix} 0 & 0 \\ -F_{cav}\big|_{x_0}\sin\delta_{c0} & -F_{fin}\big|_{x_0}\sin\delta_{f0} \\ F_{cav}\big|_{x_0}\cos\delta_{c0} & F_{fin}\big|_{x_0}\sin\delta_{f0} \\ \dfrac{-F_{cav}\big|_{x_0}\sin\delta_{c0}}{I_{yy}} & \dfrac{-F_{fin}\big|_{x_0}\sin\delta_{f0}}{I_{yy}} \\ 0 & 0 \end{bmatrix} \qquad (27)$$

The notation $(\bullet)\big|_{x_0}$ indicates that the quantity is to be evaluated at x_0. This linearization can be used to check features of a given vehicle design, e.g., to check stability or controllability of a desired motion mode given a choice of vehicle design parameters. One can also use this linearization to help automate the design procedure.

3.2 Control Design Setup

There are various control methods, like linear quadratic regulator (LQR) synthesis, μ-synthesis etc., which can be used to design a controller. Each of these methods has advantages and disadvantages.

LQR method gives a constant gain controller which considers the problem of robustness only in terms of gain and phase margins. It is a standard linear optimal control design method which produces a stabilizing control law that minimizes a cost function that is a weighted sum of the squares of the states and input variables. We assume that all of the states are available for feed back. If this were not the case, then, it is possible to design an estimator to determine the unmeasured states.

It is assumed that knowledge of the system state is accurate, ignoring high-frequency hydrodynamic noise excitation and other noise sources. However, the nonlinearity of the vehicle-cavity system has been retained. Nonlinearity enters the system via the vehicle planing behavior, due to the nonlinear force coefficients and to memory effects associated with cavity evolution. Control has been implemented via LQR. Cavity memory effects and the discontinuities in the force coefficients require incorporation of the feedforward model to maintain acceptable system performance. The current investigation focused on the simplified system is shown in Figure 2.

For the simplified system, the input to the LQR controller is the error vector, $\Delta x = x_d - x_a$, computed as the difference between the commanded state vector, x_d, and the corresponding actual state vector, x_a. Both the actual and commanded state vectors have the form: $\{z, u, w, q, \theta\}^T$. A classical regulator would provide a control vector, *u*, directly

to the hydrodynamic control effectors (here, the fins and cavitator): $\mathbf{u} = \left(\delta_c, \delta_f \right)^T$. However, the control vector of interest involves both the feedback output form the LQR, $\mathbf{u}_r$, and output from the feedforward model, $\mathbf{u}_f$: $\mathbf{u} = \mathbf{u}_r + \mathbf{u}_f$. The feedforward model investigated in our work is specialized for supercavitating vehicle planing dynamics. A scheme has been selected about one of two distinct fixed points in straight flight:

$$u_f \in \begin{cases} u_1 & \text{fin supported, no planing} \\ u_2 & \text{planing, zero fin deflection} \end{cases} \tag{28}$$

The point selected depends on the planing operating condition.

Regulation for the general LQR is measured by the quadratic performance criterion

$$J\left(\mathbf{u}\right) = \int_{t=0}^{\infty} \left(\Delta\mathbf{x}^T \mathbf{Q} \Delta\mathbf{x} + 2\Delta\mathbf{x}^T \mathbf{N} \mathbf{u}_r + \mathbf{u}_r{}^T \mathbf{R} \mathbf{u}_r \right) dt \tag{29}$$

Where the user-specified weighting matrices, **Q**, **N**, and **R**, define the trade-off between regulation performance and control effort. Once the state and control matrices have been obtained, the main variables that the LQR controller depends on are the weighting matrices **Q**, **R** and **N**. In this case the cross coupling matrix **N** is chosen to be zero. The matrices **Q** and **R** penalize the cost function for higher state and control values respectively. A higher value in **Q** matrix would cause a better tracking. A larger **R** would constrain the control surface deflection. An optimum combination of the matrices is obtained iteratively, so as to get good tracking with achievable control deflections.

A MATLAB$^\text{R}$ control system Toolbox routine is used to determine the gain matrices, K_s, which minimize the cost function. *J(u)*, for use in the state feedforward-feedback control law (MATH WORKS, 1998) for each of the two fixed points considered. The control law is then expressed as:

$$\mathbf{u} = \mathbf{u}_{fs} - K_s \mathbf{x} \quad s \in \{1, 2\} \tag{30}$$

A substantial portion of the current work is devoted to testing various combinations of the weighting matrices **Q** and **R** to achieve acceptable performance. The weighting and gain matrices are all computed prior to flight simulation.

4. Results of Simulations

The specific set of parameter values used in our simulations is as follows (Dzielski et al. 2003): g=9.81m/s2, m=2, R_n = 0.0191m, R=0.0508m, L=1.8m, V_0=75m/s, σ=0.03, n=0.5, C_{x0}=0.82.

We control the vehicle to maintain a desired operating point:

$$\left(\bar{z}, \bar{u}, \bar{w}, \bar{q}, \bar{\theta} \right) = \left(0, 75, 0, 0, 0 \right)$$

The matrices for state tracking are given as follow:

$\mathbf{Q} = diag\left(\left[10, 0, 1, 0, 0.5 \right] \right)$

$\mathbf{R} = diag\left(\left[3, 1 \right] \right)$

The simulation results are shown in Figure 3 and Figure 4. We can see that, in short period of time (one second), the uncontrolled case started with violent tail-slap behavior and undergone a limit cycle oscillations. This could be explained as that the transom of vehicle without control was fast immersed in the bottom of the cavity, the resulting planing force acts in the opposite direction of the immersion, providing a large force to bounce the body back into the cavity, leading to oscillatory motion like a fast boat bouncing on the top of water.

More interestingly, the results in (Dzielski et al. 2003) indicated that the two DOFs model system had no equilibria in erither region, only the closed-loop system with control had equilibrium point., whereas the motion of our three DOFs system in uncontrolled case is a kind of attenuation oscillation around a equilibrium point:

$$\left(\bar{z}, \bar{u}, \bar{w}, \bar{q}, \bar{\theta} \right) = \left(0.09229, 74.848, 0.1229, 0, 0.0251 \right)$$

We can change our points of view into kinetic energy: the horizontal speed of two DOFs model was restricted to constant, the energy contributed by planing force accumulated continuously and resulted in non-limit motion. For our three DOFs model, since there is no propulsion in the system, the horizontal speed is reduced extremely, so the sum kinetic energy of the vehicle system is decreasing and a limit cycle oscillation motion can be obtained..

As shown in Figure 4, the uncontrolled case is dominated by a continuous skipping mode, whereas our controller eliminates this mode. The planing force history indicates that skipping occurs in both cases – apparently the controlled response during the planing portion of the vehicle is sufficient to mitigate the unsteady cavity behavior in such a manner that the afterbody excursions are not so extreme.

5. Summary

This paper describes the control challenges associated with supercavitating vehicles. The feedback control problem features a delay dependent system with significant nonlinearities affecting the design. There are a number of open questions to be resovled before such a vehicle can be successfully controlled. These include:

- The current model assumes all the states are available for the feedback. A detailed study of the sensors is required. The available sensors and their characteristics affect the actual performance of the controller.

- The LQR controllers obtained are typically known as the 'inner-loop' controllers. An outer-loop controller is also needed for guidance and navigation.

- Robustness of feedback controller to modeling errors and poor physical models.

The performance and robustness requirements facing the design of a feedback controller will significantly shape the design of future supercavitating vehicles.

References

ANUKUL GOEL. (2005). Robust control of supercavitating vehicles in the presence of dynamic and uncertain cavity. Florida:University of Florida.

Arndt REA, Balas GJ, Wosnik M. (2005). Control of cavitating flows: A perspective. *Japan Society of Mechanical Engineers International Journal*, Japan.

B.Vanek, J.Bokor, and G.J.Balas. (2006). Developmets in high-speed underwater vehicle control. *J.Vibration and Control*.

B.Vanek, J.Bokor, and G.J.Balas. (2006). Theoretical aspects of high-speed supercavitation vehicle control. *American Control Conference*. Minneapolis.

Ivan N.Kirschner, James S.Uhlman. (2006). Overview of High-speed supercavitating vehicle control. AIAA Guidance, *Navigation and Control Conference and Exhibit*. Keystone, Colorado.

John Dzielski, Andrew Kurdila. (2003). A benchmark control problem for supercavitating vehicles and an initial investigation of solutions . *Journal of Vibration and control*.vol.9,no,pp.791-804.

Kirschner IN, Kring DC, Stokes AW, Uhlman JS. (2002). Control strategies for supercavitating vehicles. *Vibration and Control* 8:219-242.

Kirschner IN, Rosenthal B.J, Uhlman JS. (2003). Simplified dynamical system analysis of supercavitating high-speed bodies. *Fifth International Symposium on Cavitation*, Osaka Japan.

Logvinovigh GV. (1972). Hydrodynamics of free-boundary flows. NASA-TT-F-658, *US Departmet of Commerce*, Washington D.C.

Paryshev EV. (2002). The plane problem of immersion of an expanding cylinder through a cylindrical free surface of variable radius. *International Summer Scientific School on High-Speed Hydrodynamics*, Cheboksary, Russia.

Savchenko Yu N. (2001). Control of Supercavitating Motion of Bodies, *VKI Special Course on Supercavitating Flows*, Brussels: RTO-AVT and VKI. RTO-EN-010(11).

Shao Y, Mesbahi M, Balas GJ. (2003). Planing, switching and supercavitating flight control. *AIAA Guidance, Navigation and Control Conference*, AIAA-2003-5724.
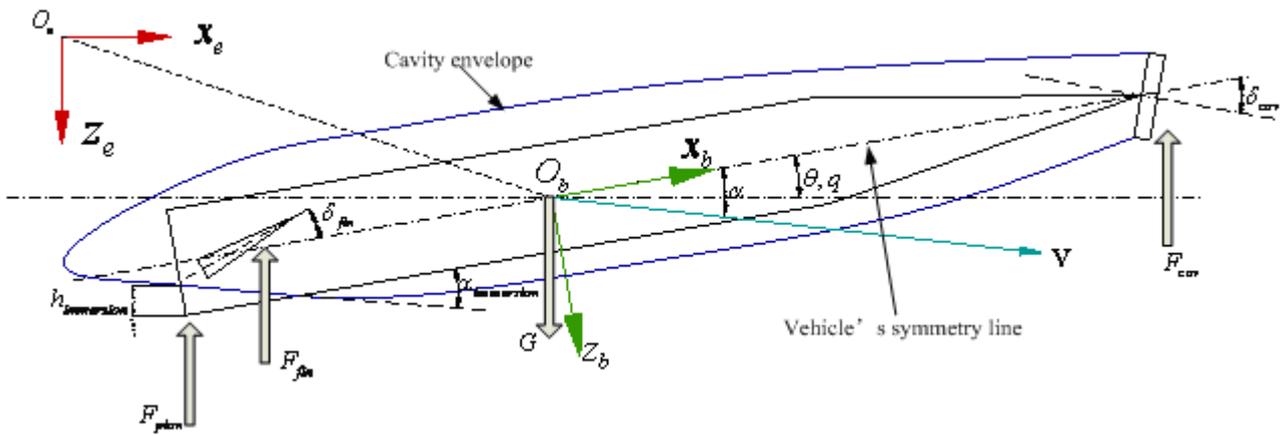
Figure 1. Schematic diagram of 3 DOFs model
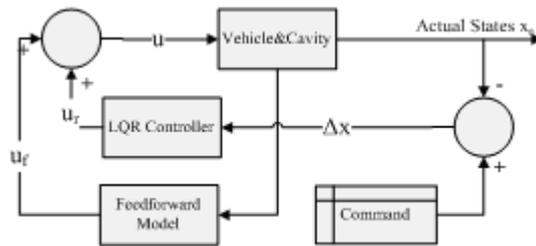
Figure 2. Simplified dynamical systems model of a supercavitating vehicle
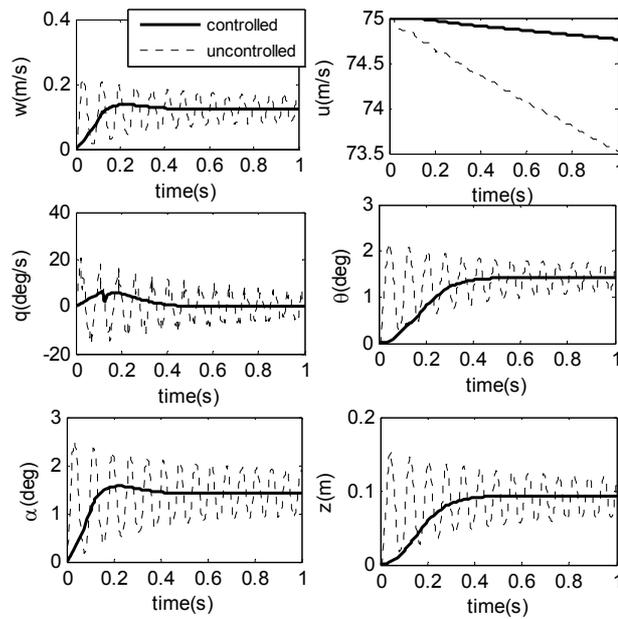
Figure 3. Simulation results of HSSV (w,u,q,θ,α,z)
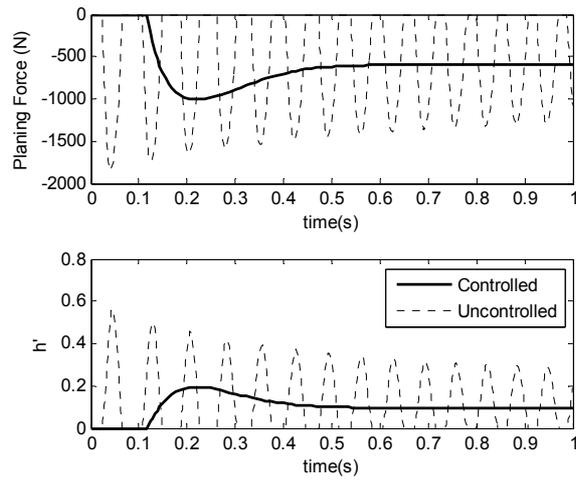
Figure 4. Simulation results of HSSV (Fp, h')

Research on Next Generation Dynamic Host Configuration

Protocol and Security of Application

Ziqian Xiao, Jingyou Chen & Chaobo Yang

Department of Software Engineering, Hainan Software Profession Institute

Qionghai 571400, China

E-mail: xiaoziqian1234@163.com

Abstract

In this paper, the author studies on next generation of Dynamic Host Configuration Protocol (DHCPv6), expounds the principle of DHCPv6 and its message exchange process. And also point out that the security issues may exist, hence several strategies have been put forward to improve the safety of message exchange, as well as the security of network. The author discusses DHCPv6 as being independent of its interaction with Neighbor Discovery in this paper.

Keywords: Stateless Services, Identity Association, Message exchange, Relay Agents

1. Introduction

With the Internet's rapid development and expansion, IP address is about to face the depletion of resources. The next generation of IP Protocol (Ipv6) is ripe in theory. Although there are many problems in transition, we will eventually enter the world of IPv6. In IPv6 networks, the number of fixed nodes will become mobile. How to quickly and easily allow network nodes to connect to the Internet is a major issue we are facing. The current DHCPv4 resolved auto-configuration of network nodes, however, in the IPv6 network DHCPv6 will play as the protagonist, which will become indispensable to the future of network members, DHCPv6 is developed from the DHCPv4, more simple and more powerful. Unavoidably, some security issues existed. After the study on DHCPv6, we found that some strategies can be adopted to improve the security of the application of DHCPv6.

2. Define about DHCPv6

2.1 DHCP Unique Identifier (DUID)

A DHCP Unique Identifier (DUID) is variable length data which uniquely identifies each individual DHCPv6 client or server. This is similar to the client or server identifier in DHCPv4, but is designed to ensure better uniqueness of the identifier among all clients and servers; [RFC3315] defines a standard format of DUIDs in order to help ensure that DUIDs are unique. They are the following three types: DUID-LLT, DUID-EN and DUID-LL, Figure 2.1 shows the detailed characteristics of their respective.

In Figure 2.1, DUID-EN in the Enterprise-number refers to IANA for a specified integer manufacturers, Identifier manufacturers refer to each specific marking of variable length.

2.2 Identity Association

An Identity Association (IA) is a conceptual structure that identifies a set of DHCPv6 configuration information. Each IA is identified by a 32-bit identifier (Identity Association Identifier, IAID). An IAID must uniquely identify one particular IA within each client. The notion of an IA was introduced in DHCPv6 because of the property of IPv6 that an interface can have multiple IP addresses. The primary goal of IAs is to define multiple identities within a single client, each of which is associated with a different IPv6 address. The lease duration is managed per IA, not per address. Three types of IA:

• Identity association for non-temporary addresses (IA_NA): An IA_NA defines a set of normal, that is, not temporary; IPv6 addresses to be allocated for a client's interface. Addresses in an IA_NA are expected to be used as long as the client wants to renew these addresses as necessary.

• Identity association for temporary addresses (IA_TA): An IA_TA defines a set of temporary IPv6 addresses to be allocated for a client's interface, where temporary refers to the privacy extension. Due to the nature of temporary addresses, an IA_TA does not have the T1 and T2 parameters and is not expected to be renewed.

• Identity association for prefix delegation (IA_PD): An IA_PD defines a set of IPv6 prefixes to be allocated from a delegating router to a requesting router for prefix delegation. Like IA_NA, an IA_PD is expected to be renewed using the T1 and T2 parameters.

2.3 Binding

A binding is a conceptual structure maintained by a server, which represents particular configuration information currently assigned to a client. For configuration information associated with an IA, the binding is identified by the tuple of <client's DUID, IA-type, IAID>, where IA-type is one of IA_NA, IA_TA, and IA_PD.

3. Working principle of DHCPv6

All DHCPv6 messages are carried in IPv6 UDP packets. The following well-known IPv6 addresses and UDP ports are used in DHCPv6 exchanges:

• All_DHCP_Relay_Agents_and_Servers (ff02::1:2): The well-known link-scope multicast address for relay agents and servers. All relay agents and servers must join this group on the interface accepting incoming messages.

• All_DHCP_Servers (ff05::1:3): The well-known site-scope multicast address for servers. All servers must join this group on the interface accepting incoming messages.

• UDP port 546: The well-known UDP port that clients listen on.

• UDP port 547: The well-known UDP port that servers and relay agents listen on.

3.1 Message Name and Descriptions

Table 1 lists message name and descriptions.

3.2 Common Message exchange process

The DHCPv6 protocol consists of various types of message exchanges. The exchanges for some common scenarios will be described next.

a. Exchanges for Address Allocation

A client starts DHCPv6 exchanges for address allocation with a Solicit message specifying an IA_TA or IA_NA for which the client wants to configure addresses. Servers receiving the Solicit message consult their local configurations, determine whether they can allocate addresses for the IA, and return Advertise messages containing their offers. When a server prepares the Advertise message, it attempts to send the same options that it will send to the client in its Reply message if the client chooses this server. This allows the client to compare the options and addresses advertised by different DHCP servers and choose the set of options and addresses that fit its particular needs. In practice, the contents of the Advertise message may not matter much; the client may simply choose the server that sends the first Advertise message as long as the server has the same preference.

Figure 3-1 shows that there are two servers, server1 and server2, respond to the Solicit message, and the client selects server1.

In Figure 3-1, Client receive the advertise message which send by Server1 earlier, so Client choose Server1 as DHCP server. And this can be done using the Rapid Commit option. The use of the Rapid Commit option primarily assumes an environment where at most one server is available for the client.

b. Exchanges for Prefix Delegation

DHCPv6 message exchanges for prefix delegation are mostly the same as those for address allocation described before with the following minor exceptions:

• The Confirm and Decline messages are not used for prefix delegation.

• When the requesting router (i.e., the DHCPv6 client) detects that it may have attached to a new uplink, it uses Rebind and Reply exchanges to confirm the previous binding, instead of using the Confirm message.

c. Exchanges for the Stateless Services

For the stateless DHCPv6 service—that is, getting configuration information that does not need per-client binding—Information-request and Reply exchanges are used. These exchanges are simple: the client sends an Information-request message, usually without including the DUID of any particular server. Servers receive the message, and respond with a Reply message containing any stateless configuration information. But this simple mechanism has turned out to be insufficient in practice, due to the lack of renewal operation. The IETF has standardized a new DHCPv6 option, called the Information Refresh Time (IRT) option, for the Information-request and Reply exchanges. This option specifies the interval with which the client needs to perform another exchange of Information-request and Reply messages so that the client can update the information with no more delay than the refresh interval.

An implementation that supports this option also has the notion of a default refresh time. Even if the Reply message to Information-request does not include an Information Refresh Time option, the client will perform another exchange about every 24 hours.

Figure 3-3 shows an example of exchanges with the Information Refresh Time option. In the first exchange, the Reply to the Information-request message contains a recursive DNS server address, 2000:db8:1111::35, and an Information Refresh Time option with the interval of 1 hour. Then the site starts renumbering, and the DNS server will have a new address, 2000:db8:ffff::35. During the migration period, both the old and new addresses are valid. In about 1 hour, the client starts the second exchange. This time, the two addresses of the recursive DNS server are provided. Eventually, the Reply message will contain the new address only, and then the site can stop using the old address(es).

d. Exchanges with Relay Agents

If there is no server on a link to which a client is attached, the client needs to contact servers via a DHCPv6 relay agent. The basic notion of relay agents is the same as that of relay agents in DHCPv4, but unlike DHCPv4, separate types of messages are used for communication between servers and relay agents. This is described in the table in section 3.Figure 3-4 shows procedure for a Solicit-Advertise exchange.

e. Other message exchanges

There are some else message exchange process, such as Renewal of Addresses, Server-initiated Exchanges and Other Exchanges for Address Allocation. Because these process are not the focus of this paper, so these are no longer described in detail.

4. We are faced with security issues in the use of DHCPv6

4.1 Stateless address allocation brings security risks

It is convenient and low cost when using Stateless address configuration, but any nodes can be free to access the network, and easily obtain the relevant configuration information, which will bring about security threats.

4.2 Fake DHCP server sends configuration information

In case there is a fake DHCP server in the network, sending incorrect configuration information to the computer to obtain configuration information, which will cause confusion in the network.

4.3 Explicitly send a message, may be illegal to obtain

Message exchanges without encryption, may be accessed by an attacker, which will lead to the leakage of sensitive information.

4.4 Illegal client access to configuration information

Message exchanges without authentication, the configuration information may be accessed by illegal clients.

5. Strategies to improve security

5.1 Strategies to protect the safety of the network

Compared with IPv4, IPv6 has a lot of great improvements. Most notably, IPsec will be integrated into the IPv6 protocol, then IPSec will no longer stand alone, but as an inherent part of IPv6 protocol, and cross-cutting.

For the physical layer of security risks, we can configure redundant equipment, redundant lines, security power supply, environment protection, as well as electromagnetic compatibility to enhance the protection of safety management. Level above the physical layer of security risks, we can use the following means of protection: such as AAA, TACACS +, RADIUS access control protocol, and security control user access to the network to prevent attacks against the application layer; through the MAC address and IP address binding to restrict the MAC addresses per port to use and the number of broadcast packets per port to establish the threshold volume, the use of Port-based VLAN and ACL, users establish a secure tunnel such as to prevent attacks against the two networks; routing through the filter of the routing information encryption and authentication, multicast directional control and improve routing convergence speed and reduce the impact of routing oscillation measures to strengthen the security of three-tier network. IPSec routers and switches guarantee the perfect support for the network data and the validity of information, consistency and integrity, and provide a number of network security solutions.

5.2 Initiative Detect illegal DHCP server

If there is an illegal server on the network, that will be a great danger and can lead to paralysis of the entire network. It is difficult to think the culprit is an illegal server. Even if there existence of an illegal server on the network, but it is also difficult to identify the location of illegal server if in a large enterprise network. So, we can use some methods to detect illegal servers, for example, the establishment of a computer program to achieve this objective.

5.3 Exchanges with Authentication can improve security between DHCP Client and DHCP Server

DHCPv6 has a built-in security mechanism between a client and a server in its base protocol specification. This security mechanism primarily aims to ensure integrity of DHCPv6 messages (particularly ones from a server to a client). It does not provide any confidentiality for message contents.

Overall, the integrity in the DHCPv6 security mechanism is ensured based on the HMAC (Keyed Hashing for Message Authentication Code) protocol. [RFC3315] defines two variations of the mechanism: The delayed authentication protocol and the reconfigure key protocol. Both protocols use a special-purpose DHCPv6 option—the Authentication option—as a common framework.

In the delayed authentication protocol, it is assumed that the client and the server(s) share the key beforehand by some out-of-band method. Figure 4-1 shows message exchanges using the delayed authentication protocol.

In the reconfigure key protocol is used specifically to secure a Reconfigure message. The client and the server do not have to share a key beforehand. Figure 4-2 shows message exchanges including a Reconfigure message with the reconfigure key protocol. Note that the key is sent to the client in the first Reply message without being encrypted. Thus, if an attacker can snoop between the server and the client, it can steal the key and mount an attack using a Reconfigure message with the valid HMAC digest. The reconfigure key protocol is thus not entirely secure, and that is why [RFC3315] states that this protocol be used only when there is not another mechanism available.

5.4 Authenticating communication between DHCP relay agent and server or between DHCP relay agents

In practice, we can use IPsec to achieve the exchange of information security.IPsec was designed such that it is independent of the IP protocol versions. Currently, IPsec is widely deployed in IPv4 as a method to connect multiple remote sites for creating a single Virtual Private Network (VPN) over the Internet. In IPv6, supporting IPsec-related protocols is a mandatory requirement for any IPv6 node, which means all IPv6 nodes have IPsec enabled by default. This requirement will accelerate the deployment of IPsec not only for creating VPNs but also to encourage secure communications among IPv6 nodes. IPsec is a set of mechanisms that adds authentication and encryption to the IP layer.

Figure4-3 shows an example of use IP security for communication between a relay agent and a server or between relay agents.

AH offers connectionless data integrity and data origin authentication for IP packets with optional protection against packet replays. The authentication covers the IPv6 header, the extension headers and upper layer protocol data. Figure 4-4 shows Original Packet of IPv6, Figure 4-5 shows after applying AH.

ESP provides all of the security services offered by AH. In addition, ESP offers data confidentiality by means of encryption and limited traffic flow confidentiality. The header coverage is the primary difference between the authentication service provided by AH and that provided by ESP. ESP does not cover the IPv6 header and the extension headers unless these are encapsulated in the tunnel. Figure 4-6 shows Insertion of the ESP header.

The Authentication Data portion of the ESP packet is optional and is included when the SA has selected the authentication service. The length of the Authentication Data depends on the chosen authentication function. The authentication algorithm performs the computation covering the entire ESP header as shown in Figure 4-6. Since data integrity protection is provided only for the ESP header, we must use AH in addition to ESP if the IPv6 header and the extension headers placed before ESP also require integrity protection. Figure 4-7 shows details of ESP Placement with AH.

6. Conclusion

In the above paragraphs, we have discussed the definition of DHCPv6, and its principle and process for the information exchange. And some feasible strategies to ensure the next generation Ipv6 network DHCP services in security applications have also been given, which is based on the experiences of current Ipv4 network.

References

Chen, lijun. (2008). Security Project Analysis and Investigation Based on DHCP. *Beijing University of Posts and Telecommunications*. 2008. 9. 17.

M. Bellar. R. Canetti. (1997). HMAC: Keyed-Hashing for Message Authentication .*RFC2104*. February 1997.

Qing Li, Tatuya Jinmei and Keiichi Shima. (2007). *IPv6 Advanced Protocols Implementation*. Morgan Kaufmann Publish. 2007.

R. Dorms et al. (2003). "Dynamic Host Configuration Protocol for IPv6 (DHCPv6)," *RFC3315*. July 2003.

R.Droms, W. Arbaugh. (2001). Authentication for DHCP Messages .*RFC3118*. June 2001.

S. Frankel and S. Kelly. (2002). *"The HMAC-SHA-256-128 Algorithm and Its Use with IPsec"*. Internet Draft:

draft-ietf-ipsec-ciph-sha-256-01.txt. June 2002.

T. Narten and R. Draves. (2001). "Privacy Extensions for Stateless Address Autoconfiguration in IPv6".*RFC3041*. January 2001.

Xiao, shaobin. (2005). Research and Implementation for DHCPv6.*Southwest Jiaotong University*.2005.8.16.

Table 1. Message Name and Descriptions

Type	Name	Description
1	Solicit	Sent by a client to find available DHCPv6 servers
2	Advertise	Sent by a server in response to a Solicit message with configuration information.
3	Request	Sent by a client to a particular server to perform resource (e.g., address) allocation.
4	Confirm	Sent by a client when it may have moved to a different link in order to check whether the prefix of allocated addresses (if any) is still valid.
5	Renew	Sent by a client to the server that has allocated a configuration resource to renew the use of that resource.
6	Rebind	Sent by a client to servers to renew an allocated information resource when the attempt using Renew messages fails.
7	Reply	Sent by a server in response to various messages from a client, mainly for confirming or rejecting the request that the client made.
8	Release	Sent by a client to the server that allocated a configuration resource in order to inform the server that the resource can be released.
9	Decline	Sent by a client when it detects that an allocated address is already in use. It informs the server that the address cannot be used.
10	Reconfigure	Sent by a server to initiate exchanges starting with a Renew or Information request message. It forces the client to refresh the information allocated to it.
11	Information-req uest	Sent by a client for the stateless service.
12	Relay-forward	Sent by a relay agent, encapsulating a message from a client to the server.
13	Relay-reply	Sent by a server, encapsulating a message returned to a client through relay agents.
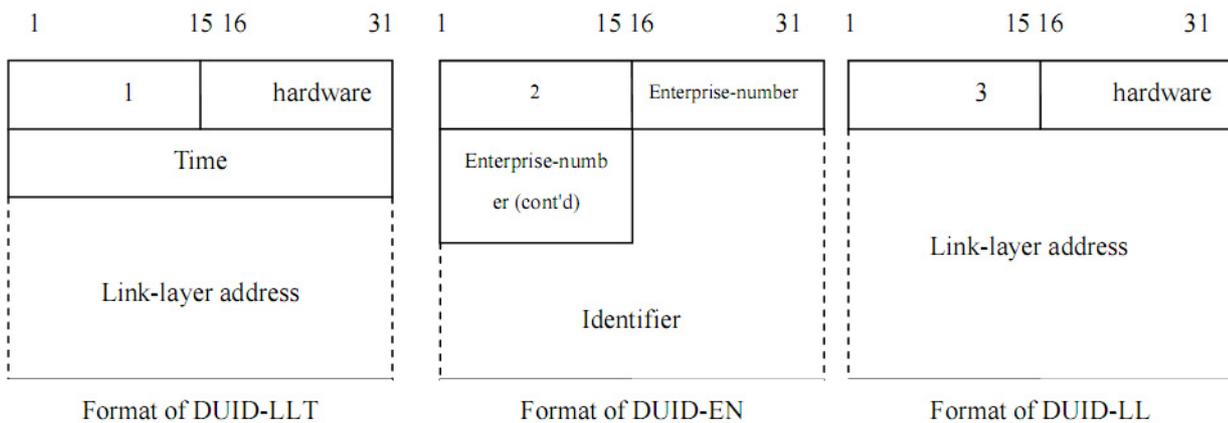
Figure 2.1 Three types of DUIDs

Time (sec)→
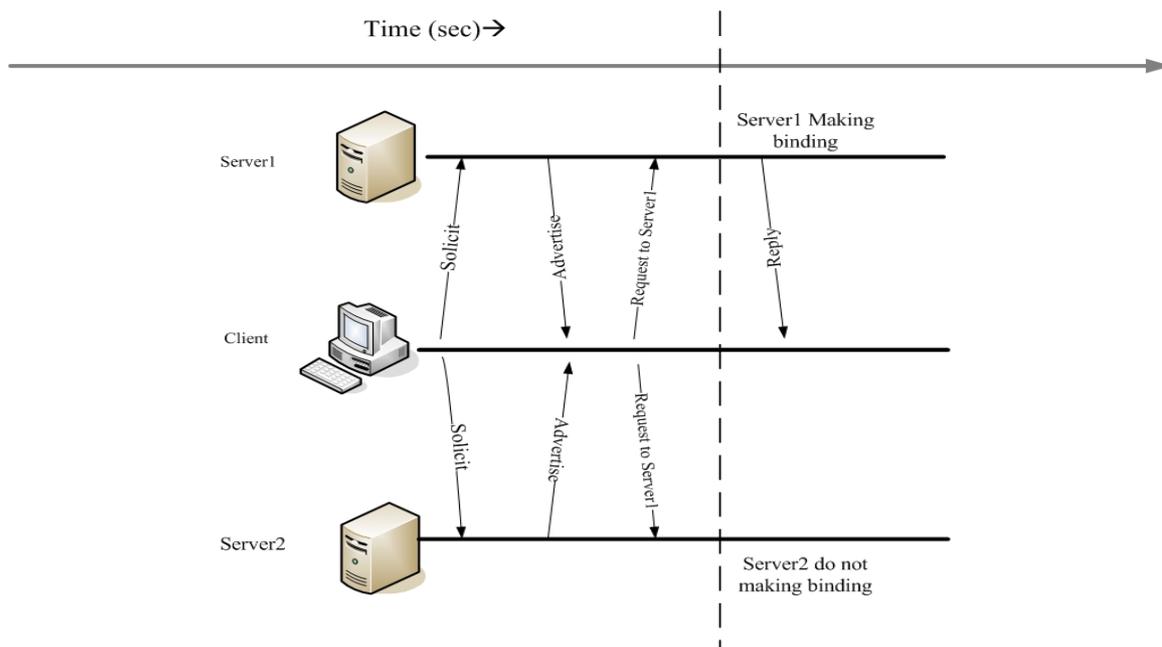
Figure 3-1. Initial message exchanges for address allocation

←   -----migration period-----   →

Time   ←   1 hour   → ←   1 hour   →

*1:
DNS server
address =2000:db8:1111::35
IRT=1 hour

*2:
DNS server
address =2000:db8:1111::35
           2000:db8:ffff::35
IRT=1 hour

*3:
DNS server
address =2000:db8:ffff::35
IRT=1 hour
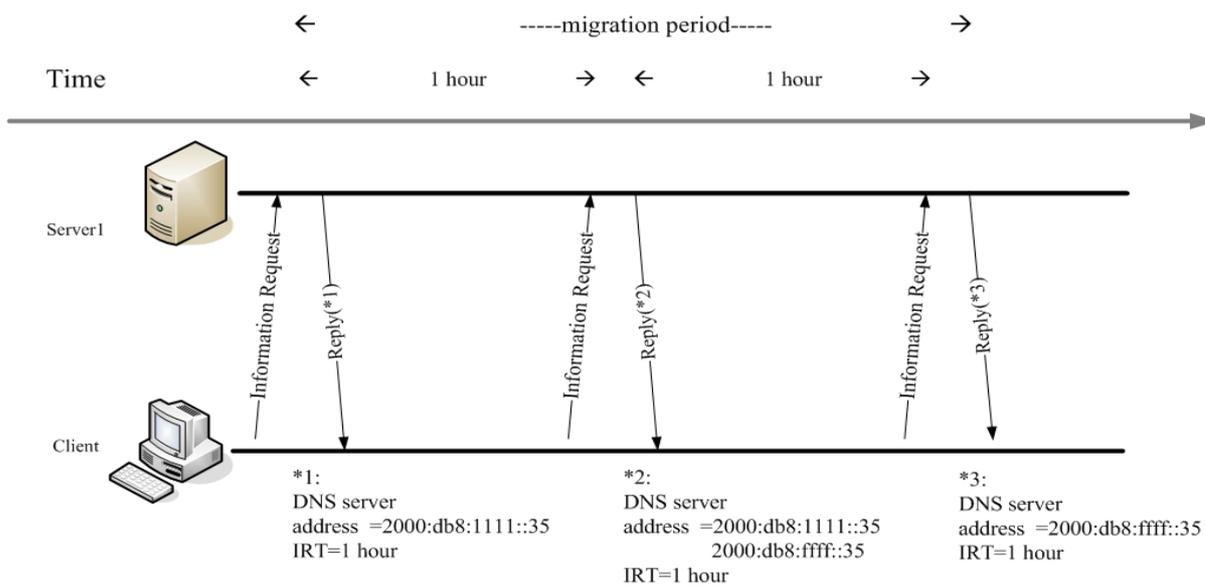
Figure 3-3. Renumbering procedure for stateless exchanges
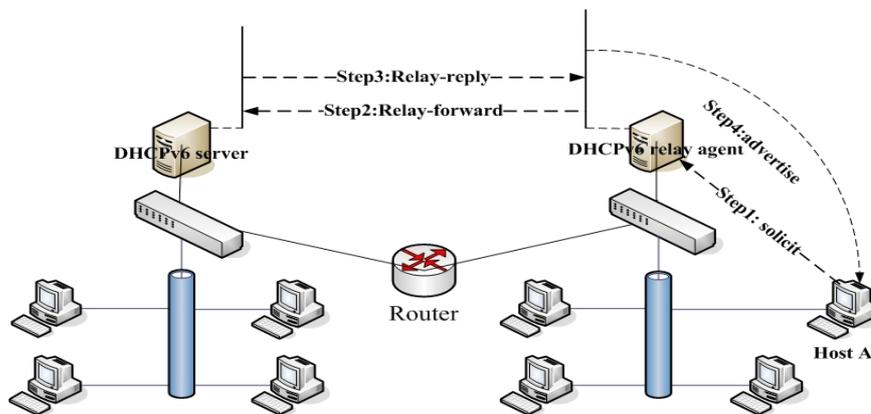
Figure 3-4. Solicit-Advertise exchange via a relay agent
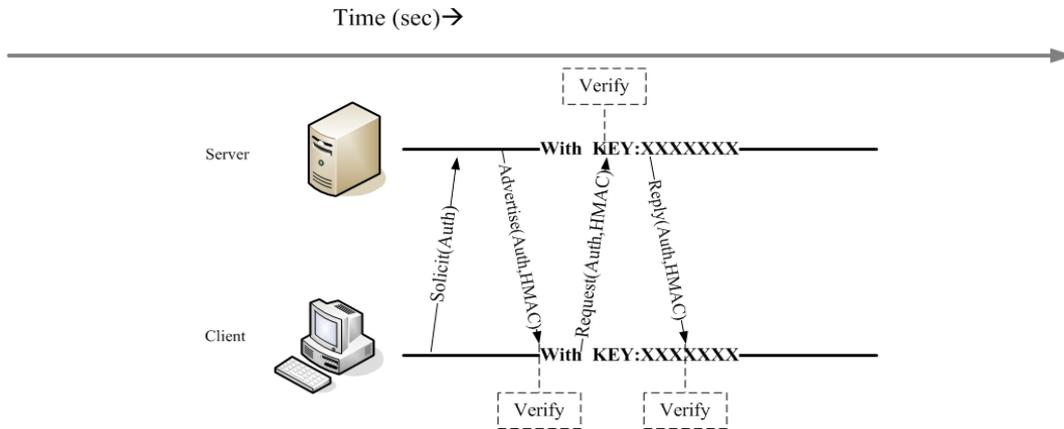
Figure 4-1. DHCPv6 message exchanges using the delayed authentication protocol
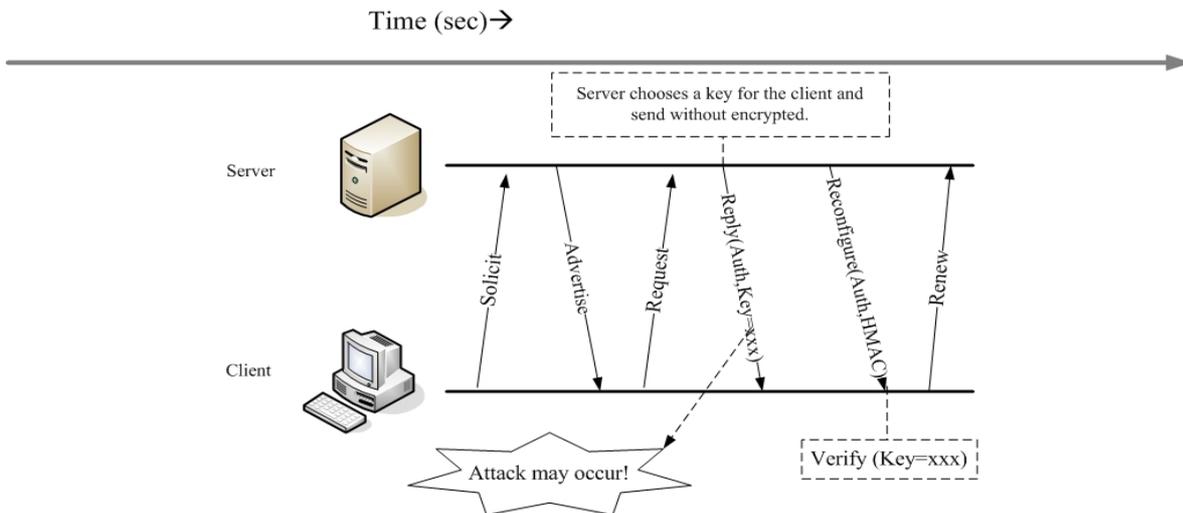
Figure 4-2. DHCPv6 message exchanges using the reconfigure key protocol.
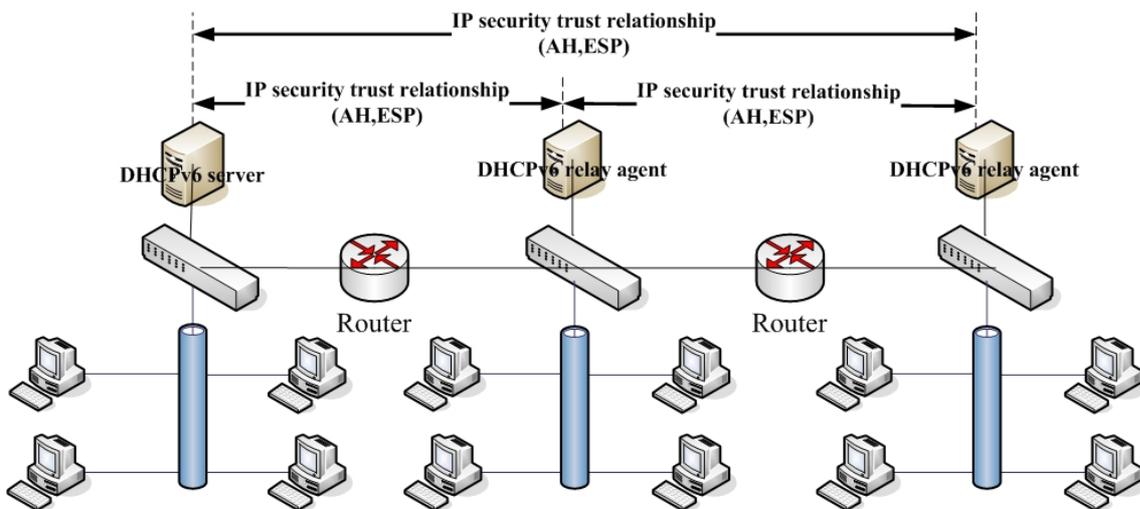
Figure 4-3. Use IP security for communication between a relay agent and a server or between relay agents.

Original IP Header	Extension Headers if present	Upper Layer Header	Data
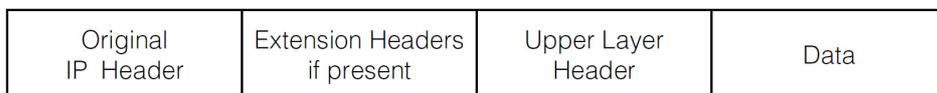
Figure 4-4. Original Packet of IPv6

Original IP Header	Extension Headers before AH	AH	Extension Headers after AH	Upper Layer Header	Data

Figure 4-5. After applying AH

IPv6 Header	Hop-by-Hop, Dest 1, Routing, Fragmentation	ESP	Dest 2	Upper Layer	Data	ESP Trailer	ESP Auth

Figure 4-6. Insertion of the ESP header

IPv6 Header	Hop-by-Hop, Dest 1, Routing, Fragmentation	AH	ESP	Dest 2	Upper Layer	Data	ESP Trailer	ESP Auth

|← encrypted →|

|← authenticated →|

|← authentication computation covering all except mutable fields →|
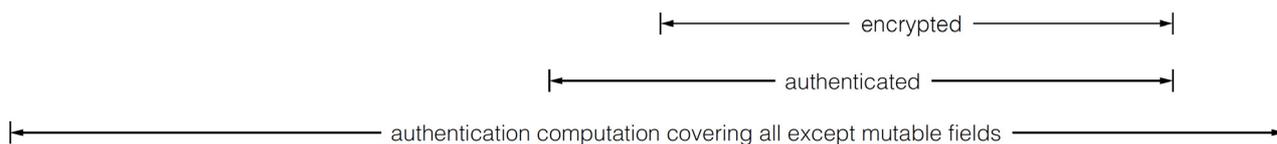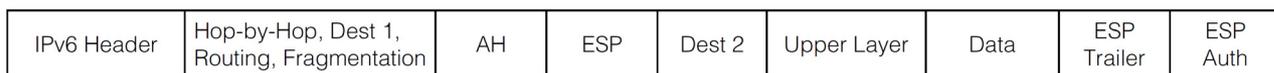
Figure 4-7. ESP Placement with AH

Study on Fouling and Cleaning of PVDF Membrane

Bofeng Zhang & Shihu Ma (Corresponding author)

Key Laboratory of Hollow Fiber Membrane Material & Membrane Process, Ministry of Education

Tianjin Polytechnic University, Tianjin 300160, China

Tel: 86-22-2458-5031   E-mail: zhangbofeng08@163.com

Abstract

The effects of different water sources on the fouling of PVDF membrane are different. On the basis of the scientific appraisal, the correct cleaning process and cleaning reagent are selected to recover the flux and other performances of PVDF membrane. The results indicate that the TMP (transmembrane pressure) of PVDF membrane can be effectively recovered by CIP (clean-in-place) process, and almost reaches the initial level even under the circumstance that PVDF membrane has been used for a certain time and its TMP can not be recovered by either physical cleaning process or CEB (chemically enhanced backwashes).

Keywords: PVDF membrane, Membrane fouling, Membrane cleaning, Cleaning agent

Preface

PVDF membrane is easy to clean, and has advantages of high flux, fouling resistance, anti-corrosion, long service life and etc. It is widely applied in the municipal facilities, chemical industry, petrochemical industry, electric power industry, seawater desalination, gray water reuse, pharmaceutical industry, food industry and etc. The key issue of PVDF membrane in practical applications is the membrane fouling. The membrane fouling causes the declines of the membrane flux, filterability and etc., in turn restricts and challenges the vigorous development of PVDF membrane separation technology. An effective way of solving the issue of membrane fouling is to clean the membrane, and recover its flux, filterability and etc., in turn prolong its service life. Therefore, a rational and effective way of cleaning the fouled membrane is of the great significance.

1. PVDF membrane fouling

PVDF membrane fouling is defined as the process in which microparticles, colloidal particles, solute molecules or bacteria deposit onto the PVDF membrane surface or into the membrane pores such that the membrane pores are blocked or become smaller, and membrane resistance increases, in turn its performances (membrane flux and etc.) are deteriorated. The generalized membrane fouling can be divided into reversible fouling and irreversible fouling based on the attachment strength of particles to the membrane surface. Reversible fouling, caused by a gel layer resulted from reversible concentration polarization, can be removed by means of strong shear force of backwashing. The foulants causing reversible fouling include inorganic compounds (silicon, alumina, iron, calcium, manganese and etc.), organic compounds, as well as microorganisms, bacteria and their metabolites (Lin et al, 2009, p. 94-96, 99). Irreversible fouling, caused by irreversible absorption and blockage, is impossible to be removed by physical cleaning method. Ridgway et al (1988, p. 429-481) reported that the membrane fouling had three features in common: (1) Gradual decline of membrane flux; (2) Gradual decline of intercepting rate of minerals; (3) Gradual increase of TMP and pressure difference across the membrane.

2. Foulants on PVDF membrane

Water supply is divided into groundwater and surface water on the basis of the types of water source (Yan et al, 1999, p. 233-236). The foulants from groundwater mainly contain colloids and scaling ions. Colloids are mainly clays. Scaling ions consist of positive ions and negative ions, wherein positive ions mainly include Ca^{2+}, Mg^{2+}, Na^+, as well as a small amount of K^+, Fe^{2+}, Mn^{2+}, Cu^{2+} and etc.; and negative ions mainly include HCO_3^-, SO_4^{2-}, Cl^-, as well as a small amount of $HSiO_3^-$, CO_3^{2-}, NO_3^- and etc. The foulants from surface water mainly contain algae; suspensions and colloids such as bacteria, virus, humus, protein, microorganisms; water-soluble substances such as metal salt of Fe, Mn, Si, Ba and etc.

Wastewater is divided into domestic wastewater and industrial wastewater (Zhang et al, 2000, p. 1). Domestic wastewater, with a high value of COD_{Cr}, contains large amount of carbohydrate and nutrient elements in terms of N, P, S and etc, as well as detergent, various bacteria and microorganisms. Industrial wastewater, with a high acidity or alkalinity, contains large amount of suspensions and harmful substances such as pesticide, phenol, dye, polycyclic aromatic hydrocarbon, oil (Liu et al, 2005, p.156-208).

A wide range of processed water with various water qualities results in different foulants on PVDF membrane. Table 1 shows the foulants on PVDF membrane from different water sources.

There are very big differences among various industrial wastewaters. Table 2 shows the foulants on PVDF membrane from various industrial wastewaters (Yan et al, 1999, p. 233-236).

3. PVDF membrane cleaning

Although the gradual decline of membrane flux is an inevitable phenomenon during membrane filtration, PVDF membrane can be recovered by proper cleaning. Correct cleaning process and cleaning reagent should be selected on the basis of the investigation and analysis on the foulants. Table 3 shows the identification methods of various foulants.

Membrane can be cleaned either physically, biologically or chemically. Physical cleaning is effective on removing the cake layer on the PVDF membrane; chemical cleaning is effective on removing the minerals, inorganic substances, organic substances and microorganisms; whereas biological cleaning is effective on removing the foulants on and inside the membrane with biocides such as microorganisms and enzymes (Zhang et al, 2003, p. 187).

3.1 Physical cleaning

Physical cleaning uses water jet or water-air jet to wash the membrane surface. This process will not introduce new foulants and is easy to operate (Zhang et al, 2003, p. 187). It includes various processes in terms of low pressure-high flow rate cleaning, isostatic pressure cleaning, backflushing (Wang et al, 2005, p. 61-63), negative pressure cleaning (Wu et al, 1999, p. 52-55), mechanical scrub (Liu et al, 2003, p. 65-68), ultra-sonic cleaning (Kobayashi T et al, 2000, p. 2980-2981), electrophoretic cleaning, hot water cleaning, circulation spray cleaning and etc.

A detailed introduction of physical cleaning is as follows:

(1) Forward flushing: the flushing water flows in the direction of influent water. Use the flushing water to wash through the particle deposits from raw water side to product water side. Either recycling mode or continuous mode can be used. The cleaning interval depends on the situation, but generally is 10~30 min.

(2) Backward flushing: the flushing water flows in the reverse direction of influent water. Use the flushing water to wash through the particle deposits from product water side to raw water side. Recycling mode can not be applied lest the product water is polluted by the flushing water. The cleaning interval depends on the situation, but generally is 10~20 min.

(3) Air-water flushing: a measured volume of compressed air is introduced to the in-flow side during backward flushing. The upwardly rising air bubbles provide intensive frictions to remove the foulants which are flushed out through outlet.

3.2 Chemical cleaning

In practical operation, physical cleaning doesn't work when PVDF membrane is severely fouled. It is necessary to use chemical reagents. There are two types of processes for chemical cleaning: on-line cleaning and off-line cleaning.

(1) On-line cleaning: the in-service PVDF membrane is directly cleaned with chemical reagents.

(2) Off-line cleaning: PVDF membrane must be removed from service for a period of time, so that the membrane can be opened for chemical cleaning. This process can rapidly recover the flux of PVDF membrane.

Whichever process is used, it is important to correctly select the chemical reagent, reagent concentration, operating sequence and cleaning interval in view of the chemicals resistance of membrane, type of foulant and fouling degree. The commonly used chemical reagents include acid detergent (hydrochloric acid, for example), alkaline detergent (sodium hydroxide, for example), oxidant (sodium hypochlorite, for example), enzyme detergent, surfactant, chelating agent, disinfectant, complex agent and etc. Various foulants are removed with different detergents. Alkali, oxidant and alkaline detergent are used to remove organic foulants, whereas inorganic acid, organic acid and acid detergent are used to remove inorganic foulants (Lin et al, 2009, p. 94-96, 99). Table 4 shows the types of foulants and corresponding cleaning reagents.

4. Cleaning experiment of PVDF membrane

4.1 Studied water sample

The study is completed at Tianjin TEDA New Water Sources Technology Development Co., Ltd. The water sample is from the municipal wastewater which flows from SBR, through regulation pond, and into primary water container; then is processed with PVDF membrane of 8 inches. The technological process is expressed with the following flowsheet.

Raw water → grid → SBR → horizontal settling pond → regulation pond → security filter → primary water tank → PVDF membrane assembly of 8 inches → fresh water tank → water output

Table 5 and table 6 respectively reveal the qualities of outlet water from SBR and regulation pond.

4.2 Used equipment

The equipment is a PVDF membrane assembly of 8 inches from Tianjin MOTIMO Membrane Technology Co., Ltd. This membrane assembly has advantages of large loading capacity, high water output per membrane and etc. The material used to make the equipment is PVDF fiber developed by Tianjin MOTIMO Membrane Technology Co., Ltd. This PVDF fiber has a molecular weight cutoff of 0.03 μm and pore size of 0.2 μm. The technological process of the above-mentioned membrane assembly is expressed with the following flowsheet.

(1) Process of water production: forward flushing → water output → air-water flushing → backward flushing → forward flushing

(2) CEB process: chemically enhanced air-water flushing → chemically enhanced backward flushing → introduction of acid / reagent / acid + reagent → immersing → chemically enhanced air-water flushing →chemically enhanced backward flushing → forward flushing → water output

(3) CIP process: CIP air-water flushing → CIP backward flushing → introduction of cleaning chemicals (one chemicals or combination of several chemicals) → circulating → immersing → CIP air-water flushing → CIP backward flushing → forward flushing until pH is 7 → water output

4.3 Result and analysis

The changes of TMP of the membrane assembly before and after CEB process had been continuously investigated for four months. Figure 1 exhibits the observed results.

From figure 1, we can see that the water output had increased from 3 t/h to 3.7 t/h from early April until mid-July, and TMP of the membrane assembly had changed little (40~60 kPa) in this period. The TMP was over 100 kPa before CEB and declined to the normal level after CEB on 29 March, 17 April and 24 April. It indicated that the membrane fiber was not severely fouled and the TMP was effectively recovered by CEB. However, after 17 July, the TMP before CEB had rapidly increased up to 120 kPa, so had the TMP after CEB. It indicated that the membrane fiber was severely fouled and the TMP can not be effectively recovered only by CEB. Therefore, it is necessary to apply CIP process to improve the cleaning effects of the membrane assembly.

The turbidity, COD_{Cr} and total bacterial count of the feed water and the permeate water are respectively shown in Figure 2~4.

Figure 2 exhibits that the feed water has a high turbidity of 1~3 NTU, however, the permeate water has a very low turbidity and is stable. Figure 3 exhibits that COD_{Cr} of the permeate water is much lower than that of the feed water. Figure 4 exhibits that the total bacterial count of the feed water is high and remarkably different for different dates, whereas that of the permeate water is lower than the detection limit. These results prove that CIP process has an excellent effect on the recovery of the PVDF membrane assembly.

Based on the nature of the feed water (see table 1~2) and the types of the cleaning reagents (see table 4), we selected sodium hypochlorite, sodium hydroxide and hydrochloric acid as chemical cleaning reagents. The specific cleaning procedure is expressed with the following flowsheet.

(1) NaOH of 1,000 ppm + NaClO of 2,000 ppm → circulate for 20 min → immersing for 3 h → circulate for 20 min;

(2) Discharge of cleaning solution → forward flushing → discharge, until pH of discharge liquor is equal to 7;

(3) 8,000 ppm HCl → circulate for 20 min → immersing for 1 h → circulate for 20 min.

The TMP was measured to be approximately 35 kPa when step 2 was finished, and still was 35 kPa when step 3 was finished. It indicated that the membrane assembly had been severely fouled by microorganism and organic substances, instead of inorganic substances.

The water output had been set as 3.7 t/h and CIP process had been applied since 24 July. From figure 1, we can see that the TMP of the membrane assembly had been recovered to 40~60 kPa, and stayed stable. It indicates that the TMP of PVDF membrane can be effectively recovered by CIP process. Exploration of a more scientific and economical CIP process will be critical in the future study.

5. Conclusion

Membrane fouling is an inevitable phenomenon during PVDF membrane filtration. It is always necessary to investigate the nature of the feed water, types of the foulants and degree of the fouling, as well as the membrane properties, cleaning solution properties and cleaning process. A scientific membrane cleaning system should be established to recover the membrane flux rapidly. Correct membrane cleaning is not only a perfect end, but also a brand new start of

the membrane process.

References

Kobayashi T & Fujii N. (2000). Effect of ultrasound on enhanced permeability during membrane water treatment. *Japanese Journal of Applied Physics*, 39(5), 2980-2981.

Lin, Ye, Chen, Jianyong & Zhu, Lieping. (2009). *Membrane Filtration Technology for Water Supply*. Beijing: Chemical Industry Press, p. 94-96, 99.

Liu, Enhua, Huan, Guolan, Du, Qiyun & Men Penghui. (2003). Research on an effective method of washing membrane: the system of washing membrane with sponge balls. *Membrane Science and Technology*, 23(6), 65-68.

Liu, Moe, Cai, Bangxiao & Chen, Yitang. (2005). *Application of Membrane Technology in Wastewater Process and Reuse*. Beijing: Chemical Industry Press, p. 3, 156-208.

Ridgway H F. (1988). Microbial adhesion and biofouling of reverse osmosis membranes. In Parekh, B (Eds), *Reverse Osmosis Technology*. New York: Marcel Dekker, p. 429-481.

Wang, Zhiqiang, Cai, Zhenyu, Zhang, Zhigang, Du, Shaoguang & Li, Juan. (2005). Study on the combination backwashing of gas and permeate as membrane fouling prevention techniques. *Techniques and Equipment for Environmental Pollution Control*, 6(8), 61-63.

Wu, Guangxia, Zhang, Donghua, Liu, Zhongzhou & Zeng, Jin. (1999). Cleaning membrane by negative pressure. *Membrane Science and Technology*, 19(4), 52-55.

Yan, Xushi & Fan, Jinchu. (1999). *Water Supply Engineering*. Beijing: China Architecture & Building Press, p. 125, 233-236.

Zhang, Guojun & Liu, Zhongzhou. (2003). Progress in membrane cleaning techniques. *Technology of Water Treatment*, 29(4), 187-190.

Zhang, Zijie, Lin Rongshen & Jin Rulin. (2000). *Sewage Engineering*. Beijing: China Architecture & Building Press, p.1.

Table 1. The foulants on PVDF membrane from different water sources

Water quality	Foulants
Groundwater	Colloid (clay, SiO_2), scaling ion (Ca^{2+}, Mg^{2+}, Fe^{2+}, Mn^{2+} and etc.)
Surface water	Colloid (humus, protein), suspension (SS), organism (algae, bacteria, virus, microorganism), organic foulant (humus, protein, organic substance)
Domestic wastewater	Organism (bacteria, microorganism), organic foulant (hydrocarbon, nitrogen, phosphorous)
Industrial wastewater	Suspension (SS), organism (algae, bacteria, microorganism), organic foulant, oil

Table 2. The foulants on PVDF membrane from different industrial wastewaters

Types of wastewaters	Foulants
Wastewater from chemical industrial	Suspension (SS), COD_{Cr}, NH_3-N, grease, phenol, salt, catalyst (Fe, CO, Ni, Cr, Mn), and etc.
Wastewater from metallurgical industrial	Suspension (SS), COD_{Cr}, metallic ions in terms of calcium, magnesium, zinc, chromium, lead and etc., rare-earth ions, oil, and tar oil
Wastewater from petroleum and petrochemical industrial	Suspension (SS), COD_{Cr}, oil, phenol, acetone, aromatic hydrocarbon, benzene, sulfide, soluble salt and etc.
Wastewater from textile and dyeing industry	Suspension (SS), COD_{Cr}, BOD_5, detergent, grease, oil, salt and etc.
Wastewater from pharmaceutical industry	Suspension (SS), COD_{Cr}, BOD_5, bacterial, virus, microorganism and etc.
Wastewater from food industry	Suspension (SS), COD_{Cr}, BOD_5, NH_3-N, bacterial, virus, microorganism and etc.
Wastewater from mining industry	Suspension (SS), sulfate, calcium salt, heavy metal ions such as Fe^{3+}, Cu^{2+} and Zn^{2+}, oil and etc.
Wastewater from paper-making industry	Suspension (SS), COD_{Cr} and etc.
Wastewater from electroplating industry	Heavy metal ions such as Cr, Ni, Cd, Cu, Zn, Au and Ag, cyanogens, surfactant, brightener and etc.
Wastewater from pesticide industry	Suspension (SS), COD_{Cr}, phenol, benzene, arsenic, mercury, salt and etc.

Table 3. The identification methods of various foulants.

Foulants	Identification methods
Microorganism, bacterial, algae	Observe by microscope
Inorganic scaling deposit (oxide, hydroxide, insoluble salt, complex compound)	Chemical analysis, inductively coupled plasma spectroscopy (ICP), atomic absorption spectrometry (AAS)
Acid-insoluble oxide	Chemical analysis, inductively coupled plasma spectroscopy (ICP), atomic absorption spectrometry (AAS)
Hydrophobic substance	Gas chromatograph (GC), Fourier transform infrared spectroscopy (RTIR)
Insoluble ion (Fe^{2+}, Ca^{2+}, Mg^{2+}, Ba^{2+} and etc.)	Chemical analysis, inductively coupled plasma spectroscopy (ICP), atomic absorption spectrometry (AAS)
Colloid	Fourier transform infrared spectroscopy (RTIR), scanning electron microscope (SEM)
Protein	Fourier transform infrared spectroscopy (RTIR), scanning electron microscope (SEM)
Organic substance, oxide and etc.	Chemical analysis, inductively coupled plasma spectroscopy (ICP), atomic absorption spectrometry (AAS)
oil	Chemical analysis

Table 4. The types of foulants and corresponding cleaning reagents.

Foulants	Cleaning reagents and their concentrations	Others
Microorganism, bacterial, algae	NaClO of 500~5,000 ppm, less than 10,000 ppm for short-term use	1.5% H_2O_2
Inorganic scaling deposit (oxide, hydroxide, insoluble salt, complex compound)	HCl with concentration less than 10% HNO_3 with concentration less than 10% Oxalic acid with concentration less than 4% Citric acid with concentration less than 10%	Citric acid with concentration of 2%, pH=7 (NH_3), Tartaric acid
Acid-insoluble oxide	Oxalic acid	Reductants
Hydrophobic substance	Specific reagent	Functional reagent + additives
Insoluble ion (Fe^{2+}, Ca^{2+}, Mg^{2+}, Ba^{2+} and etc.)	1%~2% EDTA (Na_2)	Other chelating agents
Colloid	10%~20%NaCl	Other denaturant
Protein	Enzyme preparation	Denaturant
Organic substance, oxide and etc.	NaOH with concentration less than 4%	
oil	0.02%~1% sodium dodecylbenzenesulfonate	Other surfactants

Table 5. The quality of outlet water from SBR.

pH	COD (mg/L)	Ammonia-nitrogen (mg/L)	Turbidity	Conductivity (μS/cm)
6.85~7.7	20.79~29.76	9.52~21.01	1.4~3.27	4,200~5,600

Table 6. The quality of outlet water from regulation pond.

| pH	COD (mg/L)	Ammonia-nitrogen (mg/L)	Turbidity	Conductivity (μS/cm)
6.9~7.8	22.1~30.6	10.27~22.92	1.07~4.68	3,600~4,780
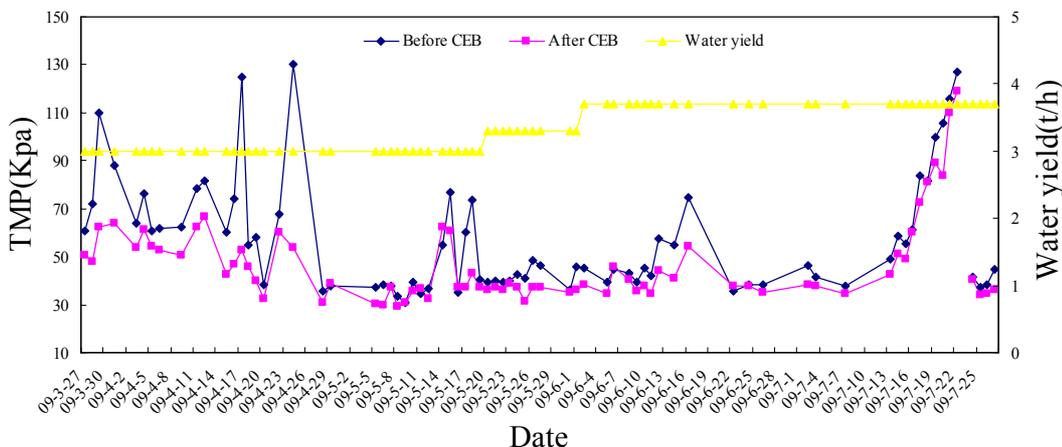
Figure 1. The changes of TMP of the membrane assembly before and after CEB process
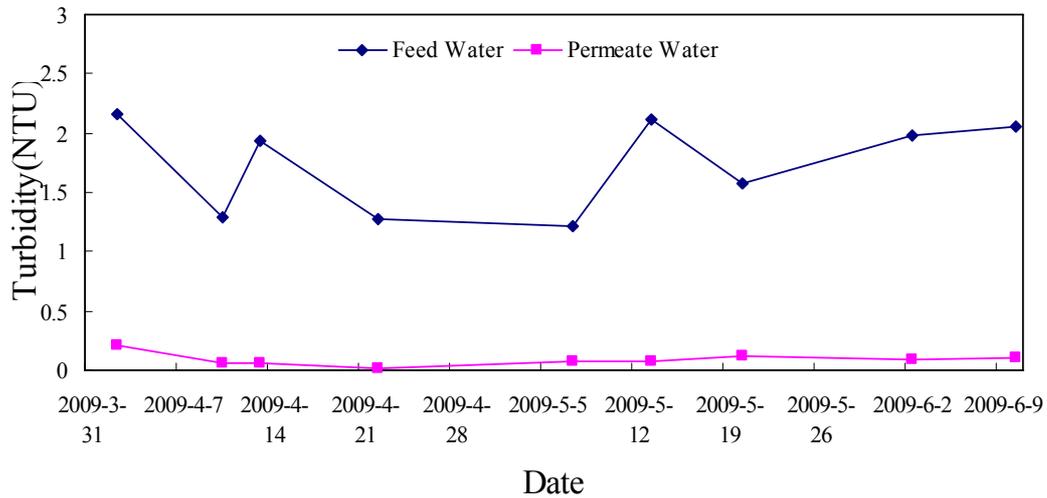
Figure 2. The turbidity of the feed water and the permeate water
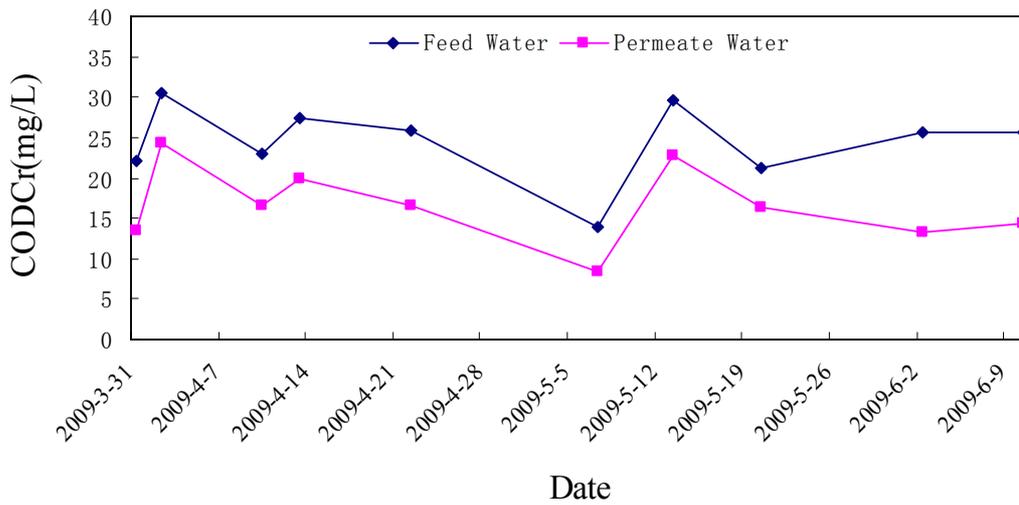
Figure 3. COD$_{Cr}$ of the feed water and the permeate water
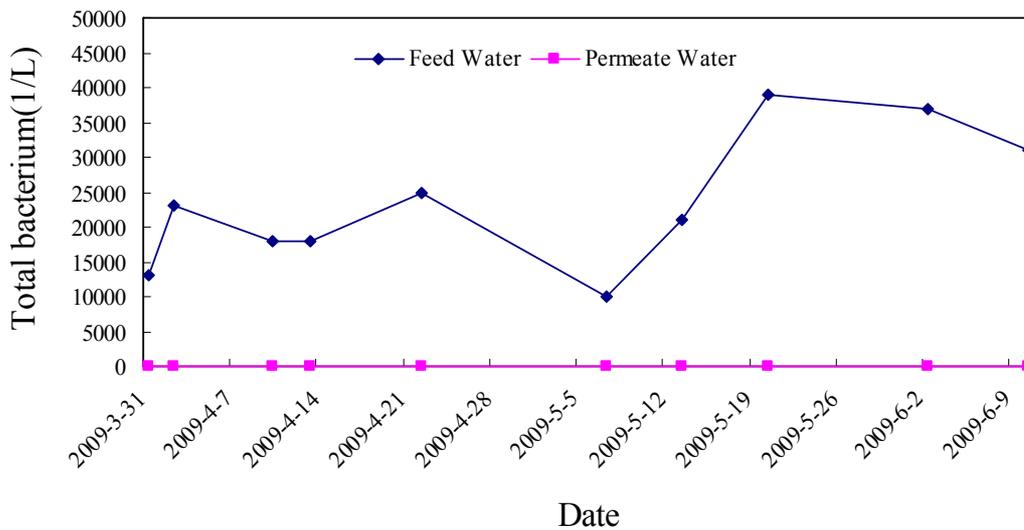
Figure 4. The total bacterial count of the feed water and the permeate water

A Non-parametric Regression Model for Consumption of Urban Residents and Foreign Exchange Reserve

Yi Ning & Xiangdong Song

Department of Probability Theory and Mathematical Statistics, Yanshan University

Qinhuangdao 066004, China

E-mail: iamddt123@126.com

Abstract

The consumption of urban residents and the foreign exchange reserves are important indicators of economic development and between which there existed a stable relationship. Local polynomial regression estimation method of the non-parametric regression model is discussed and considering the historical data of China's consumption of urban residents and foreign exchange reserves from 1981 to 2003, which was researched using the local polynomial regression estimation method of the non-parametric regression model, we built its non-parametric regression model and compare it with the polynomial fitting model. The results showed that non-parametric regression model is superior to polynomial fitting model.

Keywords: Non-parametric regression, Local polynomial regression estimation, Polynomial fitting

The consumption of urban residents is a significant economic indicator, which reflects the economic situation of one country. With the development of China's economic reform, and the rising level of people's income and consumption at the same time, foreign trade status is having a profound impact on China's economic growth and people's lives(Xiaodong, Shen and Weiya, Zhao,2005,1,18-22). Currently, as foreign trade continuously extends and domestic demand grows, the research of urban residents' consumption demand and patterns can be helpful to explain the trend of changes in consumer demand and the law of the consumer goods market, which can be useful to predict future demand for various types of consumer goods and help the relevant government departments to adjustment product structure and make reasonable arrangements for foreign trade and circulation which is of great significance for the healthy development of economy (Huiming, Zhu and Yuqi, Han,2002,18(5):7-10)(YE,A-zhong,2002,21(1):47). The foreign exchange reserve is also a significant economic indicator which has a stable relationship with the consumption level of urban residents under the condition of macroeconomic in China. This paper investigates the local polynomial regression estimation method of the non-parametric regression model which is used to empirically research the relationship between China's consumption of urban residents and foreign exchange reserve.

1. Nonparametric regression model and local polynomial regression estimation

1.1 nonparametric regression model

Definition 1.1: With given n pairs of observed value (x_1, Y_1), …, (x_n, Y_n), the relationship between response variable Y and covariate variables x is defined by following equation:

$$Y_i = r(x_i) + \varepsilon_i, \, \mathrm{E}(\varepsilon_i) = 0, i = 1, 2, \cdots, n, \tag{1.1}$$

where r is regression function. Variable x is also known as characteristic. The estimation of $r(x)$ is represented by $\hat{r}_n(x)$.

1.2 Local polynomial estimation

Under the Nadaraya-Watson kernel estimation condition, consider an estimator $a \equiv \hat{r}_n(x)$ to minimize $\sum_{i=1}^{n}(Y_i - a)^2$.

Define weight function $w_i(x) = K((x_i - x)/h)$, and chose $a \equiv \hat{r}_n(x)$ to minimize the following weighted quadratic sum

$$\sum_{i=1}^{n} w_i(x)(Y_i - a)^2 \tag{1.2}$$

Solution obtained is

$$\hat{r}_n(x) \equiv \frac{\sum_{i=1}^{n} w_i(x) Y_i}{\sum_{i=1}^{n} w_i(x)} , \tag{1.3}$$

which is kernel regression estimation.

To improve the estimation, a *p*-order local polynomial is used. x is a fixed value which is used to estimate $r(x)$. For value u that belongs to the neighborhood of x, define polynomial

$$P_x(u;a) = a_0 + a_1(u-x) + \frac{a_2}{2!}(u-x)^2 + \cdots + \frac{a_p}{p!}(u-x)^p , \tag{1.4}$$

which approximates a smooth regression function $r(u)$ in the neighborhood of target value x with the following polynomial:

$$r(u) \approx P_x(u;a) . \tag{1.5}$$

To estimate $\mathbf{a} = (a_0, \cdots, a_p)^{\mathrm{T}}$, chose $\hat{\mathbf{a}} = (\hat{a}_0, \cdots, \hat{a}_p)^{\mathrm{T}}$ which minimizes the following weighted quadratic sum:

$$\sum_{i=1}^{n} w_i(x)[Y_i - P_x(X_i;a)]^2 . \tag{1.6}$$

Estimater $\hat{\mathbf{a}}$ depends on target value x. While $\hat{\mathbf{a}}(x) = (\hat{a}_0(x), \cdots, \hat{a}_p(x))^{\mathrm{T}}$, the local estimation of r is $\hat{r}_n(u) = P_x(u;\hat{a})$.

While

$$\mathbf{X_x} = \begin{bmatrix} 1 & x_1 - x & \cdots & \dfrac{(x_1 - x)^p}{p!} \\ 1 & x_2 - x & \cdots & \dfrac{(x_2 - x)^p}{p!} \\ \vdots & \vdots & & \vdots \\ 1 & x_n - x & \cdots & \dfrac{(x_n - x)^p}{p!} \end{bmatrix} , \tag{1.7}$$

And $\mathbf{W_x}$ is a $n \times n$ diagonal matrix, where $w_{ij} = w_i(x)$. (1.6) could be written as

$$(\mathbf{Y} - \mathbf{X_x a})^{\mathrm{T}} \mathbf{W_x} (\mathbf{Y} - \mathbf{X_x a}) . \tag{1.8}$$

By minimizing (1.8), a weighted least square estimation is obtained

$$\hat{\mathbf{a}}(x) = (\mathbf{X_x^T W_x X_x})^{-1} \mathbf{X_x^T W_x Y} . \tag{1.9}$$

As $\hat{r}_n(x) = \hat{a}_0(x)$ is the inner product of the first line from $(\mathbf{X_x^T W_x X_x})^{-1} \mathbf{X_x^T W_x}$ and $\mathbf{Y}$, then there is:

Theorem 1.1: estimation for the local polynomial regression is:

$$\hat{r}_n(x) = \sum_{i=1}^{n} l_i(x) Y_i , \tag{1.10}$$

where

$$\mathbf{L}(x)^{\mathrm{T}} = (l_1(x), \cdots, l_n(x)) , \tag{1.11}$$

$$\mathbf{L}(x) = \mathbf{e_1^T}(\mathbf{X_x^T W_x X_x})^{-1} \mathbf{X_x^T W_x} , \tag{1.12}$$

$\mathbf{e_1} = (1, 0, \cdots, 0)^{\mathrm{T}}$, and $\mathbf{X_x}$ and $\mathbf{W_x}$ were defined in (1.7).

The mean value and covariance value of this estimation are:

$$\mathrm{E}(\hat{r}_n(x)) = \sum_{i=1}^{n} l_i(x) r(x_i) , \tag{1.13}$$

$$\text{Var}(\hat{r}_n(x)) = \sigma^2 \sum_{i=1}^{n} l_i(x)^2 = \sigma^2 \left\| \mathbf{L}(x) \right\|^2 . \tag{1.14}$$

Theorem 1.2: If $\hat{r}_n$ is a linear smoothing value, then the leave-one-out cross-validation score $\hat{R}(h)$ can be written as

$$\hat{R}(h) = \frac{1}{n} \sum_{i=1}^{n} \left[\frac{Y_i - \hat{r}_n(x_i)}{1 - L_{ii}} \right] , \tag{1.15}$$

in which, $L_{ii} = l_i(x_i)$ is the ith diagonal elements of the smooth matrix.

The bandwidth h can be obtained by minimizing cross-validation formulas from theorem 1.2(Larry Wasserman,2008,p.57-62).

2. A non-parametric regression model of the consumption of urban residents and the foreign exchange reserve

Define **Y** as foreign exchange reserves, **X** as consumption of urban residents. The research sample is the historical data of China's foreign exchange reserves and consumption of urban residents date from 1981 to 2003. Data sources is from *Statistical Yearbook of China 2005*

2.1 Polynomial fitting model

Build 3-order polynomial fitting model based on least squares method:

$\hat{y}_i = 0.0000000140\ 4x_i^3 - 0.0000204906\ 3x_i^2 + 0.1323783246\ 2x_i - 37.5053646378$, where $i = 1, 2, \cdots n$.

2.2 Local polynomial regression estimation model

Build non-parameter local polynomial regression estimation model of consumption of urban criticizes and foreign exchange reserves according to theorem 1.1 and theorem 1.2, where *p*=3, *h*=250. The results are shown in Figure 1, Figure 2, Table 1, and Table 2.

The fitting results of the foreign exchange reserves by polynomial fitting model and non-parameter local polynomial regression estimation model are shown in Figure 1, in which the dot-line represents the fitting curve of polynomial fitting model and the solid line represents the fitting curve of non-parameter local polynomial regression estimation model. Figure 2 shows the estimate value of the two models at x_i, in which □ represents the fitting value y_i at point x_i based on polynomial fitting model, while ○ represents the estimate value at point x_i based on non-parameter local polynomial regression estimation model. Symbol * represents the actual value in both Figure 1 and Figure 2.

As shown in Figure 1, the fitting curve in non-parameter local polynomial regression estimation model tallies with the actual situation better than that of polynomial fitting model. In Figure 2, fitting values in both models tallies with the actual values, but the former is superior to the latter. This can be drawn from table 1 and table 2.

As can be seen from the above chart, at the beginning of China's reform and opening up, the relationship between the consumption of urban residents and foreign exchange reserves was not stable and the volatility couldn't be neglected. However, with the continuous deepening of China's reform and opening up, expending trade with other countries, improvement of the market economic system and perfection of national policy, the relationship between the consumption of urban residents and foreign exchange reserves in more and more stable, which creates a favorable condition for our studies

Using polynomial fitting model and non-parameter local polynomial regression estimation model respectively, to predict the value of China's foreign exchange reserve in 2004, the difference between the former result and the actual result is large (error is larger than 1000) while the later is close to (error is less than 50).

3. Conclusion

In actual economic life, due to the unpredicted reasons, it is difficult to make specific assumption. With the improvement of the market economic system and increasingly close connection between China and world economy, the correlation between consumption of urban residents and foreign exchange reserve is more and more stable. Non-parametric local polynomial regression estimation model has the regression function form of arbitrariness, lower requirement than polynomial fitting model, and no need to consider the distribution of the sample, making non-parametric local polynomial regression estimation the best reflection of correlation between variables, and the errors are smaller than the polynomial fitting model.

References

Huiming, Zhu and Yuqi, Han. (2002). An empirical analysis of the equilibrium relationship between the per capital annual income and living expenditure in urban households. *Journal of Lanzhou Commercial College*.18 (5):7-10. (in Chinese)

Larry, Wasserman, Translate by Xizhi, Wu. (2008). *All of Nonparametric Satistics[M]*. Beijing: Science

press.pp.57-62.(in Chinese)

Xiaodong, Shen and Weiya, Zhao. (2005). The dynamic relationship between the per capital annual income and living expenditure in urban households - an empirical analysis based on nonparametric regression model [J]. *Economic Science*.1, 18-22 (in Chinese)

Xiaoqun, He. (1997). *Regression Analysis and Economic Data Modeling [M]*. Beijing: China Renmin University Press. (Chapter3-4) (in Chinese)

Xiru, Chen and Songgui, Wang. (1987). *Modern Regression Analysis- principle method and application[M]*. Hefei: Anhui Education Press.pp.155-161 (in Chinese)

Xizhi, Wu and Zhaojun, Wang. (1996). *Nonparametric Statistical Method [M]*.Beijing: Higher Education Press,(Chapter4) (in Chinese)

YE, A-zhong. (2002). Nonparamet ric Regression Model of Chinese Inflation[J]. *Aplication of Statistics and Management*.21 (1):47.(in Chinese)

YE, A-zhong. (2003). *Nonparameter Econometrics[M]*. Tianjing: Nankai University Press,(Chapter6).(in Chinese)

Zinai, Li. (2000). *Econometrics [M]*. Beijing. Higher Education Press, (Chapter5).(in Chinese)

Table 1. Comparison of MSE in two models

Polynomial fitting model	103.8655
Non-parameter local polynomial regression estimation model	17.0623

Table 2. Comparison of fitting values in two models

| Year	x_i	y_i	$\hat{y}_i$	$\hat{r}_n(x_i)$
1981	456.80	27.08	20.0274	54.5065
1982	471.00	69.86	21.7659	59.2710
1983	505.92	89.01	26.0406	65.9079
1984	559.44	82.20	32.5972	65.8314
1985	673.20	26.44	46.6082	47.1090
1986	798.96	20.72	62.3389	27.2955
1987	884.40	29.23	73.2534	21.9781
1988	1103.98	33.72	102.552	46.2960
1989	1210.95	55.50	117.678	80.6515
1990	1278.89	110.93	127.641	109.192
1991	1453.81	217.12	154.773	176.117
1992	1671.73	194.43	192.114	208.330
1993	2110.81	211.99	282.644	211.757
1994	2851.34	516.20	498.775	516.180
1995	3537.57	735.97	795.817	735.526
1996	3919.47	1050.49	1011.80	1059.72
1997	4185.64	1398.90	1186.98	1360.56
1998	4331.61	1449.59	1292.33	1459.37
1999	4615.91	1546.75	1517.54	1537.87
2000	4998.00	1655.74	1864.86	1666.11
2001	5309.01	2121.65	2188.30	2120.80
2002	6029.88	2864.07	3093.34	2864.07
2003	6510.94	4032.51	3830.33	4032.51
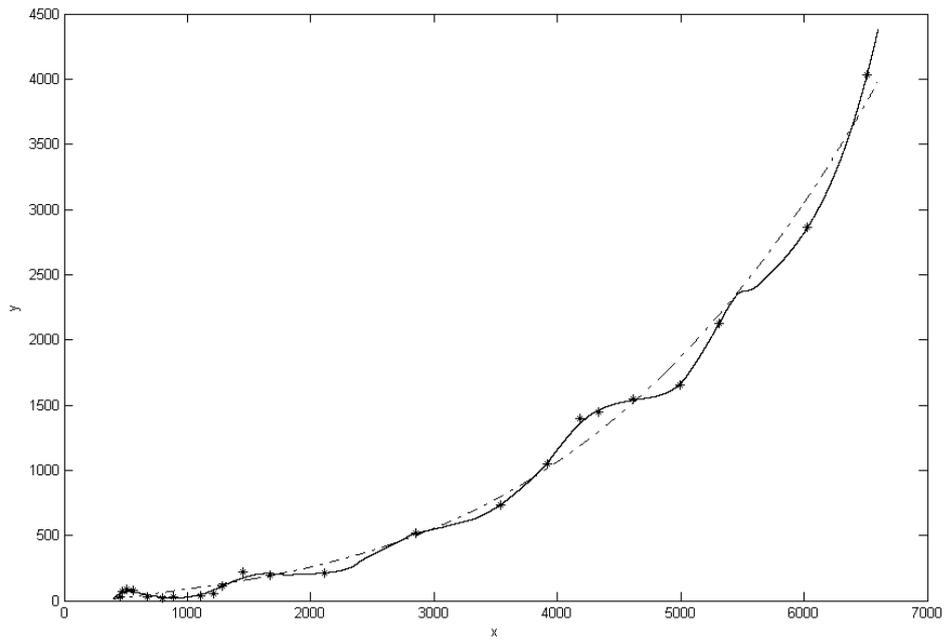
Figure 1. Fitting curve in two models
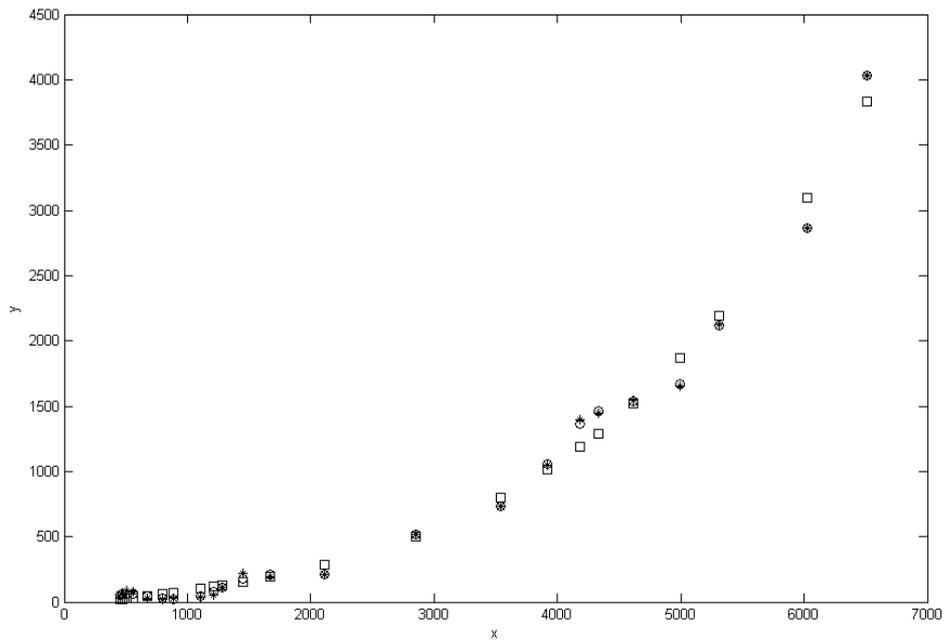
Figure 2. Fitting value in two models

Modular PCA Face Recognition Based on Weighted Average

Chengmao Han (Corresponding author)

Department of Mathematics, Linyi Normal University

Linyi 276005, China

E-mail: hanchengmao@163.com

Abstract

This paper presents an improved modular PCA approach, that is, modular PCA algorithm based on weighted average. This algorithm extracts weighted average for every sub-block of every training sample in each type of training sample, and normally operates the corresponding sub-block in training sample using weighted average, then all standardized sub-blocks constitute the overall scatter matrix, and thus the optimal projective matrix is obtained; From the middle value of sub-blocks in training set, and normally projecting sub-blocks of training samples and test samples to the projective matrix, then we can get identified characteristics; At last, use the recent distance classifier to class. The test results in the ORL face database show that the proposed method in identifying performance is superior to ordinary modular PCA approach.

Keywords: Face recognition, Principal component analysis, Weighted average

Face recognition is an active subject in the current pattern recognition field, which has broad application prospects[Valentin D, 1994-Zhang Cuiping, 1995] and has a lot of algorithms[J.Lu, 2003-Gan Junying, 2007]. In the human face image recognition, principal component analysis (PCA)[Kriby M., 1990] also known as KL transformation, is considered one of the most successful linear discriminant analysis methods, which is still widely used in image recognition field such as human face, etc. PCA method can not only effectively reduce the dimension of human face images, but also retain its key identifying information. However, this method requires the matrix of human face image pre-converted into one-dimensional vector, and then takes vector as the original characteristic to feature extraction. For the dimension of the converted one-dimensional vector is generally higher, extracting the subsequent feature causes difficulty, which makes the following algorithm has higher computational complexity. In addition, in face recognition when the facial expression and illumination conditions change largely, for the ordinary PCA method extracts the global features of image, its identification results are unsatisfactory. In fact, when facial expression and illumination conditions change, only some face significants variate, but little changes in other parts, or even no change. Discriminant analysis for the blocked sub-images can capture local information characteristics of human face, thus help identify.

Chen Fubing[Chen Fubing, 2007] proposed blocked PCA algorithm based on traditional PCA method. This method, first blocks an image, then discriminant analyses the blocked sub-images using PCA. Its characteristics are able to effectively extract the local characteristics of images, especially for the images whose facial expressions and illumination conditions change largely. Compared with the PCA method, blocking the original digital image, can not only easily reduce the dimension of image vector by two powers, but also increase the sub-images number of training samples by two parts, which converts the small sample problem into large sample problem to deal with and can reduce complexity of the problem

average face method proposed by He Guohu[He Guohu,2006] effectively increases the distance between the samples of different categories, while narrowing the distance between the samples, that is, making the distance between classes larger and distance smaller, which is conducive to identification, and improves the correct recognition rate of human face.

However, in small sample cases, average cannot guarantee that average of various types of training samples is the center of this sample distribution. And the projective matrix taken from the average of training sample as the center of this class samples can not guarantee to be optimal.

In order to further improve the recognition performance of PCA method and reduce the influence of taking the optimal projective matrix by average derivation center of training samples. This paper presents an improved modular PCA approach based on the above method and by the adaptive weighted average idea in paper [Yin Hongtao,2006], that is modular PCA approach based on weighted average. This algorithm extracts weighted average for every sub-block of

every training sample in each type of training sample, and normally operates the corresponding sub-block in training sample using weighted average. The test results in the ORL face database show that the proposed method in identifying performance is superior to ordinary modular PCA approach.

1. PCA Algorithm

PCA method is a statistical analysis method based on Karhunen-Loeve (KL) transformation, whose principle is that high-dimensional vector projects to low-dimensional vector space by a specific feature vector matrix. Through the vector of low-dimensional representation and the feature vector matrix, we can reconstruct the corresponding original high-dimensional vector. In the face recognition process, after the KL transformation, we can get a set of feature vectors to form a lower dimensional subspace. Any human face image can project it and get a set of coordinates factors. This group of coefficients shows that the image location in the sub-space can be used as a basis for face recognition.

In this method, generating matrix is the total scatter matrix of training samples, i.e:

$$S = \frac{1}{M}\sum_{i=1}^{M}\left(X_i - \overline{X}\right)\left(X_i - \overline{X}\right)^T = \frac{1}{M}XX^T \quad , \tag{1}$$

Where X_i is the image vector of the i-th training sample; Vector dimension is n; $\overline{X}$ is the average figure vector for training sample; M is the total number of training samples.

According to the general scatter matrix, we can derive a set of orthogonal eigenvectors $u_1, u_2, \cdots, u_n$, and its corresponding characteristic values are $\lambda_1, \lambda_2, \cdots, \lambda_n$. Through choosing the corresponding eigenvectors of the previous $m\,(m < n)$ non-zero eigenvalues as the orthogonal basis, in the new orthogonal sub-space U, the face sample X_i can be expressed as:

$$Y_i = U^T X_i \tag{2}$$

2. Adaptive weighted average [Yin Hongtao, 2006]

When using PCA algorithm, we first spread the image matrix by row (column) as a vector. Suppose the vector spread by all the image matrix be:

$$X_j^{(i)} = \left(X_{(j,1)}^{(i)}, X_{(j,2)}^{(i)}, \cdots X_{(j,m)}^{(i)}\right)^T \quad , \tag{3}$$

Where $i = 1, 2, \cdots, c$, c is the type number of training samples; $j = 1, 2, \cdots N_i$, is the number of the i-th training sample; m is the vector dimension. Because the mean vector of several vectors is taken averagely from the scalar vector of the corresponding dimension, we explain the determined method of weighted value by taking the first dimension as example.

First of all, calculate the distance sum $d_{j,1}^{(i)}(j = 1, 2, \cdots, N_i) d_{j,1}^{(i)}(j = 1, 2, \cdots, N_i)$ of every sample in the i-th sample and other sample, then find the minimum of them $d_1^{(i)} = \arg\min_j \left(d_{(j,1)}^{(i)}\right) d_1^{(i)}$.

We believe that the sample whose distance sum with the same type sample is larger. It deviates greater from the class center. In calculating class average, it should be given a smaller weight and the weighted value in the first dimension of the j-th sample in the i-th class is

$$\mu_{(j,1)}^{(i)} = 1 + \beta \frac{d_1^{(i)}}{d_{(j,1)}^{(i)}} \quad , \tag{4}$$

where β is a constant greater than or equal to zero. For regulating the weight extent, when $\beta = 0$, the algorithm becomes the traditional averaging method. The average of the first dimension in the i-th sample can be modified to

$$\tilde{X}_1^{(i)} = \frac{\sum_{j=1}^{N_i}\mu_{(j,1)}^{(i)} X_{(j,1)}^{(i)}}{\sum_{j=1}^{N_i}\mu_{(j,1)}^{(i)}} \tag{5}$$

Similarly, we can find the means of other dimensions of training samples.

3. Modular PCA algorithm based on the weighted average

The basic idea of modular PCA algorithm based on the weighted average is as follows: block $m \times n$ image matrix I into $p \times q$ blocked image matrix, namely,

$$I = \begin{pmatrix} I_{11} & I_{12} & \cdots & I_{1q} \\ I_{21} & I_{22} & \cdots & I_{2q} \\ \vdots & \vdots & \ddots & \vdots \\ I_{p1} & I_{p2} & \cdots & I_{pq} \end{pmatrix} \tag{6}$$

Where each sub-image matrix I_{kl} is a $m_1 \times n_1$ matrix, $pm_1 = m$, $qn_1 = n$, then taking the sub-image matrix of all training samples as the image vector of training sample to purpose PCA method. The difference from the traditional PCA algorithm is that we derive all scatter matrix not using the sub-block average of all training samples, but using weighted average of sub-blocks. This can reduce the impact of deriving the optimal projective matrix from the mean deviation in training samples, thus improving the recognition rate.

Algorithm steps are as follows:
For convenience, we first introduce the concept of quantization matrix.

Definition: Suppose $A = (A_1, A_2, \cdots, A_n) \in R^{m \times n}$, $mn \times 1$ vector is defined as

$$Vec(A) = \begin{pmatrix} A_1 \\ A_2 \\ \vdots \\ A_n \end{pmatrix}, \tag{7}$$

Where the vector is arranged in turn by column vector of the matrix A, which is called the quantification of matrix A.

1) Suppose the model category is C, the image matrix in the i-th class training sample is $n(i)$; A_{i1}, A_{in_i}, $N = \sum_{i=1}^{c} n(i) N$ is the total number of training samples, and each sample image is $m \times n$ matrix. The $p \times q$ blocked matrix of training sample image A_{ij} is expressed as:

$$A_{ij} = \begin{pmatrix} (A_{ij})_{11} & (A_{ij})_{12} & \cdots & (A_{ij})_{1q} \\ (A_{ij})_{21} & (A_{ij})_{22} & \cdots & (A_{ij})_{2q} \\ \vdots & \vdots & \vdots & \vdots \\ (A_{ij})_{p1} & (A_{ij})_{p2} & \cdots & (A_{ij})_{pq} \end{pmatrix} \tag{8}$$

2) Require overall scatter matrix of sub-image matrix in all the training sample images.

Let $(\eta_{ij})_{kl} = Vec(A_{ij})_{kl}$, $k = 1, 2, \cdots, p$, $l = 1, 2, \cdots, q$, then $(\eta_{ij})_{kl} \in R^{m_1 \times n_1}$. So the overall scatter matrix of all training sample sub-blocks is:

$$S = \frac{1}{M} \sum_{i=1}^{C} \sum_{j=1}^{n(i)} \sum_{k=1}^{p} \sum_{l=1}^{q} \left((\eta_{ij})_{kl} - (\eta_{kl})_i \right) \left((\eta_{ij})_{kl} - (\eta_{kl})_i \right)^T . \tag{9}$$

Where $i = 1, 2, \cdots, C$; $j = 1, 2, \cdots n(i)$; $k = 1, 2, \cdots p$; $l = 1, 2, \cdots, q$, $n(i)$ is the number of each class of training samples;

$$M = \left(\sum_{i=1}^{c} n(i) \right) pq = Npq \tag{10}$$

is the total number of training sample sub-images matrix. .

$(\eta_{kl})_i$ is the weighted average image between the i-th sample image and the kl-th block. The specific calculation method is to spread all sub-blocks by row to column vector, then calculates its weighted mean vector by equations (4) and (5), and reverts the middle measures to a matrix.

Easily, we can prove S is a $m_1 n_1 \times m_1 n_1$ non-negative definite matrix.

3) Seek optimal projective matrix

Take corresponding orthonormal eigenvectors (discriminant vectors) $Z_1, Z_2, \cdots, Z_r$ of the r largest eigenvalue of S to constitute

$$Q = [Z_1, Z_2, \cdots, Z_r],$$

4) Require weighted average vector of all training sample sub-blocks matrix

In order that test samples and training samples are comparable, standardize them by the same weighted average matrix. So we must calculate weighted average matrix η of all training sub-block samples.

5) Feature extraction of training samples.

Each block of training samples $A_{ij} = \begin{pmatrix} (A_{ij})_{11} & (A_{ij})_{12} & \cdots & (A_{ij})_{1q} \\ (A_{ij})_{21} & (A_{ij})_{22} & \cdots & (A_{ij})_{2q} \\ \vdots & \vdots & \vdots & \vdots \\ (A_{ij})_{p1} & (A_{ij})_{p2} & \cdots & (A_{ij})_{pq} \end{pmatrix}$ is quantified by equation (7) and normalized, then

obtain the characteristics matrix of A_{ij} after projecting to $Q = [Z_1, Z_2, \cdots, Z_r]$:

$$B_{ij} = \begin{pmatrix} Q^T\left((\eta_{ij})_{11} - \eta\right) & Q^T\left((\eta_{ij})_{12} - \eta\right) & \cdots & Q^T\left((\eta_{ij})_{1q} - \eta\right) \\ Q^T\left((\eta_{ij})_{21} - \eta\right) & Q^T\left((\eta_{ij})_{22} - \eta\right) & \cdots & Q^T\left((\eta_{ij})_{2q} - \eta\right) \\ \vdots & \vdots & \vdots & \vdots \\ Q^T\left((\eta_{ij})_{p1} - \eta\right) & Q^T\left((\eta_{ij})_{p2} - \eta\right) & \cdots & Q^T\left((\eta_{ij})_{pq} - \eta\right) \end{pmatrix}_{pr \times q} . \tag{11}$$

6) Feature extraction of test samples

Each block of test sample image $I_x = \begin{pmatrix} I_{11} & I_{12} & \cdots & I_{1q} \\ I_{21} & I_{22} & \cdots & I_{2q} \\ \vdots & \vdots & \vdots & \vdots \\ I_{p1} & I_{p2} & \cdots & I_{pq} \end{pmatrix}$ is quantified by equation (7) and normalized, then obtain the

characteristics matrix of test samples after projecting to $Q = [Z_1, Z_2, \cdots, Z_r]$:

$$B_x = \begin{pmatrix} Q^T\left(\eta_{11} - \eta\right) & Q^T\left(\eta_{12} - \eta\right) & \cdots & Q^T\left(\eta_{1q} - \eta\right) \\ Q^T\left(\eta_{21} - \eta\right) & Q^T\left(\eta_{22} - \eta\right) & \cdots & Q^T\left(\eta_{2q} - \eta\right) \\ \vdots & \vdots & \vdots & \vdots \\ Q^T\left(\eta_{p1} - \eta\right) & Q^T\left(\eta_{p2} - \eta\right) & \cdots & Q^T\left(\eta_{pq} - \eta\right) \end{pmatrix}_{pr \times q} , \tag{12}$$

where $\eta_{kl} = Vec(I_{kl})$, $l = 1, 2, \cdots, q$.

7) Sort

Suppose $B_{ij} = \left[Y_1^{(ij)}, Y_2^{(ij)}, \cdots, Y_q^{(ij)}\right]$, $B_x = \left[Y_1^{(x)}, Y_2^{(x)}, \cdots, Y_q^{(x)}\right]$, carrying the most recent method to sort:

$$d\left(B_{ij}, B_x\right) = \sum_{m=1}^{q} \left\| Y_m^{(ij)} - Y_m^{(x)} \right\|_2 \tag{13}$$

$i = 1, 2, \cdots, C$; $j = 1, 2, \cdots n(i)$; x is identified the x -th sample under test.

If $d\left(B_{nj}, B_x\right) = \min_i d\left(B_{ij}, B_x\right)$, the sample I_x belongs to the i -th category.

4. Experiment and result analysis

Test the method of this paper in ORL (olivetti research laboratory) face database. This face database contains 40 individuals, and each person has 10 images. The image is a positive image of single dark background that contains a certain amount of illumination changes, facial changes (open eyes   and closed eyes , laughing or not laughing), facial details changes(wearing glasses or not wearing glasses), and the depth rotation within a certain range. The sizes of these images are 112 × 92 pixels. Other part faces are showed in Figure 1. For each person, randomly selecte five images as training samples and the rest five images are used to test the identification method performance.

The experimental results are shown in Figure 2 and Figure 3. Figure 2 shows experimental result of traditional PCA method, 2×2 modular PCA method and 2×2 blocked PCA method based on weighted average. From the figure, we can see that recognition rate of traditional PCA method is lower, that is up to 77 %.   Module PCA method improves the recognition rate, while the blocked PCA method based on weighted average is superior to ordinary blocked PCA method. Figure 3 respectively shows the test results of 4×2 sub-blocks and 4×4 sub-blocks conditions. From the figures we can see that in the 4×2 block case, modular PCA method based on weighted average has a higher recognition rate and a more robust than ordinary blocked PCA method; In addition, test result also shows that 4×2 blocked approach is superior to 2×2 blocked approach. In the blocked mode, the correct recognition rate is greatly decreased. The cause is that the more blocks number of each image is, the more reduced the distinguished information contained in each sub-block. So there will be more similar sub-blocks and it is not conducive to classification, thus correct identification rate has dropped. In this case, modular PCA method based on weighted average is still better than ordinary blocked PCA method. At the same time, we find in experiments the recognition performance of 4×2 sub-blocks is far better than that of 2×4 sub-blocks, which is shown in Table 1. The cause is that the difference between different people faces focus on eyes, nose, mouth, chin and other parts, so the vertical multi-block is not conducive to identification.

5. Conclusion

The prominent advantage of face recognition method based on modular PCA is the ability to extract the local features of image, which better reflects the difference between images. We can easily use discriminant analysis method in the smaller image for the process is simple. To further improve the recognition rate, this paper improves face recognition method based on modular PCA and proposes modular PCA algorithm based on weighted average. The experiment on ORL face database shows that this method is superior to the traditional PCA method and ordinary PCA method. For the same database, if the original image has different sub-blocks, the obtained highest recognition rate is generally different. How to find the best sub-blocks acquired highest recognition rate and how to simplify the sub-blocks PCA algorithm have yet to be further studied.

References

Chen Fubing, Yang Jingyu. (2007). Modular PCA and its application in human face recognition. *Computer Enineering and Design*,28(8):1889-1913.

Gan Junying, Li Chunzhi. (2007). 2DICA based on wavelet transformation and application. *Journal of System Simulatio*n,19(3):612-619.

He Guohui, Gan Junying. (2006). Study for class average face method based on PCA in face recognition. *Application Reseach of Computer*, 3:165-169.

J. Lu, K. Plataniotis, A.Venetsanopoulos.(2003). Face Recognition using LDA-based Algorithms[J]. *IEEE Trans*. Neural Networks, 14 (1):195-200.

Jian Yang, David Zhang. (2004). Two-Dimensional PCA: A New Approach to Appearance-Based Face Representation and Recognition [J]. *IEEE Trans. Pattern Analysis and Machine Intelligence*, 26(1):131-137.

Keun-Chang Kwak, Witold Pedrycz. (2007). Face Recognition using an Enhanced Independent Component Analysis Approach[J]. *IEEE Trans*. Neural Networks, 18(2):530-541.

Kirby M, Sirovich L.(1990). Application of the KL Procedure for the Characterization of Human Faces[J].*IEEE Trans*. Pattern Analysis and Machine Intelligence, 12(1):103-108.

Rama Chellappa, et al.(1995). *Human and Machine Recognition of Faces: A Survey[J]*. Proceedings of the IEEE, 83(5): 705-740.

Valentin D, Abdi H, OToole A J. (1994). *Connectionist Model of Face Processing: A Survey [J]*. Pattern Recognition, 27(9): 1209-1230.

Yin Hongtao, Fu Ping, Meng Shengwei. (2006). Face recognition based on adaptively weghted Fisherface. *Journal of Optoelectronics. Laser*,17(11):1405-1408.

Zhang Cuiping, Sun Guangda. (2005). A survey on face recognition. *Journal of Image and Graphics,* 5(11):885-894.

Table 1. recognition rate of 2×4 blocks and 4×2 blocks of method in this paper (%)

recognition rate number	5	10	15	20	25	30	35	40
2×4 blocks	84.5	85	85.5	85.5	85	86	85.5	85
4×2 blocks	91.5	92	91.5	92	91.5	91.5	91.5	91.5

Figure 1. image in ORL face database
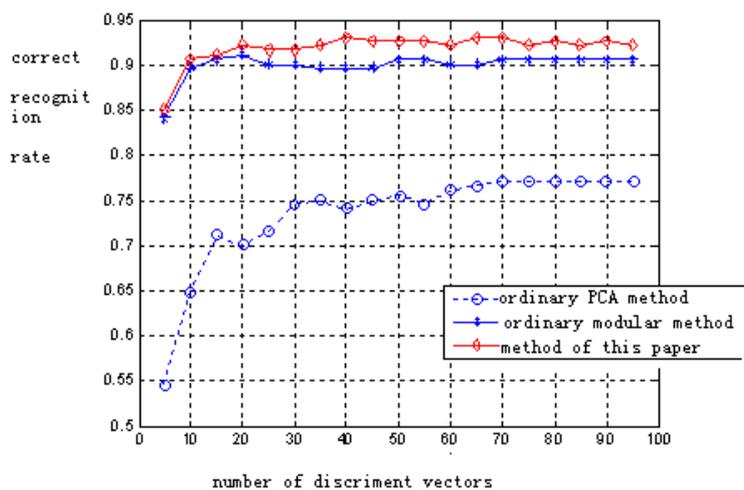
Figure 2. Experimental result of 2×2 sub-blocks
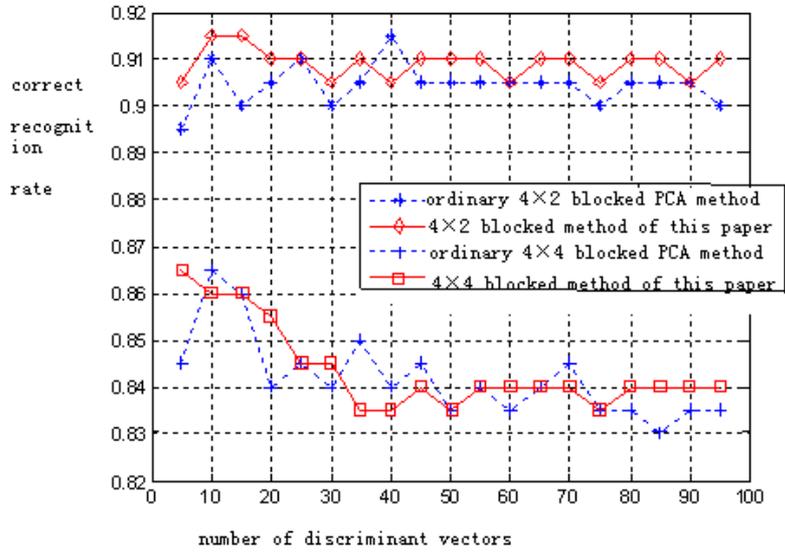
Figure 3. Experiment result of 4×2 blocks and 4×4 blocks

Reliability Growth Testing Based on Dynamic Planning Methodology

Lu Yao, Jing Yang, Jianjun Yang & Kai Chen

Department of Management Science, Naval University of Engineering

Wuhan 43003, China

E-mail: fzqy2046@163.com

Abstract

The reliability growth test is known as to stimulate malfunction, analyze the cause of the malfunction and improve of the design designedly, and carry out tests is to prove the effectiveness of improving measures. A large number of projects practice has proved that reliability growth test is an important and effective way in various stages of the work of the equipment reliability growth. This model search for the optimum target of reliability growth testing to make the cost using in whole reliability grow project in a low amount by considering the reliability growth testing as one stage of reliability grow project and basing on Dynamic Planning Methodology. Through the use of Dynamic Planning Methodology to arrange the target value at every stage of the work, so as to achieve the purpose of the minimum cost of the whole reliability project. After the target value is confirmed at the end of the various stages of the project, the target of growth of the reliability growth test as one of the projects is also determined accordingly.

Keywords: Reliability growth testing, Target of growth, Dynamic planning

1. Instruction

Target of growth of test is one of the important indexes that the test needs to establish, the reasonable growth targets will not only guarantee to achieve a satisfactory test results, but also shorten the test time and save the costs. (Mei, 2001, p.75).During determining the target of tests, we not only consider the cost savings of the test, but consider the reliability growth testing as one stage of reliability grow project in the premise of Technical Support.

2. Build Cost Model

This section takes the ultimate reliability level of the system as a state variable, the reliability of the completion of the Items (that is, the MTBF at the end of the work of the project) (Jin, 2002, p.119).as a decision-making program to establish optimal model. In order to determine the MTBF values at the end of the various stages of the project, so that under the premise of the reliability level of the product will meet the required the implementation of the decision-making make the total reliability cost the lowest. When the MTBF values are determined at the end of the various stages of the project, Target of growth as one project of the Reliability growth tests is determine accordingly. (Liu, 2000, p.63-65).

On the assumption that in the process of product development Products have the total number of n items which can increase the reliability of products, including reliability growth test is the a project, the n work items have the time sequence, that is, after one of the projects is completed, the next work project starts, every project is on the basis of the preparatory work project. Clearly, the Completion Description of preparatory work will directly affect the costs inputs and Completion Description of the late work, thereby affecting the total cost of the development of products.

The following index model is a frequently-used cost account model in the reliability growth testing:

$$C = A + B\left(\frac{M_z}{M_q}\right)^{\beta}$$

(1)

Among them, C express the development costs for product reliability; A as the basic fixed costs; B as the variable costs; M_q as the original MTBF value of Product; M_z as the MTBF value of the product is improved; β as for the model parameters that can be obtained by fitting.

This article consider any the work of the project which caused reliability growth , can make use of the above-mentioned model, but the different project have different content itself, so their basic costs, variable costs and model parameters are not the same, the specific values can be accessed by the project's own related data. Thus, cost model of any i

project as follows:

$$C_i = A_i + B_i \left(\frac{M_i}{M_{i-1}} \right)^{\beta_i}$$

(2)

Among them, M_{i-1} as at the end of the preparatory work project, the MTBF value at the beginning of the work item; M_i as the MTBF value at the end of the work item.

Correspondingly, the total reliability project cost is sum of the reliability costs of each sub-project: $C = \sum_{i=1}^{n} C_i$

3. Build Optimization Models

On the assumption that the initial value of the MTBF of Products is M_0, according to the order we carried out project work in order to increase the reliability of products, so that the final value of the MTBF is M, in which the reliability growth test is the a ($1 \le a \le n$) projects. In this paper, the optimal strategy is as follows:

By adopting the ultimate reliability level of system as a state variable, the completion of the reliability of the projects (that is, the value of MTBF at the end of the work of the project). (Gan, 1999, p.69).as a decision-making program to establish optimal model. In order to determine the MTBF values at the end of the various stages of the project, so that under the premise of the reliability level of the product will meet the required the implementation of the decision-making make the total reliability cost the lowest.

Specific optimization model is as follows:

$$MinC(M) = \sum_{i=1}^{n} A_i + B_i \left(M_i / M_{i-1} \right)^{\beta_i} \quad \cdots\cdots \qquad\qquad \cdots\cdots\cdots(3)$$

$$\text{s.t. } M_0 \le M_1 \le \cdots \le M_{n-1} \le M_n = M$$

4. The Research of Model Solution

Since variables of the model can not be separated, so it can not be directly solved by dynamic programming methods. In this paper, variables are separated through introducing magnification factor k_i to the model. The definition of magnification factor k_i is enlarging multiples of the value of MTBF of product compared with the early start of the project after the i work item. Substitute it into the optimization model formula can be turned into:

$$MinC(k_i) = \sum_{i=1}^{n} A_i + B_i (k_i)^{\beta_i} \quad \cdots\cdots \qquad \cdots\cdots(4)$$

$$s.t. \begin{cases} k_i = M_i / M_{i-1} \\ 1 \le k_i; \ k_1 * k_2 \cdots k_{n-1} * k_n = \dfrac{M}{M_0} \end{cases}$$

For the above-mentioned formula, it can be solved by the dynamic programming order method.

Set up: When a work item corresponds to a phase, that is, the number of phase sequence is i ; the state variable is defined as the multiples which has been enlarged of the value of MTBF of the product before stage i ,decision-making variables k_i expresses enlarge multiples of the value of MTBF of Products from stage $i-1$ to stage i

The state transition equation is as follows: $s_{i+1} = s_i * k_i$

Set of admissible decisions is $D_i(s_i)\{1 \le k_i \le s_{i+1}\}$

Index function at various stages is the cost inputs of each working item: $v_i(k_i) = A_i + B_i k_i^{\beta_i}$

The optimal function values expresses the spent minimal cost by magnifying the value of MTBF of the product in the working item i by k_i times, thus the order recursion relations of the dynamic programming can be written into:

$$f_i(s_{i+1}) = Min\{v_i(s_{i+1}, k_i) + f_{i-1}(s_i)\} \quad \cdots\cdots \qquad \cdots\cdots\cdots(5)$$

$$i = 1, 2, \cdots, \ n$$

Among them, at the time $s_0 = 1$,it means that the cost inputs of product is zero when the value of MTBF of product is not increased, that is, the boundary conditions are as follows: $f_0(s_1) = 0$

According to the above methods, we can get the magnification factor k_i of each work item; the value of MTBF at the

end of the work item is $M_i = M_{i-1} * k_i$ among $i \geq 1$ and M_0 is known.

Accordingly, the growth objectives of the a Reliability growth testing can be established: $M_a = M_{a-1} * k_a$.

5. Examples

Known in the process of some product development, the initial value of MTBF of product is $M_0 = 100$ hours, now we plan to improve of the value of MTBF which will not be less than $M_3 = 900$ hours through three reliability work item, the three projects carried out by time sequence, in which reliability growth testing is the second work item.

The cost of Three working project and the relationship model of reliability are as follows:

$$C_1 = 350 + 300 \left(\frac{M_z}{M_q} \right)^2 ,$$

$$C_2 = 400 + 280 \left(\frac{M_z}{M_q} \right)^{2.5} ,$$

$$C_3 = 500 + 350 \left(\frac{M_z}{M_q} \right)^3$$

M_z is the value of MTBF at the end of the work item;

M_q is the value of MTBF at the beginning of the work item.

Requested under the premise of meeting the requirements the final value of MTBF of Products, we arrange for the three projects reasonably, making the total cost of reliability the lowest.

By substituting Known conditions into the above optimization model we get:

$$Min C(k) = 1250 + 500k_1^2 + 300k_2^{2.5} + 500k_3^3$$
$$s.t. \begin{cases} 1 \leq k_i; \\ k_1 * k_2 * k_3 = 9 \end{cases}$$
……… ……….(6)

in that $k_i = M_i / M_{i-1}$, $i = 1, 2, 3$.

Three work items can be taken as a three-stage decision-making problem set state variables are s_1, s_2, s_3, s_4 ,

s_i expresses the multiples which has been expanded compared with the values of MTBF of the Product at early stages i , $s_1 = 1$

Adopting k_1, k_2, k_3 as the decision variable;

Index function at various stages is:

$$v_1(k_1) = 1250 + 500k_1^2 ,$$
$$v_2(k_2) = 500k_2^{2.5} ,$$
$$v_3(k_3) = 500k_3^3$$

The state transition equation is as follows:

$$s_1 = 1,$$
$$s_2 = s_1 * k_1,$$
$$s_3 = s_2 * k_2,$$
$$s_4 = s_3 * k_3 = 9$$
$$k_1 = s_2, \quad 1 \leq k_2 \leq s_3, \quad 1 \leq k_3 \leq s_4$$

Supposed the optimal value function $f_i(s_{i+1})$ expresses the minimum value of the cost of reliability from the first stage to the i stage, so the order recursion relations are:

$$\begin{cases} f_i(s_{i+1}) = Min\{v_i(s_{i+1},k_i) + f_{i-1}(s_i)\} \\ i = 1,2,3 \\ f_0(s_1) = 0 \end{cases} \quad \cdots\cdots \quad \cdots\cdots\cdots\cdots(7)$$

By substituting related conditions into the recursive relationship respectively and using differentiation we get:

$$k_1 = 2.695, k_2 = 2.0781, k_3 = 1.607$$

Then By substituting the initial value of MTBF of products into $f_i(s_{i+1})$,we can get the optimized reliability objectives of the work item are as follows:

$$M_1 = 235, M_2 = 560, M_3 = 900$$

So when we carry out the reliability growth testing, growth target of product may be set as its value of MTBF is 560 hours, the optimized purpose can be achieved.

6. Summary

It should be noted that:

When the model solution obtained is $k_i = 1$, purely from the economic perspective it means that the reliability of the work item is worthwhile and it should not be carried out.

However, in engineering practice, it does not mean that the work item can be omitted, we should arrange the work item by the required minimum input conditions of project, and then by substituting the cost and its growth of reliability which is regarded as a certainty value into the original model and resolving, we can get the optimized growth targets of other work item.

References

Gan, Ying'ai. (1999). *Operational Research*. (3rd ed.). Qing Hua University Press.

Jin, Bihui. (2002). *System Reliability Engineering*. National Defence Industry Press.

Liu, Xiaodong and Zhang, Hengxi. (2000). Flight System Reliability Develop Forecast Model Cost Research. *Quantity and Technology Economic Research*, 12, p.63-65.

Mei, Wenhua. (2001). *Reliability Growth Testing*. National Defence Industry Press.

Alteration of the Let-off and Take-up Machine of Loom SAURER 400

Bingyin Liu & Jianjun Sun

School of Mechanical and Electronic Engineering

Tianjin Polytechnic University, Tianjin 300160, China

E-mail: liubingyin@163.com

Abstract

At present, many shuttleless looms in Chinese enterprises still use the mechanical let-off and take-up machine, and to fulfill the requirements of modern textile technology and consider the factor of saving cost, most enterprises begin to alter their old looms. Taking the rapier loom SAURER400 as the research object, the original let-off and take-up machine of loom SAURER400 was analyzed in the article, and the electric let-off and take-up system was designed, and the revs of the let-off input end and the take-up input end were respectively computed, which could provide some references for the alteration of future electric let-off and take-up control system.

Keywords: Loom SAURER400, Let-off and take-up, Machine alteration

1. Introduction

The research object in the article is a SAURER400 rigid rapier loom imported from Switzerland, and the let-off and take-up machine of this loom is mechanical mode, and the drive of let-off and take-up is from the main shaft motor. The speed of the main shaft motor is different with the let-off and take-up speed, and a series of mechanical machines such as gears and chain wheels are needed between them, and the intension adjustment and the beam diameter change are accumulated by the mechanical machine, and the take-up machine needs the gear transformation to fulfill the change of the weft density, and the mechanical structure is complex (Zhu, 1996 & Run, 1998, P.63-66). At present, many Chinese enterprises have altered their mechanical let-off and take-up machines to electric let-off and take-up machines which adopt the independent motor to drive, and the intention control and the weft density change can be completed by adjusting the motor speed (The India Textile Journal Group, 2003, P.90). Based on that, some attempts about the alteration of electric let-off and take-up machine of loom will be made in the article (Wu, 2008, 47-48 & E.A.Plate, 1971, P.515-531). Through analyzing the mechanical let-off and take-up system drive of loom SAURER400, the alteration design will be made to adopt the electric let-off and take-up system.

2. Alteration design of the let-off system drive

2.1 Original let-off system machine

The let-off machine of loom SAURER400 is mechanical, and its drive is transferred by straps and gears and its structure sketch is seen in Figure 1.

The transmission ratio of the worm wheels and worms in the machine can be computed by the let-off machine. The teeth number of the manual gears are $Z_1=16$ and $Z_2=64$, and the teeth number of the let-off gear is $Z_{12}=53$, and the teeth number of the driving shaft beam flange gear is $Z_{13}=37$. So the total transmission ratio is i=111. So the three transmission ratios respectively are

$$i_1 = \frac{Z_2}{Z_1} = \frac{64}{16} = 4 \,, \quad i_3 = \frac{Z_{13}}{Z_{12}} = \frac{37}{53} \,, \quad i_2 = \frac{i}{i_1 \times i_3} = 39.75$$

Where, i_1, i_2 and i_3 respectively denote the first class transmission ratio, the second class transmission ratio and the third class transmission ratio.

2.2 Altered let-off system machine

The sketch of the altered electric let-off machine is seen in Figure 2. The mechanical transmission linkage is broken, and the independent step motor is used to drive the let-off machine as the let-off motor. In the sketch, the motor drives the gear 3 to gear with the gear 2 by the reducer, and drives to the coaxial worm and worm wheel with gear 2, and

drives to the let-off gear to gear with the beam flange gear, and finally drives to the driving shaft. The reducer, gear 2, gear 3 and worm wheel and worm can all reduce the speed of the motor.

The reduction ratio of the reducer is i_{10} =20, and the transmission ratio of the first class reduction gear is i_{11} =64/50, and the transmission ratios of the second class reduction gear and the third class reduction gear are same with the original machines, so the total transmission ratio is

$$i = i_{10} \times i_{11} \times i_2 \times i_3 = 20 \times \frac{64}{50} \times 39.75 \times \frac{37}{53} = 710.4 \tag{1}$$

2.3 Rev computation of the let-off motor

Supposed the diameter of the warp yarn is D, the weft density of the fabrics specs is P_w, so the required let-off quantity of each weft is

$$L_j = \frac{100}{P_w \times (1 - a_j)} \tag{2}$$

From $L_j = \omega D t / 2$,

$$\omega = \frac{200}{P_w \times (1 - a_j) \times D \times t} \tag{3}$$

The angular speed of the motor is

$$\omega_1 = i \times \omega \tag{4}$$

Where, ω is the angular speed of the beam (rad/s), ω_1 is the angular speed of the motor (rad/s), D is the warp yarn diameter of the driving shaft (mm), a_j is the off-machine shrinkage ratio, t is the let-off time (s), and i is the total transmission ratio of the motor.

If the maximum diameter of the driving shaft is $D_{max} = 500$mm, and the minimum diameter is $D_{min} = 200$mm, so $P_w = 137$ and $a_j = 16\%$.

After altering, i =710.4, the let-off time can be the rev time of the principal axis, and the rev of the principal axis is 332 rev/min, i.e. $t = 0.1807$, so from the formula (2), (3) and (4), the angular speeds of the altered motor are

$\omega_{1max} = 34.1623$rad/s, $\omega_{1min} = 13.6648$rad/s.

Where, ω_{1max} is the maximum angular speed of the motor, and ω_{1min} is the minimum angular speed of the motor.

3. Altered design of the take-up system drive

3.1 Original take-up system drive machine

The drive sketch of the original take-up machine of rapier loom SAURER400 is seen in Figure 3.

Through measurement and analysis, the shape size parameters of various drive parts in the gear-box can be obtained. For the gear, Z_1 =28 and m=2.5mm, and the gear tip diameter is d_{a1}=75mm, Z_2 =26, and m=2.5mm, and d_{a2}=70mm, Z_7 =19, m=4mm, and d_{a7}=78mm, Z_8=50, m=4mm, and d_{a8}=208mm. For the transmission gears Z_a and Z_b in the original equipment, according to the actual installed gears, Z_a=52, Z_b=46.

And through manual speed measurement, the rev ratio from the input end to Z_1 is N_I: N_{Z1}=10.62.

So the transmission ratio between them is $i_{1T} = 10.62 \tag{5}$

Where, the value of N_I is equal to the rev of the principal axis, i.e. 332 rev/min.

And the rev ratio between Z_7 and Z_b is $N_{Zb} : N_{Z7} = 26.43$.

So the transmission ratio between them is $i_{2T} = 26.43 \tag{6}$

Because the known the transmission value between Z_1 and Z_b is

$$i_{3T} = \frac{Z_2 \times Z_b}{Z_1 \times Z_a} = \frac{26 \times 46}{28 \times 52} = 0.82 \tag{7}$$

and

$$i_{4T} = \frac{Z_7}{Z_8} = \frac{50}{19} = 2.63 \tag{8}$$

From (5), (6), (7) and (8), the total transmission ratio of take-up is

$$i_T = i_{1T} \times i_{2T} \times i_{3T} \times i_{4T} = 605.7 \tag{9}$$

Therefore, under the transmission gears in the existing equipment, the total transmission ratio is 605.7, and according to the demands of different fabrics, the transmission gears can be changed, and the different total transmission ratio of the gear-box can be obtained.

3.2 Altered take-up system drive machine

The take-up machine is altered to be electric take-up machine, and the loom needs not to change the transmission gears because of the change of the fabrics or manufacturing requirements, it can only change the rev of the motor. The chain wheel 1 in the original take-up machine is remote and has large noise, and the take-up motor is added to this position, which will not impact the function of the take-up machine. The simplified machine sketch is seen in Figure 4.

The altered take-up machine adopts the drives between the synchronous transfer motor and the gear-box, the three-phase asynchronous motor, and the frequency conversion to adjust the speed.

Because of the demand of the actual installation, the space to install two gears is limited, so the maximum diameter of the gear can not exceed 80mm.

The small gear pitch diameter is $d_1 = 48.51\text{mm}$, and the teeth number is $Z_1 = 16$.

The big gear pitch diameter is $d_2 = 75.80\text{mm}$, and the teeth number is $Z_2 = 25$.

So the transmission ratio between them is

$$i_{5T} = \frac{Z_2}{Z_1} = \frac{25}{16} = 1.5625 \tag{10}$$

Because the structure of the gear-box is simplified, the corresponding sizes change, so the size of the interior parts in the gear box should be altered. Supposed that the transmission between Z_1 and Z_2 is

$$i_{3T}{}' = \frac{Z_1}{Z_2} = 0.79 \tag{11}$$

From (5), (6), (8) and (11), the total transmission ratio of the gear-box is

$$i_{6T} = i_{1T} \times i_{2T} \times i_{3T}{}' \times i_{4T} = 585.78 \tag{12}$$

From (10) and (12), the total transmission ratio of the altered take-up machine is

$$i_{TA} = i_{5T} \times i_{6T} = 915.24 \tag{13}$$

3.3 Rev computation of take-up motor

Take-up needs large torque, and the step motor can not fulfill the demand, so the TAIDA VFD-B transducer is adopted to drive the control AC motor.

The weft density is the weft amount weaved in the unit length (10cm), and it is divided into the on-machine weft density $P\omega'$ and the off-machine weft density $P\omega$ (Shi, 2003, P.185-187).

$$P\omega' = \frac{100}{L}$$

$$P\omega = \frac{P\omega'}{1-\alpha\%}$$

Where, $P\omega'$ is the theoretical weft density, $P\omega$ is the actual weft density, $\alpha\%$ is the off-machine shrinkage ratio which is related with the type of fabrics, the organization and density of fabrics, the amount of weft, the on-machine intension of yarn, and the temperature and humidity of the workshop, and L is the corresponding fabric crinkling length when the principal axis of the loom rotates one cycle (mm).

$$P\omega = \frac{100}{L \times (1-\alpha\%)} \tag{14}$$

Supposed that

$P\omega' = P\omega$

So, $P\omega = \dfrac{100}{L}$

$$\text{i.e.} \quad L = \frac{100}{P\omega} \tag{15}$$

Because $L = v \times t$

Where, v linear speed of the take-up roller, and t is the time that the take-up roller rotates in the distance of L.

And, $v = \omega' \times R$

Where, ω' is the angular speed of the take-up roller and R is the radium of the take-up roller, so,

$$\omega' = \frac{100}{P\omega \times R \times t} \qquad (16)$$

In the practice, the radium of the take-up roller is $R = 70\,mm$, and $t = 60/332 = 0.1807\,s$, so the rev of the cubing rolling n' is

$$n' = \frac{\omega' \times 60}{2 \times \pi} = \frac{6000}{2 \times \pi \times P\omega \times R \times t} \qquad (17)$$

From (13) and (17), the rev of the motor is

$$n = n' \times i_{\text{总}} = \frac{33200 \times i_{\text{总}}}{2 \times \pi \times P\omega \times R} = \frac{16600 \times 915.24}{3.14 \times 70 \times P\omega} = \frac{69121.86}{P\omega} \qquad (18)$$

4. Conclusions

First, the combination of the electric let-off and take-up machine and the flexible beam control system can obtain good real-time character, quick response, and automatic adjustment function, and the coherence of various fabric cycle intentions is good, and the filling phenomena of the machine stopping and starting can be improved obviously.

Second, the electric let-off and take-up system adopts two sets of independent drive sources, which can reduce the interference and make the measurement of the yarn intension more exact. The weft density setting of the electric let-off and take up machine is very convenient, and the altered range will be increased.

References

D.E.A.Plate & K.Hepworth. (1971). Beat-Up Forces in Weaving, Part 1. *Journal of the Textile Institute.* No.62(10). P.515-531.

Run, Gan. (1998). Development Tendency of Rapier Looms. Textile Accessories. No.3. P.63-66.

Shi, Weimin & Zhang, Lichao. (2003). The Electromechanical Control System of Loom. Mechanical & Electrical Engineering Magazine. No.20(5). P.185-187.

The India Textile Journal Group. (2003). Electronic let-off & take-up. *The Indian Textile Journal.* No.113(4). P.90.

Wu, Dongfeng. (2008). Study on the Electronic Let-off and Take-up System of Loom. Thesis of Tianjin Polytechnic University. P.47-48.

Zhu, Sukang & Chen, Yuanfu. (1996). *Weaving Theory.* Beijing: China Textile Press.
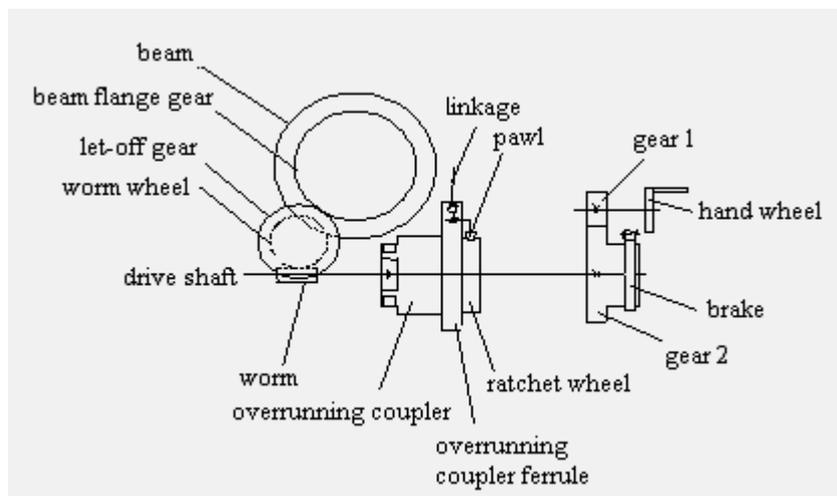
Figure 1. Sketch of Original Let-off Machine SAURER400
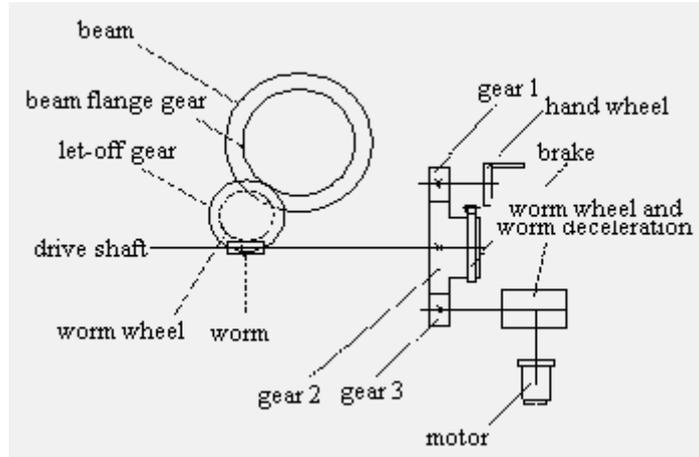
Figure 2. Sketch of Improved Electric Let-off Machine
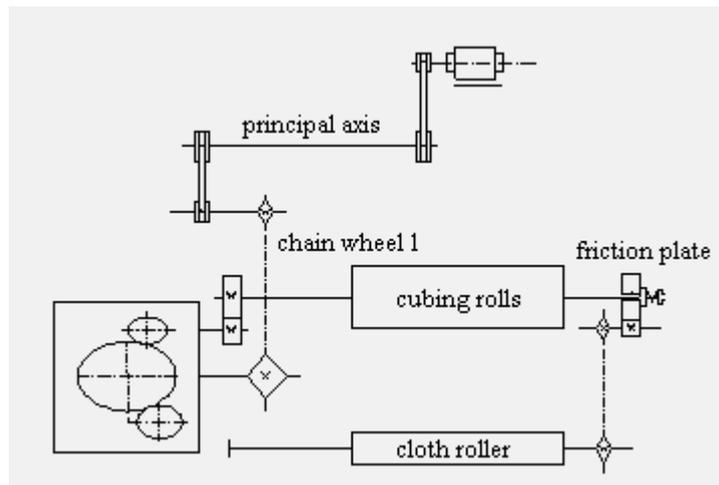
Figure 3. Sketch of Take-up Machine of Rapier Loom SAURER400
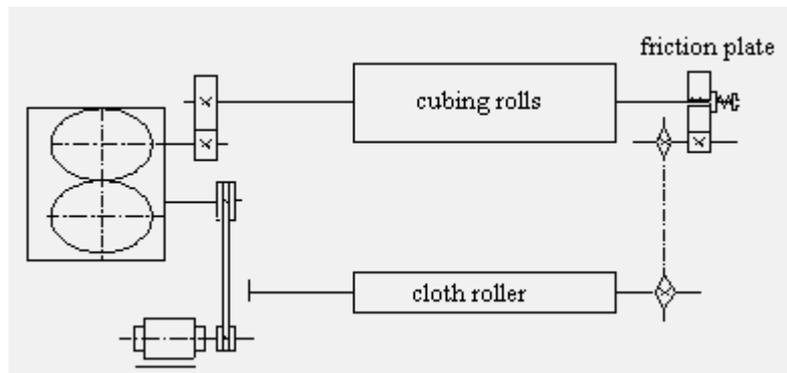
Figure 4. Sketch of Improved Take-up Machine

Moving Objects Segmentation Based on Histogram for Video Surveillance

Jinglan Li

College of Information

Linyi Normal University

Linyi 276005, China

E-mail: lijinglan1229@163.com

Abstract

The detection of moving object is one of the key techniques for video surveillance. In order to extract the moving object robustly in complex background, this paper presents a novel background subtraction method for detecting foreground objects in dynamic scenes. The difference image of color distance between current image and the reference background image in YUV color space is first obtained. According to the mono-modal feature of histogram of the difference image, an adaptive clustering method based on histogram is given. With morphological filtering, the flecks of noise existed in the segmented binary image can be removed. Finally, an updating scheme for background image is introduced to follow the variation of illumination and environmental conditions. Experimental results show that the proposed approach can detect moving objects effectively from video sequences.

Keywords: Image processing, Segmentation, Histogram, Detection

1. Introduction

The detecting of moving target in video sequence is of importance in many applications, such as intelligent transportation, safety monitoring, etc. At present, the main existed approaches of moving target detection are background difference, time difference (frame difference) and optical flow. In the past, there have been researchers investigating kinds of methods for segmenting moving objects in real time to achieve these vision-based applications. For example, difference image method was proposed in Anderson, C(1985), and the optical flow technique was introduced in Barron, J(1994). The impact of noise, many light source, shadows (Y.M.Wu, 2002, Wren, C.1997), transparency and shelter reduces the reliability and accuracy of the algorithm which is based on optical flow technology for moving object detection methods. Despite these difficulties, computational complexity and time-consuming further complicate the moving object detection in real-time monitoring(Lipton, A,1998), it is hard to meet real-time requirement without the support of specific hardware devices. Image difference method was divided into the background difference method and the inter-frame difference method. The former algorithm is simple but it lacks a reasonable method for the background update, which changes with illumination and other factors. The latter using the adjacent frame difference can extract information of moving objects, The method is robust to the change of environment, since it assumes that there should be a certain degree of difference of moving speed between target and background, and the information of grey scale or gradient of temporal difference image can be employed to obtain the moving information from the deviation of two or three consecutive frames. but objects of sudden stopping cannot be detected, and this method can not solve the problem of background exposed and the overlapping of moving objects in the adjacent frames. In addition, the current difference method, which didn't make full use of rich color information, is generally limited to two images of the brightness, but color information is indispensable in practical application.

In this paper, a new method is proposed for separating moving objects from current frame. In order to change in time(Yujian, S,2001) with the illumination of background scene, the quick update strategy of reference background image is given. Due to the simplicity of the proposed method, the moving objects can be extracted accurately and quickly.

2. Moving Objects Segmentation

2.1 Determining Color Difference Model

Traditional method of background image subtraction accomplished with background images and the current image in the gray space, because of less information available in gray space, the gray value of the target and background are very closely, fracture and large hole would appear in difference image, which are not conducive to further processing.

Through observation and analysis of many images, the same moving object and background in gray space are the same. Generally, they wouldn't be identical in color space. Thus the color image difference model(D.Wang,2002) was chosen in this paper. RGB color model in the computer field has an important position, which was been widely used in computer graphics and imaging. However, in some image applications, this model is not effective as the former, because all its colors are all isometric pixel R, G, B three colors to be synthesized. This allows each pixel on the three components of the R, G, B has the same pixel depth and display resolution. In addition, related to human visual system, human eyes has a higher sensitivity on the low-frequency6 signals than on high-frequency signal, compared the changes of visibility with color, the former was more sensitive. Therefore, YUV color model was chosen, transform formula is as follows:

$$\begin{bmatrix} Y \\ U \\ V \end{bmatrix} = \begin{bmatrix} 0.299 & 0.587 & 0.114 \\ -0.148 & -0.289 & -0.437 \\ 0.615 & -0.515 & -0.100 \end{bmatrix} \begin{bmatrix} R \\ G \\ B \end{bmatrix} \tag{1}$$

color difference mode as follow:

$$dd = a * \sqrt{d_1^2 + d_2^2 + d_3^2} \tag{2}$$

else:

$$d_1 = | Y_b(i, j) - Y_k(i, j) | \tag{3}$$

$$d_2 = | U_b(i, j) - U_k(i, j) | \tag{4}$$

$$d_3 = | V_b(i, j) - V_k(i, j) | \tag{5}$$

where $Y_b(i, j)$, $U_b(i, j)$ and $V_b(i, j)$ are three values of the pixel in the background, respectively, and $Y_k(i, j)$, $U_k(i, j)$ and $V_k(i, j)$ are three values of the pixel in the current frame. The a is an experienced value, which obtained from a large number of experiments, 0.5 is the value of a in the paper. Because of full use of information in the color difference model, the method greatly improves the integrity of the target region.

2.2 Segmentation Algorithm

Differential image segmentation algorithms mainly include automatic threshold approach based on class variance, euclidean distance among all instances of different class, the histogram segmentation method and the clustering segmentation method based on the Gaussian model. However, the above methods are all not applicable, if color distance is used as the difference result in the color space. Since automatic threshold segmentation method was most suitable in the bimodal histogram of the image, and the histogram from color distance as shown in Fig.1 is single-peak form, Gaussian model-based approach is to assume that pixel values of difference image obey the Gaussian distribution, in which there must be the margin of plus or minus. According to (2), the distance value is positive, and negative value does not exist. Thus new segmentation method should be explored.

In Fig.1, horizontal axis represents the gray value of the image. Vertical axis represents the frequency of occurrence of each gray value. As can be seen from Fig.1, the histogram shows the characteristics of a single and highly concentrated peak. Single-peak represents the background region. The color difference is not exactly zero, but an interval greater than zero. The upper limit of interval is decided by the width of single-peak. Based on these features, a segmentation algorithm is presented as follows:

1) Find the maximum peak value *pf* of the difference image histogram and the gray value *pc*, which is clustering centre of the background region and corresponding to the peak.

2) Seek the width *hw* of peak. Experiments indicate that peak width corresponding to $0.04 * pf$ height can achieve more satisfactory segmentation results, and *hw* could be obtained by the statistics of histogram.

3) Find clustering radius R. $R = hw - pc$.

4) In accordance with the established clustering centre and clustering radius, clustering starts on the difference image. Suppose any pixel gray value is p_i and $|p_i - pc| \leq R$, the pixel belongs to background; otherwise, it belongs to moving object.

Obviously the clustering centre and the clustering radius depend on the single-peak shape of the histogram and change with it, so it has strong adaptive ability.

2.3 Morphological Method Dealing with Binary Image

Wind and other factors will lead to changes of elements, such as trees, grass in background, so difference image contains lots of noise. The difference image after binarization still has a lot of useless noise spots in the background and objects. In this paper, Mathematical Morphology (Zhu,Weigang, 2002) is used to carry out post-processing of the segmented binary image. Basic morphological operations include expansion, corrosion, opening, closing, etc. Combined opening and closing can achieve morphological noise filter, which can effectively remove noise spots. Since the scale of morphology filter is fixed, the target region may also have empty holes after segmenting. Area surrounded method is applied to fill the hole of object in order to provide complete moving templates, benefiting to the background update and so on.

2.4 Updating Background Strategy

In video surveillance, because of changes of outdoor light and climatic condition, background image(Pascual, J,2006) must have its corresponding update strategy. If no moving object is detected at a fixed time interval, the current frame image substitutes for the background image; otherwise, the background should be updated after segmentation of each moving object. The updated region is obtained from moving templates ahead. The background of current frame can be adapted as follows:

$$B_K(i,j) = \begin{cases} I_{K-1}(i,j) & \text{if pixel } (i,j) \text{ not belongs to motion region} \\ B_{k-1}(i,j) & \text{otherwise} \end{cases}, \tag{5}$$

where $B_k(i,j)$, $I_{K-1}(i,j)$ and $B_{K-1}(i,j)$ are point pixels of the *Kth* background, $(K-1)th$ frame and the $(K-1)th$ background respectively. *i* and *j* are the coordinates.

3. Experimental results

The algorithms discussed above were tested on personal computer with an INTEL Pentium 4 2400 CPU using Microsoft Visual C++6.0. In this paper, all images used were obtained by a general video camera and the size of the image is 320×240. In order to analyze the effectiveness of the proposed method, many experiments under different conditions were performed. Fig.2 was typical experimental results. The background frame and the current frame are shown in Fig.2(a) and Fig.2(b) respectively. The segmentation and morphological filtering results of the algorithms are shown in Fig.2(c) and Fig.2(d). At last, an integrated moving object can be seen in Fig.2(d). The experimental results also shows that the method can segment moving object accurately and quickly.

4. Conclusion

In this paper, methods of moving objects segmentation based on histogram were proposed to detect moving objects effectively. The method used YUV color model by using (2) to obtain difference image of color distance. Then a histogram could be obtained by statistics of the difference image. The information extracted by algorithm in this paper was used for segmenting moving targets. In particular, the background subtraction was applied to detect image motion, and the algorithm correctly distinguished the changed areas in the scene from the background. Experimental results indicated that the proposed algorithm is simple and effective in segmenting moving objects. Since the background update was performed only in the changed areas where the moving objects occurred too frequently, the computational load is reduced significantly. Moreover, the proposed methods are based on general scenes, so it is suitable for other surveillance sequence.

References

Anderson, C., Burt, P., van der Wal, G. (1985). Change detection and tracking using pyramid transformation techniques. *Proceedings of SPIE-Intelligent Robots and Computer Vision*. vol. 579, pp.72–78

Barron, J., Fleet, D., Beauchmin, S. (1994). Performance of optical flow techniques. *International Journal of Computer Vision.* 12(1), pp.42–77

D. Wang, T Feng, H. Y. Shum, S. Ma. (2002). A Novel Probability Model for Background Maintenance and Subtraction. *Int'Conf. on Vision Interface*, pp.109-117.

Lipton, A., Fujiyoshi, H., Patil, R. (1998). Moving Target Classification and Tracking from Real-time video. *Proceedings of IEEE Workshop on Application of Computer Vision*. IEEE Computer Society Press, Los Alamitos. pp. 8–14.

Pascual, J., Neucimar, J., Barros, Ricardo, M.L. (2006). Background Recovering in Outdoor Image Sequences: An

Example of Soccer Players Segmentation. *Image and Vision Computing*. 24(4), pp.363–374.

Wren, C., Azarbayejani, A., Darrell, T., Pentland, A. (1997). Pfinder: Real-time tracking of the human body. *IEEE Transactions on Pattern Analysis and Machine Intelligence.* 19(7), pp.780–785.

Y.M.Wu, X.Q.Ye & W.K.Gu. (2002). A Shadow Handler in Traffic Monitoring System. *Proceedings of IEEE Vehicular Technology Conference*. vol.1,pp.303-307.

Yujian, S., Xin, H., Zhihang, H. (2001). Study on the method of determination for K coefficient in time-domain recursive filter. *Journal of Systems Engineering and Electronics*. 23(3), pp.61–65.

Zhu,Weigang, Hou,Guojiang & Jia,Xing. (2002). A study of locating vehicle license plate based on color feature and mathematical morphology. *Signal Processing*. vol.1,pp.748-751.
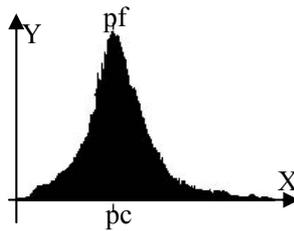
Figure 1. The general shape of the color difference histogram

(a) Background frame   (b) Current frame   (c) Segmentation algorithm   (d) Morphological filtering

in this paper   result
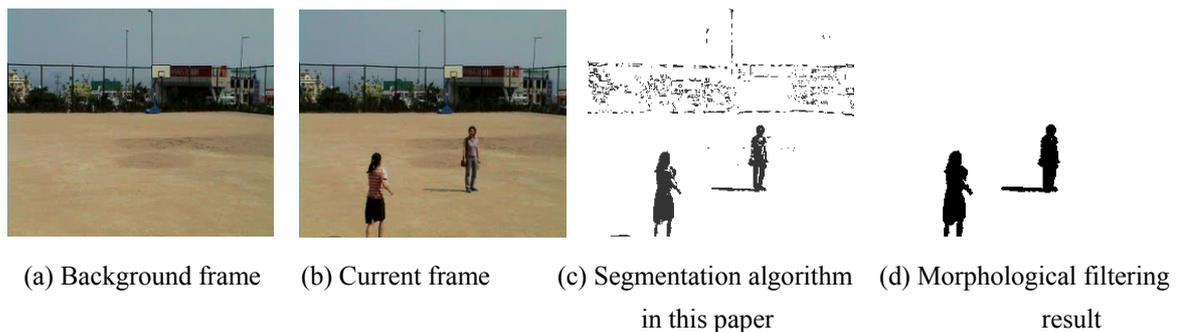
Figure 2. Moving object segmentation result

Research and Application of the Property of Conductive Knitted Fabrics

Liwen Li, Kun Yang, Guangli Song, Liang Zhang & Juan Guo

School of Textiles, Tianjin Polytechnic University, Tianjin 300160, China

Tel: 86-22-2452-8287   E-mail: kunyang@tjpu.edu.cn

Abstract

Traditional knitted fabrics have been extensively applied in dresses and home decoration, and in recent years, the applications of the fabrics knitted by new technologies and new materials also increase in other fields. The conductive fiber knitted fabrics was used in the article, and its electric properties under transverse stretching were tested and researched. Based on the electric model of 1×1 rib fabrics, the silver-coasted conductive yarns were adopted to knit the conductive fabrics, and the stretching test was conducted, and the relationship between stretching and resistance was primarily analyzed. Then, a product prototype, an electronic organ with force sensitive keyboard was designed. The test result reveals that it works well.

Keywords: Conductive knitted fabrics, Stretching, Resistance, 1×1 rib

In recent years, the research and application of conductive fibers have been gradually mature, and the conductive fibers can not only eliminate static and absorb electromagnetic wave, but can be used in the detection technologies such as the detection and transmission of electric signals. As a kind of important intelligent material, the conductive fibers have been extensively concerned by foreign and domestic material industry, and possess bright application foreground in dresses, sensors and other industries (Li, 2003). Some literature had acquired the relation between the resistance and density of the flat conductive knitting fabrics with the single-axis stretching through test and theoretical analysis, and studied the impacts of various factors on the conductive knitted fabrics, and established the theoretical model (Yang, 2006). Good flexibility and stretching property of the knitted fabrics make the sensors to fit measuring the large stretching stress and possess more extensive application range. The fabric texture, loop transfer, contact resistance and loading speed of the conductive knitted fabrics are the factors to impact the resistance of the fabrics (Yang, 2008 & Zhang, 2005). These scholars studied the application of conductive knitted fabrics, and most of them aimed at the plain knitted fabrics, and few of them studied the conductive knitted fabrics with other textures, because other textures such as 1×1 rib texture has different geometric structure and electric property with the plain knitted texture. Therefore, it is necessary to further study the electric conductivity of other conductive knitted fabrics in large transverse stretching. In the article, the stretching test of the conductive knitted fabrics (1×1 rib) was made to obtain the stretching change rule of fabric resistance, and relative properties were discussed simply, and the applied product prototype was designed based on above researches.

1. Basic theories

The theoretical research of conductive knitted fabrics is based on following hypothesis, i.e. the unit length of conductive fiber resistance is invariable, and isn't impacted by the stretching and distortion in certain stretching range (Xue, 2004). When the fabrics are drawn, the transfers of various loops are consistent, i.e. the yarns in the loop transfer from the arc part to the pole part, and under the premise that the loop length is invariable, the resistances of the art part and the pole part change with the changes of lengths, so the network resistances of the whole fabrics will correspondingly change. Figure 1 is the geometric structure unit of the 1×1 rib conductive fabrics loop, and Figure 2 is the corresponding resistance unit model, and R_{L1}, R_{L2} and R_{L3} denotes the length resistances, and Rc denotes the contact resistance in the unit.

The electrics model of 1×1 rib conductive knitted fabrics can be established based on Ohm's Law and Kirchhoff's Law, and the formula (1) is the matrix expression of various loop currents.

$$[R_{k,j}^{*}][i_k] = [U_j] \quad (k=1,3,5,...,m; j=1,2,3,...,n) \tag{1}$$

Where, $\left[R^{*}_{k, j} \right]$ denotes the matrix expression of the k'th row and the j'th line in the network circuit model, i_{k} denotes the loop current of the mesh in the circuit model, U_{j} is the exterior voltage of the circuit, and *m* is odd number and *n* is natural number.

$$\left[R^{*}_{k,j} \right] = \begin{pmatrix} R_{1,1}+R_{1,2}+R_{2,1} & -R_{1,2} & 0 & 0 & \dots & -R_{2,1} & 0 & 0 & \dots & \dots & -R_{1,1} \\ -R_{1,2} & R_{1,2}+R_{1,3}+R_{2,2} & -R_{1,3} & 0 & \dots & 0 & -R_{2,2} & 0 & \dots & \dots & 0 \\ 0 & -R_{1,3} & R_{1,3}+R_{1,4}+R_{2,3} & -R_{1,4} & \dots & 0 & 0 & -R_{2,3} & \dots & \dots & 0 \\ \dots & \dots & \dots & \dots & \dots & \dots & \dots & \dots & \dots & \dots & \dots \\ \dots & \dots & \dots & \dots & \dots & \dots & \dots & \dots & \dots & \dots & \dots \\ \dots & \dots & \dots & \dots & \dots & \dots & \dots & \dots & \dots & \dots & \dots \\ -R_{1,1} & 0 & 0 & 0 & \dots & 0 & \dots & 0 & \dots & \dots & R_{1,1}+R_{3,1}+R_{5,1}+R_{7,1}+R_{9,1}+\dots+R_{m-2,1}+R_{m,1} \end{pmatrix} \quad (2)$$

$$\left[U_{j} \right] = \begin{pmatrix} 0 \\ 0 \\ 0 \\ \dots \\ \dots \\ \dots \\ U \end{pmatrix} \quad (3)$$

Through computing $\left[R^{*}_{k, j} \right]$ in (1), the total current $i_{(\frac{m+1}{2}) \times n+1}$ of the whole loop can be obtained, and $(\frac{m+1}{2}) \times n + 1$ is the amount of loop.

2. Stretching electric conductivity test of conductive knitted fabrics

The rib texture is collocated by the transverse line of the obverse loop and the transverse line of the reversed loop alternately. The sinking arc linking the obverse loop and the reversed loop bears large bending and torsions, and the loop transverse lines on each face are adjoined each other. Therefore, when the transverse stretching happens, the fabrics will have larger flexibility than the plain knitted fabrics. In the research, the most representative 1×1 rib textures were selected to knit the conductive fiber fabrics.

2.1 Experiment materials and equipments

Because of the limitation of the knitted property of conductive fibers, the Flying Tiger hand-operated flat knitting machine was selected based on the results of primary test research (Zhang, 2008) and comparison. The machine gauge is E9, i.e. 9npi. The raw materials were silver-coated conductive fibers. Table 1 shows the specs of conductive fibers and conductive knitted fabrics.

In the experiment, the LK-1 knitted fabrics stretching property tester was used to stretch the fabrics (seen in Figure 3), and the stretching speed was 30cm/min, and the initial tension was 0.5N. The resistance change of the conductive fabrics was measured and recorded by the Agilent Digit Multimeter connecting with the computer. The instrument connection is seen in Figure 4.

2.2 Experiment test and result analysis

The current in the experiment was obtained by measuring the resistance transversely passing the fabrics, and Figure 5 is the relation between the stretching rate (ε) and the resistance (R) in the stretching process of the conductive fabrics.

In Figure 5, in the whole stretching process, the resistance of the conductive fiber fabrics changed obviously. The relative resistance of the conductive knitted fabrics reduced with the increase of ε, and the electric conductivity increased correspondingly, which was close to the linear relation in certain strain range. When the stretch achieved certain value, the resistance of the fabrics was stable basically, and the electric conductivity of fabrics achieved a relatively stable state.

3. Application of the conductive knitted fabrics

3.1 Design scheme

Above theoretical analysis and experiment result indicated that the resistance of conductive knitted fabrics changed with the stretching length. Based on that conclusion, the electric organ was converted in the experiment. The volume controller of the electric organ was a controllable resistor in fact, and when the volume controller was turning, the resistance of the controllable resistor would change. The change of the resistance would change the voice intensity of the trumpet. So when the volume control knob was turning, the sound of the electric organ would change with that.

Connect the silver-coated conductive fiber knitted fabrics with the circuit of the electric organ, and stretch the conductive fiber fabrics at the connecting place by the knob form to change the resistance in the circuit and change the current, and accordingly change the loudness of the electric organ.

According to the experiment result, it was ideal to control the stretching resistance change of the conductive knitted fabrics in 30%.

3.2 Circuits assembly

Figure 6 is the circuit diagram of the electric organ, and various components are connected by the circuit principle diagram, and Figure 7 is the converted electric organ (6V).

3.3 Test result and analysis

The research reflected the change of the resistance of the whole circuit by measuring the voltage change of two ends of the electric organ, and the current change.

From the test result (Table 2), in the whole stretching process, because of the stretching, the resistance of fabrics decreased, so the current of the whole circuit changed. In the circuit, to press the key-press could stretch the conductive fiber to change the resistance of the whole circuit, and the result could basically accord with the initial hypothesis of this research.

The silver-coated fibers are the yarns with silver-coated surface, and different materials have different stretching properties of the yarn and metallic-membrane plating when the fibers were stretching. The anti-stretching performance is stronger than the performance of the silver-coated surface, and when the stretch achieves a certain extent, the conductive fiber will be stretched, and its exterior silver-coated surface will be cracked, so the resistance will increase, and the current will first increase and reduce later, which showed that in actual application, the stretching flexible range and the application limitation of fabrics with different materials should be considered.

4. Conclusions

In the research, the stretching test and theoretical analysis of the conductive fiber knitted fabrics indicated that with the increase of stretching and distorting, the resistance of conductive knitted fabrics reduced correspondingly, and when the stretching achieved certain degree, the electric conductivity of fabrics achieved a relatively stable state. Combining with the conductivity of conductive fiber and the stretching property of knitted fabrics, the knitted conductive fabrics were connected into the circuit of the electric organ, and under different pressing states (different stretching degrees), the current in the circuit would change with the change of resistance, and the loudness of the electric organ would also change. But it needs further research to exactly control the volume of the electric organ.

References

Li, W. & Zhuang, Q.L. (2003). Development of Electrically Conductive Fibers and Its Smart Textiles. *Technical Textiles*. No.8.

Xue, P., Tao, X. M., Yu, T. X., Kwok, K. & Leung, S. (2004). Electro-mechanical behavior and mechanistic analysis of fiber coated with electrically conductive polymer. *Text. Res. J.* No.74. P.924-937.

Yang, B. & Tao, X.M. (2008). Effect of Tensile Condition and Textile Structure on Resistance Response of Stainless Steel Fibers Fabric. *Rare Metal Materials and Engineering*. No.37(2).

Yang, B., Tao, X.M. & Yu, J.Y. (2006). A Study on the Relation between Resistance and Strain Based on Stainless Steel Fabric. *Rare Metal Materials and Engineering*. No.35(1). P.97-99.

Zhang, H., Tao, X.M., Wang, S.Y. & Yu, T.X. (2005). Electro-mechanical properties of knitted fabric made from conductive multi-filament yarn under unidirectional extension. *Text. Re. J.* No.75. P.598..

Zhang, L., Song, G.L. & Yang, K. (2008). Study on Knittability of Conducting Knitted Fabric. *Journal of Tianjin Polytechnic University*. No.5.

Table 1. Specifications of conductive yarns and conductive knitted fabrics

Material	Base material	Diameter (mm)	Stretching rate (%)	Electric conductivity ($\Omega.cm^{-1}$)	Amount of multifilament	Fabric texture	Spec of fabrics (cm×cm)
Silver-coated fibers	Chinlon	0.020	26	$10^1 \sim 10^2$	12	1×1 Rib	12×6

Table 2. Test table of electric organ

| Pressing State	1	2	3	4	5
U (mV)	19	15	11	9.42	5.0
R (Ω)	20	15	10.4	7.8	4.7
I (A)	0.95	1	1.06	1.2	1.01
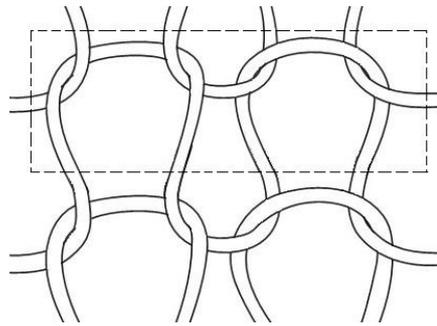
Figure 1. Geometrical Unit of 1×1 Rib Structure
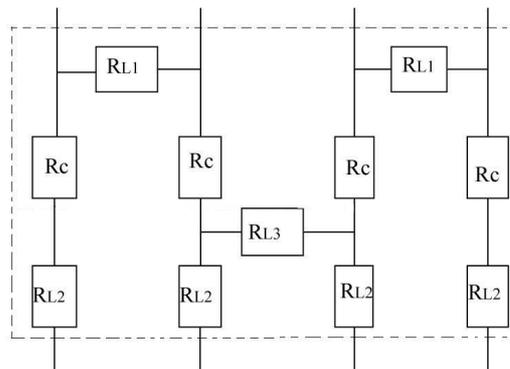

Figure 2. Model of Resistance Unit
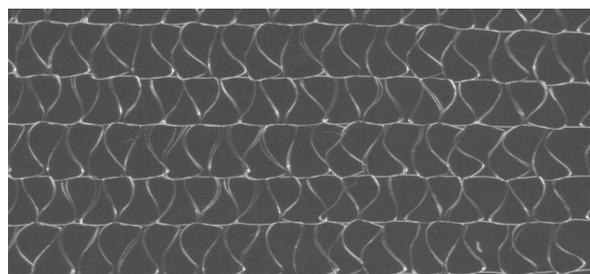
Figure 3. Conductive Knitted Fabrics Knitted by Silver-coated Yarns

Figure 4. Test System
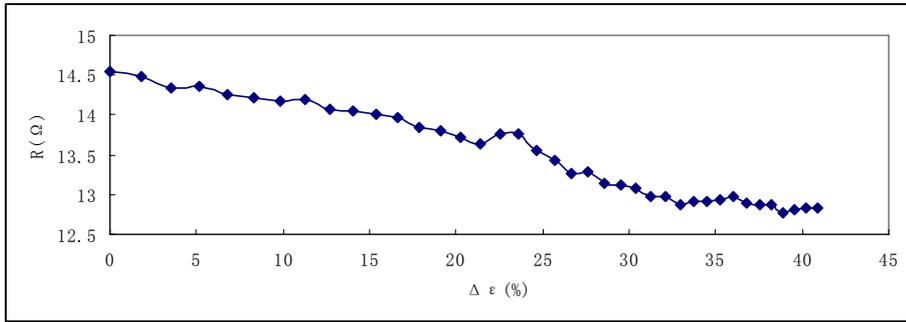
Figure 5. Change of the Silver-coated Conductive Fiber Fabrics Resistance with Stretching
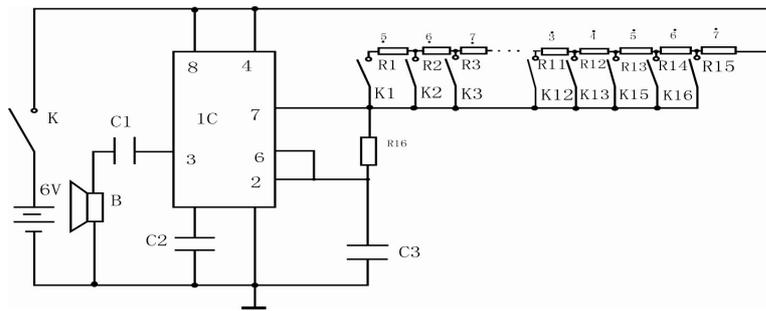
Figure 6. Circuit Principle of Electric Organ

Figure 7. Converted Electric Organ

Modern Applied Science